Engineering Low Noise Organic Electrochemical Transistors for Electrophysiology Applications

Anastasios Polyravas

Department of Engineering

University of Cambridge

This thesis is submitted for the degree of

Doctor of Philosophy

Downing College June 2021

Declaration

I confirm that this thesis does not exceed the limit of 65,000 words, including references, tables and equations; and it contains less than 150 figures, in accordance with the Department of Engineering guidelines. The work presented in this thesis has been carried out by me, under the supervision of Professor George Malliaras and Dr. Ronan Daly, at the University of Cambridge; with the exception of the following:

- Chapter 3 & 4: Noise measurements were performed in a custom made set up in the Catalan Institute of Nanoscience and Nanotechnology (ICN2).
- Chapter 5: Noise data were collected and exported by Mr. Ramon Garcia at the Catalan Institute of Nanoscience and Nanotechnology.
- Chapter 6: Surgeries for the devices implanted in rats were performed by Dr. Alejandro Carnicer Lombarte at the University of Cambridge.

I hereby declare that except where specific reference is made to the work of others, the contents of this dissertation are original and have not been submitted as a whole or in part for any other degree, diploma or qualification in this or any other university.

Abstract

Engineering Low Noise Organic Electrochemical Transistors for Electrophysiology Applications

Anastasios Polyravas

Understanding how the nervous system functions has always been one of the most difficult challenges the medical community has faced. Despite the progress made so far, the ability of scientists to treat brain disorders has been severely limited by the complexity of the nervous system and the quality of the information derived from recording devices. A device that holds great potential for recording high quality electrophysiology signals is the organic electrochemical transistor (OECT). OECTs have been fabricated onto flexible substrates from biocompatible materials and have been shown to provide higher signal-to-noise ratio (SNR) than electrodes. Their unique properties can pave the way for enhanced performance neural interfaces whilst minimising the invasiveness of the recording method.

In this study, a thorough analysis of the noise characteristics of OECTs was performed with the greater aim of utilising these findings to further improve the performance of OECTs in various *in vitro* and *in vivo* environments. From an engineering perspective, different parameters such as the device geometry and the thickness of the channel film were tuned to minimise the intrinsic noise of an OECT. OECTs with different overlap between the conducting polymer and the source-drain gold contacts were fabricated. It is shown that the contact overlap reduced the frequency response of OECTs without affecting the noise level, suggesting that a good Ohmic contact is achieved. The effect of the thickness of the polymer film was also studied, indicating that noise can be further reduced as a function of increased channel thickness. This effect was observed up to a specific polymer thickness, above which the noise level reached a plateau. These findings allow to design OECTs that exhibit record low noise and lead to the establishment of new design rules.

To further understand the origins of noise in OECTs, we applied these design rules and tested the performance of our devices under different bias conditions. It has been shown that the voltage applied between the three terminals of an OECT can modify the signal amplification, rendering an optimisation on the biasing conditions imperative for high quality recordings. By employing different bias conditions, we managed to combine maximum signal amplification with minimum noise, leading to an increased SNR. Our results highlight that the optimum operation point is achieved at zero gate voltage.

Finally, an analysis of the performance of our low noise OECTs in an *in vitro* and an *in vivo* application was performed. The *in vitro* application consisted of a simulated neuron configuration that was employed to test the capability of OECTs to record low amplitude, high frequency signals. It is shown that OECTs have the potential to record a variety of neurological signals, including action potentials. The application of OECTs in electrocorticography (ECoG) recordings was also explored. By using devices that consisted of both transistors and electrodes, we collected and compared the quality of epidural recordings. OECTs were found to outperform electrodes and the quality of the recordings was significantly high, even with minimal filtering. Our findings demonstrate that OECTs are an ideal candidate for chronic neurological recordings due to their ability to provide consistent high signal quality in a minimally invasive set up.

This thesis is dedicated to the memory of my grandpa Anastasis

Acknowledgements

First and foremost, I would like to express my sincere gratitude to my supervisor Professor George Malliaras, not only for giving me the opportunity to join the group but also for all the support and guidance he was always so willing to provide me with. Exploring the world of research under his supervision was a pleasure; I hope one day I could be as an inspirational leader as he is. I am also thankful to my advisor Dr. Ronan Daly for his input in my research, especially at the beginning of my PhD.

Working in the Bioelectronics group in Cambridge has been a lifetime experience as it allowed me to grow as a researcher and in the meantime, helped me to develop as a person due to all these great people I had a chance to meet. One of them is Vincenzo, who's attitude and patience towards life (and me) was a joy to experience. I am really thankful for having worked with him and for all the mentorship and knowledge he was so kind to share with me. I would also like to express my gratitude to Alex and Chris, who were post docs in the group and some of the first people I met when I arrived in Cambridge, and were always there to help me and guide me when needed. Johannes and Santi are two of the people I was lucky enough not just to collaborate with but also to live together for the last year of my studies. Lucky is maybe the best word to describe meeting them; I had so much fun this last year, even with all these COVID restrictions and self-isolations we had to go through. I am also grateful for having met Roberto, Sanggil, Alejandro and Sagnik; it was a pleasure working and travelling with you. Nathan, Ramon and Andrea are some of the people I met in Barcelona under the flag of the Braincom project and were so kind to help me with my topic and also give me multiple tours of this amazing city. Eleftheria is one of the people I might have met for a short period of time but managed to build a strong friendship with; I cannot but thank her for all the support she gave me (despite thinking of charging me for it at the end) and for being so original, such a unique personality she has.

Finally, I feel the need to thank some people who despite being in distance were always available and happy to hear me out. These were my mom and dad, Kathrine and George, my siblings, Ioannis and Sotiria, my cousin Giannis and two of my best friends, George and Dimitris. I really appreciate your endless support and the fact that no matter what happened you always believed in me. And a special thanks to my grandpa Anastasis, who might not be with us anymore, but will always have a special place in my heart.

All these would not have been accomplished without funding, however. Hereby, I would like to gratefully acknowledge funding from the European Union's Horizon 2020 research and innovation programme under grant agreement no. 732032 (BrainCom).

PUBLICATIONS

- **Anastasios G. Polyravas**, Alejandro Carnicer-Lombarte, Sanggil Han, V. F. Curto, G. G. Malliaras, “High Quality Epidural Recordings using Organic Electrochemical Transistors”. *in preparation*.
- Sanggil Han, **Anastasios G. Polyravas**, Shofarul Wustoni, Sahika Inal, George G. Malliaras “Integration of organic electrochemical transistors with implantable probes”. *submitted*
- Farnaz Fahimi Hanzaee, Peter J. Langlois, **Anastasios G. Polyravas**, Ivan B. Dimov, Richard H. Bayford, George G. Malliaras, Andreas Demosthenous “A DC Model for Organic Electrochemical Transistors and Analysis of Their Performance as Voltage Amplifiers”. MWSCAS 2021 conference, *accepted*.
- **Anastasios G. Polyravas**, C. M. Proctor, V. F. Curto, D. G. Barone, G. G. Malliaras, “Organic Bioelectronics”. Handbook of Neuroengineering, Springer, Nitish V. Thakor, Ed., Springer Nature, *submitted* (2021).
- Sanggil Han, Shunsuke Yamamoto, **Anastasios G. Polyravas**, G. G. Malliaras, “Microfabricated Ion-Selective Transistors with Fast and Super-Nernstian Response”. *Adv. Mater. n/a, 2004790* (2020).
- **Anastasios G. Polyravas**, N. Schaefer, V. F. Curto, A. B. Calia, A. Guimera-Brunet, J. A. Garrido, and G. G. Malliaras, “Effect of channel thickness on noise in organic electrochemical transistors”. *Appl. Phys. Lett. 117, 073302* (2020).
- **Anastasios G. Polyravas**, V. F. Curto, N. Schaefer, A. B. Calia, A. Guimera-Brunet, J. A. Garrido, and G. G. Malliaras, “Impact of contact overlap on transconductance and noise in organic electrochemical transistors”. *Flex. Print. Electron. 4, 044003* (2019).

CONFERENCE PRESENTATIONS

- "Effect of channel thickness on Noise in Organic Electrochemical Transistors", **MRS Fall Meeting & Exhibit**, Boston, Massachusetts, USA; oral online presentation (December 2020).
- "Using Organic Electrochemical Transistors for Enhanced Electrophysiology Recordings", **InnoLAE**, Cambridge, United Kingdom; poster presentation (January 2020).
- "Using Organic Electrochemical Transistors for Enhanced Electrophysiology Recordings", **MRS Fall Meeting & Exhibit**, Boston, Massachusetts, USA; oral presentation (December 2019).
- "Organic Electrochemical Transistors for Neural Interfaces", **Milner Therapeutics**, Cambridge, United Kingdom; poster presentation (June 2019).
- "Enhancing the Performance of Organic Electrochemical Transistors by Understanding the Effect of Noise", 6th International Winter School on Bioelectronics, **BioEl 2019**, Tyrol, Austria; poster presentation (March 2019).
- "Sources of noise in OECTs", **BioMedEng18**, London, United Kingdom; poster presentation (September 2018).

Contents

List of Figures

List of Tables

List of Abbreviations

OECT	Organic electrochemical transistor
SNR	Signal-to-noise ratio
TFT	Thin film transistor
LFP	Local field potential
MEA	Microelectrode array
EEG	Electroencephalography
ECoG	Electrocorticography
R_s	Electrolyte resistance
R_e	Double layer resistance
R_m	Microelectrode resistance
C_e	Double layer capacitance
CP	Conducting polymer
PEDOT:PSS	Poly(3,4-ethylenedioxythiophene):poly(styrene sulfonate)
V_{sig}	Electrical signal generated by a population of neurons
V_{in}	Input signal
Z_a	Amplifier impedance
V_{rec}	Amplified signal
PaC	Parylene C

PI	Polyimide
V_D	Drain-source voltage
V_G	Gate-source voltage
I_D	Drain current
g_m	Transconductance
MOSFET	Metal oxide semiconductor field effect transistor
W	Width of the transistor channel
L	Length of the transistor channel
d	Thickness of the transistor channel
μ	Mobility of the holes/electrons
C	Volumetric capacitance
V_{TH}	Threshold voltage
OFET	Organic field effect transistor
DOS	Density of states
PET	Polyethyleneterephthalat
DBSA	Dodecyl benzene sulfonic acid
GOPS	3-glycidoxypropyltrimethoxysilane
PSD	Power spectral density
S_V	Voltage power spectral density
S_I	Current power spectral density
k_B	Boltzmann's constant

T	Temperature in Kelvin
R	Resistance of a device
Δf	Frequency bandwidth
a	Hooge parameter
f	Frequency
N	Total amount of free charge carriers
PTV	Poly-thienylene vinylene
p	Hole density
σ	Conductivity
e	Elementary charge
S_{VG}	Gate referred voltage noise
FET	Field effect transistor
DI	Deionised water
IPA	Isopropyl alcohol
A	Surface area
f_c	Cut-off frequency
V_{rms}	Voltage fluctuations in a specific frequency bandwidth
L’	Length of the PEDOT:PSS stripe
LOD	Limit of detection
BCI	Brain computer interface
CSF	Cerebrospinal fluid

ACF	Anisotropic conductive film
ZIF	Zero insert force
PCB	Printed circuit board
SMU	Source measure unit

Chapter 1

Introduction

1.1 Thesis overview

This thesis focuses on broadening our knowledge on devices that can be used for neural interfaces. The device physics of organic electrochemical transistors (OECTs) are explored with more emphasis being placed on their noise characteristics, as the main way to understand and thus, improve their performance. The findings of these studies are then applied in an *in vitro* and an *in vivo* environment. The main contributions of this thesis are split into seven chapters as follow:

- Chapter 1 introduces the motivation behind this study and provides a background on the need for neural interfacing, the different methods and types of electrophysiology recordings, as well as the fundamentals of OECTs and noise in organic devices.
- Chapter 2 presents the methods and the materials used to fabricate and characterise the devices used for this work.
- Chapter 3 focuses on how geometry and the bias conditions can be utilised to tune the performance of OECTs in a recording configuration, providing a set of design rules to achieve that.

- Chapter 4 investigates the effect of the channel thickness in the noise profile of OECTs, aiming to bridge the gap between maximum signal amplification and minimum noise level. These findings allow for an optimum operation point of OECTs from a recording and sensing perspective.
- Chapter 5 demonstrates the performance of an OECT, designed based on the rules set on the previous chapters for optimum signal-to-noise ratio (SNR) operation, in an in vitro configuration.
- Chapter 6 shows the behaviour of a similar OECT design in an electrophysiology configuration, used to collect epidural recordings in a minimally invasive way.
- Chapter 7 summarises the main findings of this study and highlights potential future directions.

1.2 Background

The human brain has always been one of the most important and complex systems of the human body. It consists of billions of neurons that communicate with each other by exchanging electrical signals in order to transmit and process the desired information to and from different parts of the body. Understanding the working mechanisms behind this significantly complex organ has been one of the greatest challenges of the medical community. In recent decades, a variety of approaches have been examined providing us with a better understanding of the neuronal functions.

Multiple diseases such as Alzheimer's, Parkinson's, epilepsy, depression and multiple sclerosis are affecting a large amount of the population with their causes rising from neurological disorders[2]. To successfully treat these diseases, we need to be able to specify the origin of the disorder by recording the brain activity and effectively stimulate different populations of neurons to restore their functionality. Despite the progress made so far, our ability to intervene with the human brain and establish a clear communication path has not provided us with the desired tools to deal with these disorders.

The rising demands of the medical community to improve the interaction between electronic devices and the human brain has paved the way for the invention of biocompatible or "organic" materials, as they are most commonly known, giving birth to the field of Organic Bioelectronics. Organic materials can translate electric signals into bio signals[3] and have low fabrication cost[4], becoming a fitting candidate for neural interfaces. Multiple electronic devices have been created including wires, electrodes and semiconductors using organic materials to interface with the brain. However, extracting the information from brain activity demands the recording of high quality signals, pushing the existing devices to their limits. A promising technology which can overcome such limitations and can be fabricated from biocompatible materials was developed by White and colleagues in 1984[5]. Their findings heralded the creation of the organic electrochemical transistor.

OECTs belong to the category of thin film transistors (TFTs) using an organic film as the semiconducting material. Their unique architecture confers them with biocompatibility as well as the ability to amplify the recorded signal, without the need of any external electronic circuits on the signal acquisition side. They have been shown to provide high signal-to-noise ratio recordings[6] and localised neuron stimulation[7]. Although the basic principles of operation of OECTs are understood, a more thorough analysis of their noise characteristics is needed to optimise the SNR and maximise their recording capabilities. OECTs hold great potential for the bioelectronics world as bio transducers and can eventually replace conventional electrodes.

1.3 Electrophysiology

Electrophysiology is "the study of the electrical properties of biological cells and tissues". It was Jan Swammerdam in the 17th century who first discovered that an electrical stimulation can cause muscle contraction on the legs of a diseased frog[8]. Swammerdam's research laid the foundations upon which Galvani based his more thorough exploration of the electric nature of nerves. Since then, medical research has attempted to understand how the human body reacts to stimuli derived from the environment, leading to the creation of bioelectronics as a scientific

field. Nowadays, bridging the gaps in our knowledge demands interaction with the nervous system through artificially made devices, called neural interfaces[9].

Neurons communicate with each other through an electrochemical process. The transmission of a signal within a neuron is carried in the form of an electrical pulse, called an action potential. Before receiving an impulse, the membrane of a neuron is in the resting phase exhibiting a -70 mV potential. This potential is generated from the difference in the concentration of ions between the inside and the outside of the cell membrane. The interior part is negatively charged as it contains a larger amount of potassium ions (K^+) compared to the exterior. A strong enough action potential arriving to the axon terminal of a neuron can cause the depolarisation of the target's cell membrane. If the threshold potential (-55mV) is reached the sodium (Na^+) channels open allowing ions to flow inside the membrane (Figure 1.1). This flux of positively charged ions is responsible for the depolarisation of the cell membrane, up to a +40 mV potential. This process is considered an "all-or nothing" event as it demands a strong enough stimulus to reach the threshold potential and completely depolarises the neuron membrane. Following that, the repolarisation of the membrane is achieved by closing down the Na^+ channels while K^+ channels open allowing K^+ cations to flow outside of the membrane. During this step (refractory period) the neuron is "inactive" and cannot respond to any other events. The membrane reaches a hyperpolarisation state due to the continuous diffusion of K^+ ions up until it stabilises, waiting to fire again (Figure 1.2). During the depolarisation of the membrane, calcium (Ca^{2+}) channels open, catalysing a procedure which unleashes neurotransmitter molecules. Neurotransmitters are then released into the synaptic cleft establishing connection between the presynaptic and the postsynaptic neuron, corresponding to the transmitting and receiving cells respectively. Through this process the information is transmitted to its final destination, by repeating this electrical-to-chemical signal translation process.

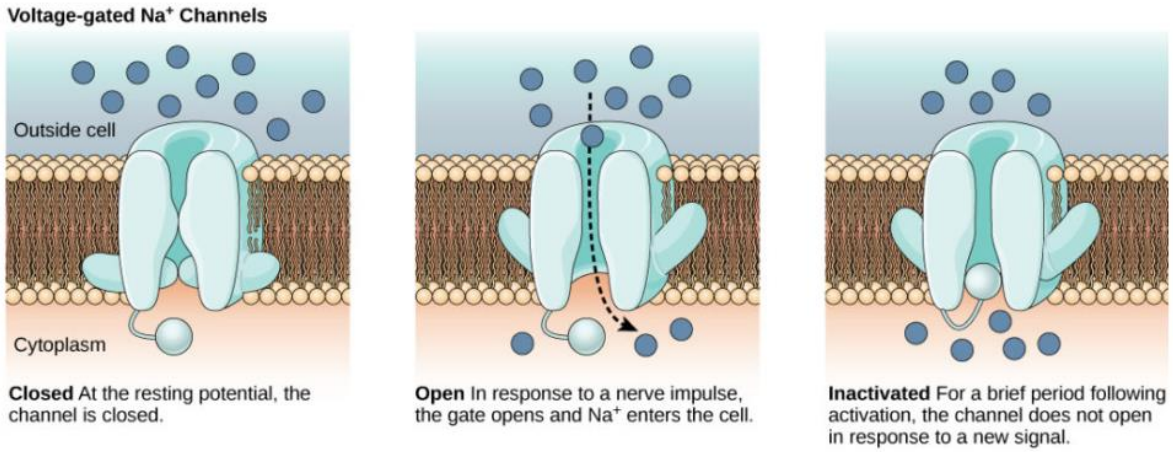

Figure 1.1 Voltage-gated ion channels responding to the potential of the cell membrane. The ion channels remain resting until an electrical impulse activates them, allowing the flow of positively charged Na^+. A short period of time is needed before the channels can respond to any other event. Image reproduced from [10].

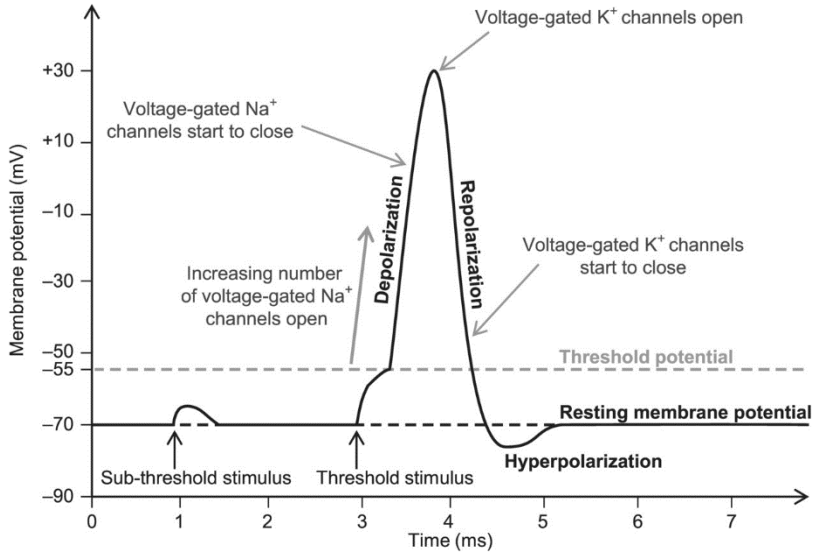

Figure 1.2 Propagation of an action potential. A large enough stimulus depolarises the cell membrane of a neuron. The neuron needs a finite amount of time to repolarise and restore its original resting state. Image adapted from [11].

1.3.1 Recording methods

The study of the electrical signals that are generated from brain activity has revealed that there are two main types of signals that can be traced[12]. The first one is the signal that is generated when a single neuron fires and is called action potential, as mentioned above. The amplitude of an action potential is in the range of 100mV for transmembrane potential measurements or in the range of 100μV for surface potentials with the frequency bandwidth being dominated by the refractory period, <500 Hz[13]. Collecting action potentials demands placing the recording device very close to the neuron to ensure sufficient high resolution (extracellularly) or alternatively, penetrate the membrane of the cell (intracellularly). The most commonly recorded type of signal is the local field potential (LFP). LFPs are more complex signals originating from a population of firing neurons. As a sum of multiple action potentials, LFPs vary in amplitude and frequency (<200 Hz). Although action potentials can provide more accurate information about specific neurons, the invasive methods that are needed most often to perform a reliable measurement have made LFPs more popular with neuroscientists.

There are two different approaches to record signals coming from neurons: intracellularly and extracellularly. Intracellular recordings offer higher signal quality, which can be translated into higher SNR but they come with the major drawback of invasive procedures. Early studies in the second half of the 20th century led to the invention of patch-clamp techniques[14], allowing the study of single ion channels in cells. This radical discovery furthered our knowledge of charge transportation in cell membranes and earned Erwin Neher and Bert Sakmann with the Physiology Nobel prize, in 1991. Later findings have employed nanowires[15], nanostraws[16] and gold mushroom—shaped microelectrode arrays (MEAs)[17]. Despite the fact that intracellular measurements provide a reliable quality of signal, further improvements are needed to tackle critical issues such as the connection with external recording circuitry and micromotion[18]. On the other hand, extracellular recordings provide lower resolution signals but are less/non-invasive. It is of paramount importance to mention that the invasiveness of this technique varies, depending on the recording method (EEG, ECoG, etc.). Electroencephalography (EEG) involves collecting

signals from the surface of the scalp by attaching arrays of electrodes on the skin. Although this method is non-invasive, the quality of the recorded signal is relatively of low amplitude (typically tens of μV) and low frequency (<100 Hz), as it consists of spontaneous electrical activity of underlying neurons[19,20]. Electrocorticography (ECoG) employs a more invasive technique in which the recording device is placed on top of the brain surface, after a craniotomy has been performed. The recording quality of this method lies between EEG and LFPs. This higher quality of the recorded signals originates from the removal of protective layers, such as the scalp and the skull, that significantly affects the quality of EEG recordings. The amplitude of ECoG is typically in the range of hundreds of μV and the majority of the information can be found in frequencies lower than 200 Hz[13,21]. Figure 1.3 summarises the recording types in relation to the brain sections. It should be noted that the recording method used depends on the quality of the extracted information that is desired; the higher the resolution of the signal the more invasive the approach.

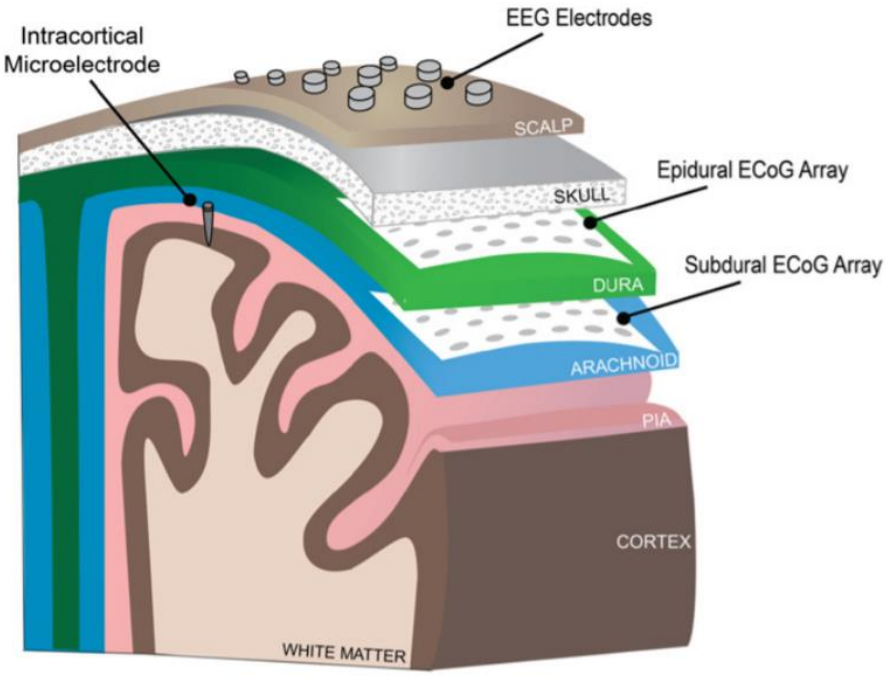

Figure 1.3 Different recording types relatively represented with the layers of brain from which they originate. Image reproduced from [22].

1.3.2 Electrodes as recording devices

The most widely used devices that record signals coming from the human brain have been electrodes. Electrodes have the ability to both record and stimulate neurons, making them a useful tool for neural interfaces. A more critical approach is needed to understand the advantages/disadvantages and the possible limitations of electrodes. Figure 1.4 illustrates the equivalent circuit that describes the operation of a recording electrode. The total impedance consists of 4 different elements: the resistances R_s, R_e, R_m and the double layer capacitance C_e. Reducing the interface impedance of the microelectrode is beneficial for both recording and stimulation applications[18]. Larger areas of the microelectrode tip reduce R_s and increase C_e. Maximising C_e induces higher current, rapidly increasing SNR and paving the way to action potential recordings[18]. The need, though, to minimise the size of the electrodes in order to reduce the footprint of the device and allow to collect signals from smaller groups of neurons leads to an increased impedance, which reduces the quality of the recordings. Recent work on conducting polymers (CPs) has shown that materials such as Poly(3,4-ethylenedioxythiophene):poly(styrene sulfonate) PEDOT:PSS can be coated on top of the recording site of an electrode to significantly reduce the impedance and improve the SNR[23,24]. The unique properties of CPs, particularly the volumetric capacitance, provide a higher effective surface area and assisted in reducing the footprint of microelectrode recording devices[18].

The earliest reported recordings of neural activity date back to 1940s, when Renshaw employed metal wire electrodes to measure signals from single neurons[22]. Following that, the rapid development of semiconducting materials and the advance in microfabrication techniques gave birth to the Michigan probes[25] and arrays[26], in 1980s. Michigan probes were a stepping stone in the fabrication of microelectrodes as they offered, for the first time, the ability to implement abundant recording sites on a single shank, allowing for multiple simultaneous recordings[22]. In Michigan probes the neural activity is recorded along the whole length of the implanted shank. On the other hand, Utah arrays consist of up to 128 microelectrode needles (arrays), in which the signal is collected only from the tip of the electrodes[26].

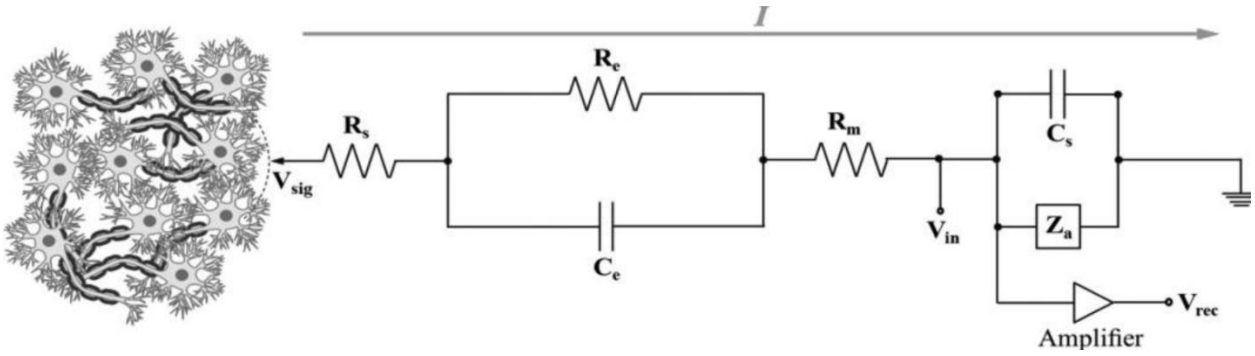

Figure 1.4 Equivalent circuit of a microelectrode recording device, used to interface with neurons. V_{sig} corresponds to the electrical signal (generated from a population of neurons), R_s is the resistance of the electrolyte (consisting of ions such as Na^+ and K^+), R_e resembles the resistance of the double layer that is created in the electrode interface (leakage resistance), C_e is the double layer capacitance, R_m is the actual resistance of the microelectrode, V_{in} is the input signal containing the recorded potential, C_s is the total shunt capacitance to the ground, Z_a is the impedance of the amplifier and V_{rec} is the final amplified signal. Image adapted from [22].

Despite their high impact, Michigan probes and Utah arrays suffer from the rigid substrates on which they are fabricated onto, exhibiting a mechanical mismatch with the neural tissue. As shown in Figure 1.5 the Young's modulus of materials such as SiO_2 and Au is much higher than neural tissues and cells. This mismatch triggers the immune system causing a foreign body response, which in turn initiates the encapsulation of the device, rapidly decreasing the quality of the recorded signal overtime. Hence, a wide variety of materials such as parylene C (PaC), polyimide (PI) and SU-8 have been employed as an alternative choice of substrates, rendering the fabricated devices "flexible" while operating as insulators. From a device perspective, performance can be affected from the degradation of the electrode materials and from mechanical stress. Mechanical stress applied during the insertion process or after the implantation can cause delamination of the electrode layers and cracking of the insulating coating[2]. The exposed parts behave in an unexpected manner inducing parasitic currents and cross-talk between different recording sites[18,22]. Another important factor is the corrosion of the electrode material, which causes failure of the recording device and can release dangerous

substances to the human body. Figure 1.6 highlights the main factors which can lead to neural probe failure. It is important to mention that other parameters originating from the biology of the human body (such as the implantation technique, the tissue micromotion, the formation of glial scars, etc.) can affect the performance of the recording devices.

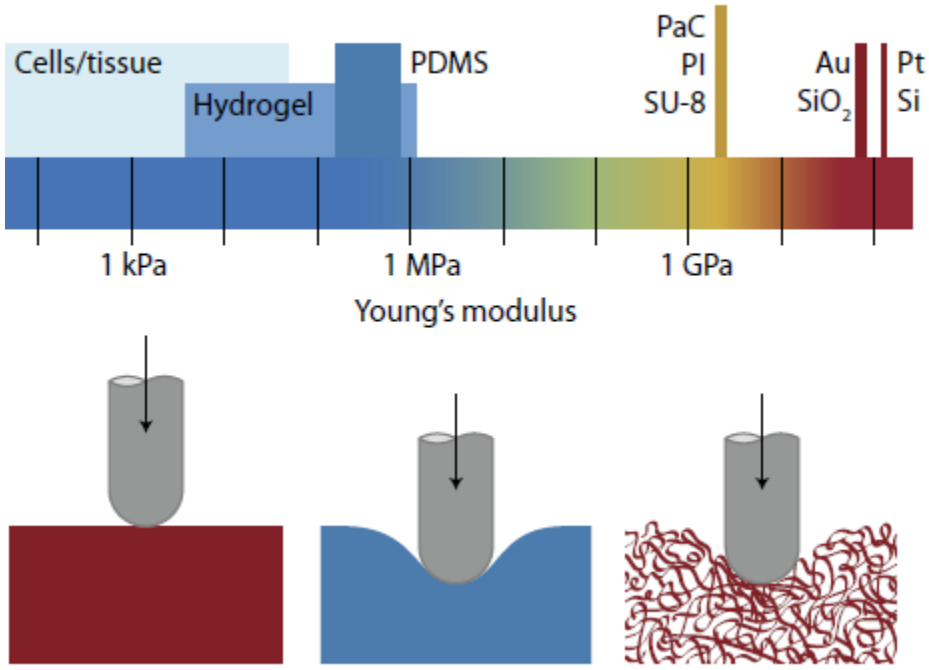

Figure 1.5 Young's modulus of different materials used in neural recording devices. Specially selected coatings can reduce the stiffness of rigid materials such as SiO_2 and Au and make them compliant. Image reproduced from [18].

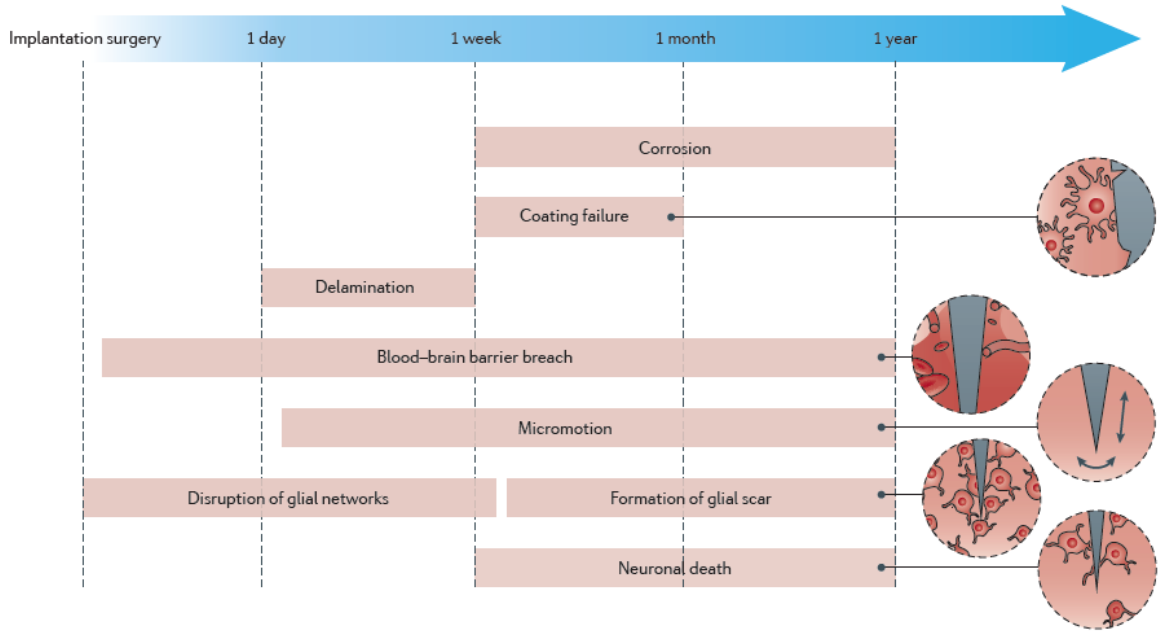

Figure 1.6 Mechanisms that lead to failure in the operation of a neural probe overtime. Image reproduced from [2].

Although microelectrode arrays have been used in a variety of medical applications, a different type of electronic device which can be used to perform recording and stimulation of the neural tissue is the transistor. The main advantage of transistors, compared to electrodes, is their ability to amplify the recorded signal as close to the recording site as possible, avoiding any extra noise that is introduced to the system by the transmission line when using an amplifier configuration. This intrinsic property of transistors can improve the SNR of the recorded signals and reduce the complexity of the signal acquisition circuit. A new type of thin film transistors the organic electrochemical transistor (OECT) has been shown to exhibit great characteristics, such as high transconductance[27] and great SNR recordings of brain activity, compared to surface electrodes[6]. The necessity to continuously improve the quality of the recorded neural signals, to further broaden our knowledge of the human brain, combined with the promising properties of OECTs render this device a fitting alternative for neural recordings.

1.4 OECTs

Since their first development in 1984 by Wrighton and colleagues[5], OECTs have attracted a significant amount of attention and have found fertile ground in various biological applications, due to their unique properties[28–30]. Their ability to convert ionic to electronic current combined with the use of a conducting polymer as the semiconductor material makes them easy to fabricate onto flexible substrates and suitable for electrophysiological monitoring[31,32].

An OECT consists of two metal contacts (Drain and Source), a semiconducting material, which establishes connection between them, and a gate electrode. The semiconducting film is in direct contact with an electrolyte, filled with mobile ions, in which the gate electrode is submerged[4] (Figure 1.7). OECTs use ions injected from the electrolyte to change the doping state and hence, the conductivity of the semiconducting film[33]. This process is controlled by the voltage applied between drain-source (V_D) and gate-source (V_G). V_D creates a current (I_D) in the channel and V_G regulates the amount of ions being injected into the channel[4]. Depending on the organic semiconductor material, OECTs can be designed to operate in two different modes: accumulation or depletion. In the accumulation mode, the drain current I_D can be considered negligible at zero gate voltage and the transistor is switched OFF. When a negative voltage is applied holes accumulate in the semiconductor, compensating the injected anions, and the transistor is switched ON[34–36]. In contrast, depletion mode OECTs are switched ON at zero gate voltage. The application of a positive voltage in the gate electrode injects cations that replace the holes flowing in the channel reducing the drain current I_D and thus, switching OFF the device[37]. Figure 1.8 illustrates the transfer curves of a depletion and an accumulation mode OECT, respectively.

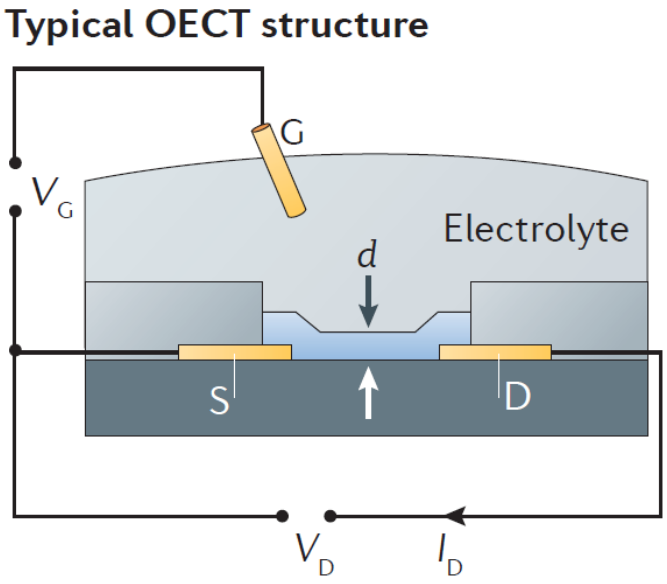

Figure 1.7 Typical OECT structure. The two metal contacts Source (S) and Drain (D) communicate through the semiconducting polymer (pointed by the white and black arrows). The gate electrode (G) is immersed into the electrolyte, which makes contact with the conducting polymer. Image adapted from [4].

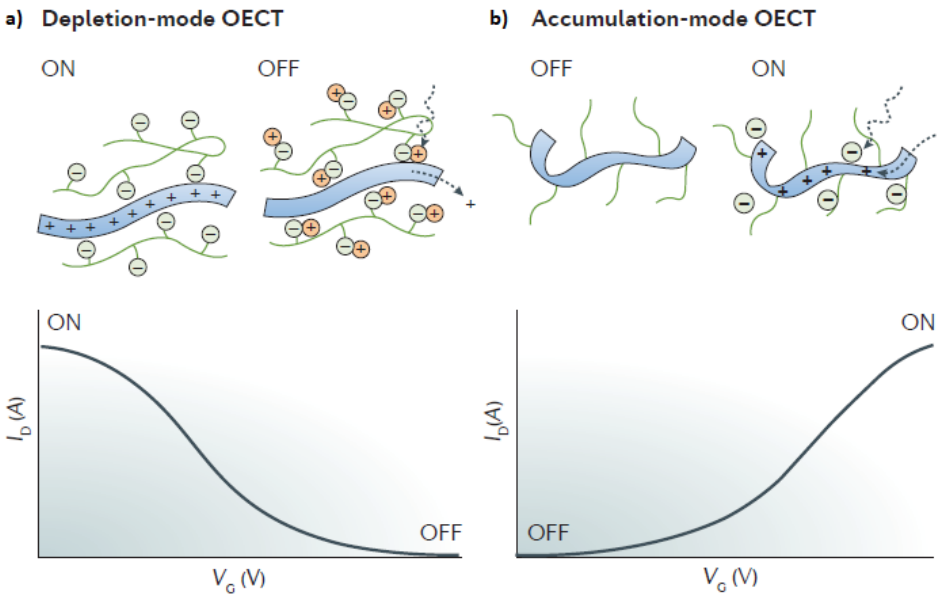

Figure 1.8 a) Transfer curve of a depletion mode OECT. The drain current I_D decreases when a positive gate voltage is applied. b) Transfer curve of an accumulation mode OECT. The drain current I_D increases when a negative gate voltage is applied. Image adapted from [4].

One of the factors that differentiate OECTs from other types of transistors is the doping-dedoping of the conducting polymer, which is performed across the entire volume of the channel (bulk)[38]. This allows the induction of high values of drain current for low gate voltages and creates the potential for OECTs to be used as powerful amplifiers, biosensors and bio actuators[27,38,39]. Most OECT architectures are defined by the typical planar structure shown in Figure 1.7. It is important, however, to mention that vertical OECTs with high transconductance values have also been reported[40]. This 3D model of OECTs has a smaller footprint and can open a door for higher density architectures in the near future. Limitations such as the parasitic series resistance between source and drain, as well as the extra complexity in the fabrication process need to be tackled first though.

1.4.1 Principle of operation and device physics of OECTs

As previously mentioned, OECTs work as transducers. The application of a signal in the gate electrode is translated in a large change to the drain current. This change is measured by the transconductance (g_m), which is the first derivative of drain current over gate voltage, $g_m = \frac{\partial I_D}{\partial V_G}$. Higher transconductance provides higher gain in the output which renders the device more sensitive to lower power signals.

OECTs have been shown to exhibit exceptionally high values of transconductance, in the order of mS, which makes them suited to record electrophysiology signals[6]. This figure of merit made OECTs extremely appealing to the research community. A comparison performed in recent work, illustrated the superior performance of OECTs in signal amplification by evaluating the transconductance of different types of transistors[27] (Table 1).

Active material	Dielectric material	$\|V_D\|$ (V)	g_m (µS)	$g_m/\|V_D\|$ ($\mu S*V^{-1}$)
Aqueous electrolyte				
PEDOT:PSS (~400 nm thick)	NaCl	0.6	8000	13333
PEDOT:PSS (~100 nm thick)	NaCl	0.6	2000	3333
Graphene[41,42]	PBS+NaCl	0.1	420	4200
Diamond[43]	PBS+KCl (in vitro)	0.2	18	90
Silicon[44]	$SiO_2/Ti0_2$ (in toto)	0.25	15	60
Silicon nanowire[45]	SiO_2, PBS	0.03	5	167
Ionic liquid/gel, solid electrolyte				
ZnO[46]	IL (DEME/TFSI)	0.1	160	1600
ZnO nanowire[47]	Solid electrolyte (PVA/$LiClO_4$)	0.5	2.79	5.58
Organic semiconductor: P3HT[48,49]	IL (EMIM/TFSI) gel (PS-PEO-PS)	1	50	50
Solid state				
ZnO[50,51]	Al_2O_3	4	1400	350
Graphene[52–54]	SiO_2 (bottom gate); Y_2O_3 (top gate)	2	1863	932
III-V nanowire: n-InAs nanowire[55,56]	SiN_x	1	97.5	98
III-V Bulk: GaN/InAlN[57–59]	SiN_x	2	-	-
Carbon nanotube (mat)[60,61]	HfO_2	0.5	50	100
Organic semiconductor: DNTT[62–64]	AlO_x/SAM	2	12	95
Silicon nanowire[65]	SiO_2	-	2	-

Table 1 Illustration of the variation of transconductance in different transistor types. Table adapted from[27].

Bernards and Malliaras proposed a model to describe the behaviour of depletion mode OECTs[33]. The operation of an OECT was divided into two circuits: the first one describing the behaviour of the device based on solid state physics (electronic circuit) and the second one describing the exchange of ions based on electrochemistry (ionic circuit). Figure 1.9 illustrates the schematic of an OECT.

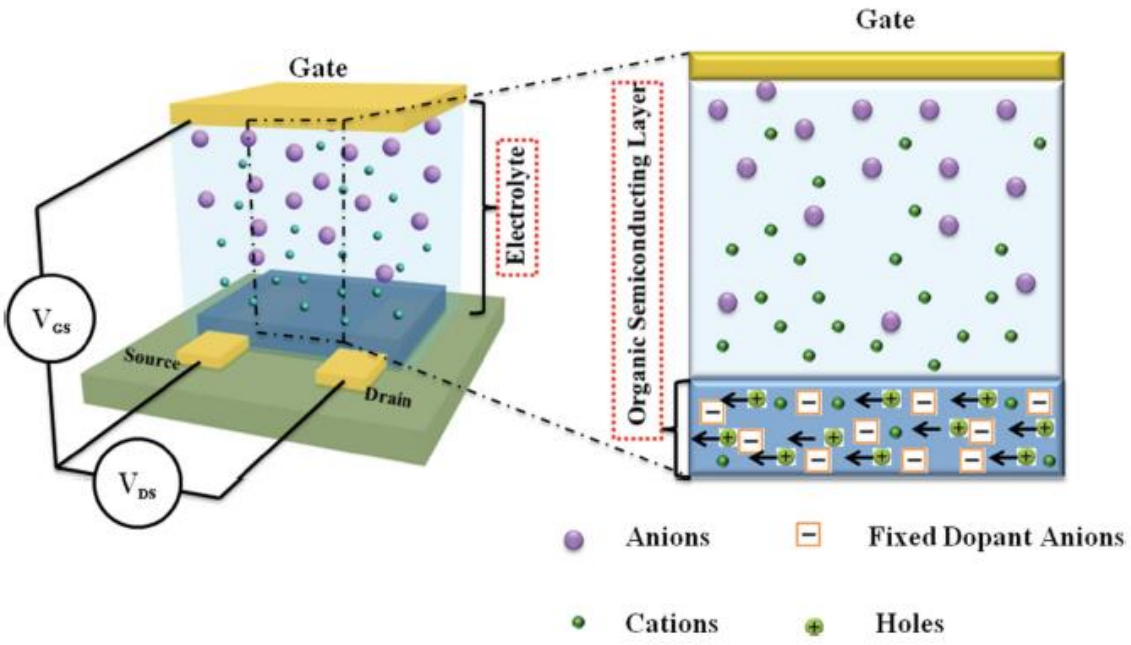

Figure 1.9 Schematic representation of the behaviour of an OECT. A bias voltage is applied to drain contact while source is grounded. The current flowing in the channel can be modulated by applying different gate voltages. When a positive gate voltage is applied, cations from the electrolyte are injected into the channel dedoping the semiconducting film, leading to a reduction in the drain current. Image adapted from [32].

The electronic circuit is examined by applying Ohm's law whereas the ionic circuit is modelled as a resistor in series with a capacitor. The equivalent circuit combines the principle of operation of a typical transistor such as a MOSFET (metal oxide semiconductor field effect transistor) and an ideal polarisable electrode[33] (Figure 1.10).

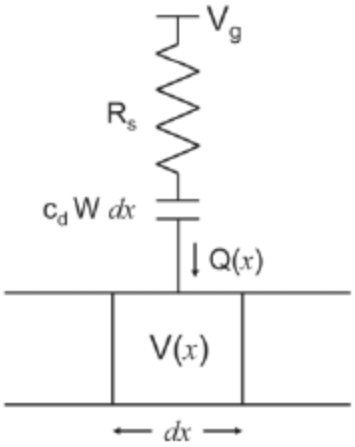

Figure 1.10 Ionic circuit of an OECT showing the charge Q being injected into the channel of the transistor. Image adapted from [33].

The thickness of the semiconducting polymer has been examined extensively, as Bernards' model indicates that transconductance is proportional to the thickness of the channel[33]. In the saturation regime transconductance is given by[66]:

$$g_m = \frac{W}{L} * d * \mu * C * (V_{TH} - V_G),$$

where W is the width of the channel, L is the length, d is the thickness, μ describes the mobility of the holes or electrons, C is the capacitance per volume (F/m^3), V_{TH} is the threshold voltage and V_G is the voltage applied to the gate electrode with reference to the source. Understanding the meaning of this equation is of paramount importance in identifying the advantages and disadvantages of OECTs. The form of the equation is similar to those describing other types of transistors such as MOSFETs with the exception of the thickness factor (d). In OECTs, transconductance is affected by the volume of the conducting polymer whereas in other transistors it is only affected by the channel ratio (W/L) and the capacitance per surface area (F/m^2). Hence, the high signal amplification in OECTs originates from the volumetric coupling of the conducting polymer compared to organic field effect transistors (OFETs), in which the presence of a dielectric layer prohibits the injection of ions into the channel.

Rivnay et al. was one of the first to analyse the influence of geometry on maximising transconductance[39]. OECTs with different widths (W), lengths (L) and polymer thickness (d) were fabricated. Careful examination of the results showed that the voltage at which the device reaches a peak in transconductance depends on the W/L ratio and the polymer thickness. The surface area was found to not affect the measurements. From an engineering perspective, the findings of this study allow us to tune the geometry of OECTs in order to achieve the highest signal amplification in a designated gate voltage V_G (for constant V_D) and thus, actively set the desired bias conditions (Figure 1.11).

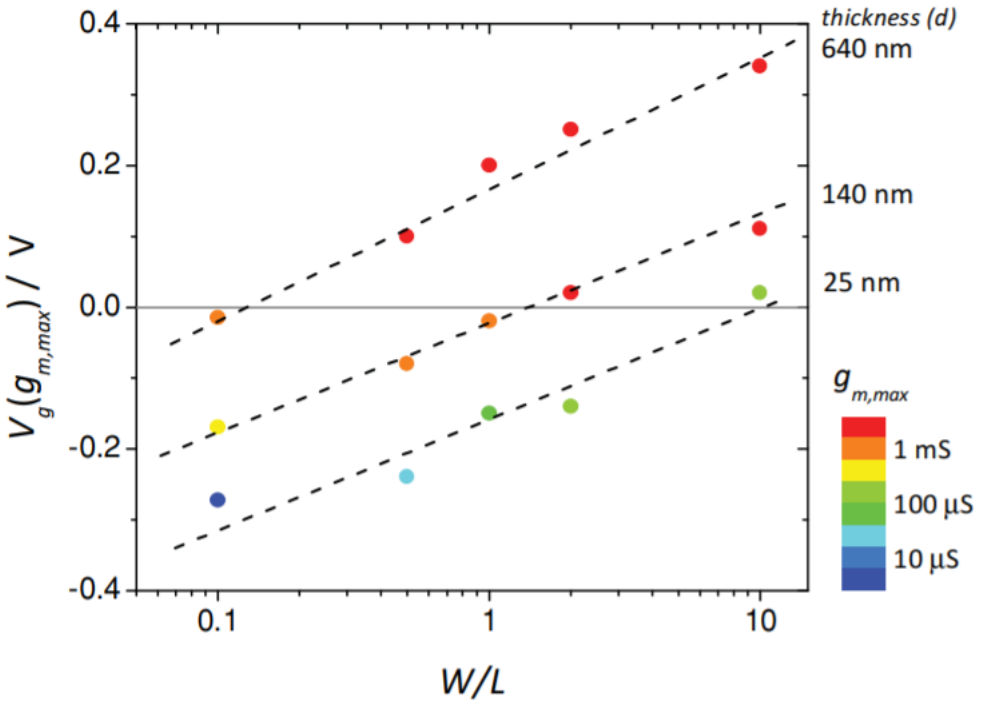

Figure 1.11 Optimising the W/L ratio and the polymer thickness to achieve maximum transconductance at 0 gate voltage. Image adapted from[39].

In a more recent study, researchers utilised the thickness dependence of transconductance to fabricate OECTs with enhanced performance[67]. The results showed that capacitance in OECTs scales proportionally to the volume and can reach high values up to 39-40

F/cm^3; a value that is 100 larger than the equivalent capacitance per unit area of 500 µF/cm^2 for a 130 nm thick PEDOT:PSS film (Figure 1.12).

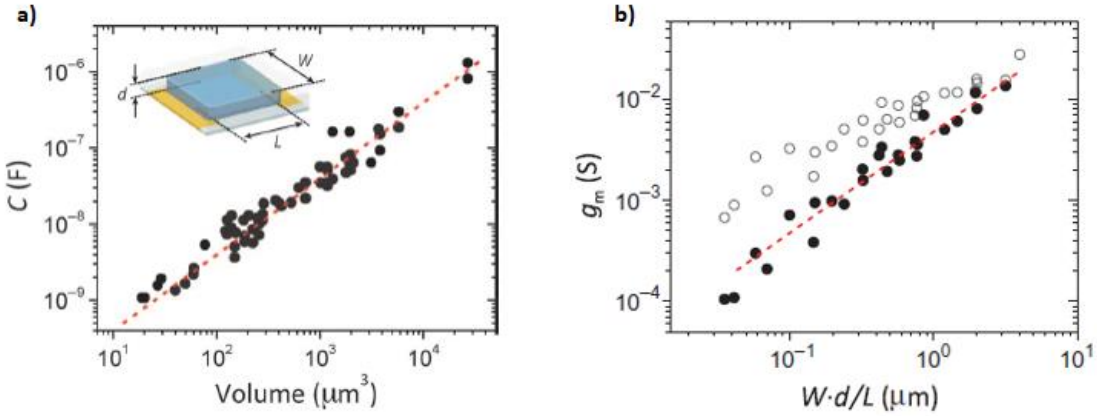

Figure 1.12 a) Capacitance dependence of PEDOT:PSS for OECTs of different volume. b) Transconductance behaviour for OECTs with different geometry. White dots correspond to the maximum transconductance values measured while black dots correspond to transconductance values in the saturation regime. Image adapted from [67].

Bernards' model provides an easy and effective way to analyse how different parameters can affect the performance of an OECT but cannot fit in every occasion. A typical example is the non-monotonic curve of the transconductance. Based on Bernards' model, transconductance should be constant in the linear regime and reduce linearly in the saturation regime[33]. However, transconductance exhibits a bell-shaped curve. Kaphle et al. proposed that the resistance of the contacts can be one of the main factors leading to this bell-shaped curve. An exponential increase of the contact resistance over gate voltage was observed, signifying that the contact resistance dominates the total resistance of the device, up until a gate voltage high enough is applied to dedope the semiconducting film[68]. Further investigation demonstrated that although this may be

the case for some p-type semiconductor materials, such as PEDOT:PSS, this trend is not observed in every p-type conducting polymer, for example p(g2T-TT). It was shown that the influence of disorder on the electronic transport in the channel of the semiconducting polymer is the main reason for the shape of the transconductance curve, suggesting that this is an intrinsic characteristic of OECTs[69]. A model based on hopping transport with a Gaussian-shaped density of states (DOS) was employed to provide a better fit between the experimental and the theoretical results of the output curves of OECTs.

Furthermore, Bernards' model treats the electronic circuit of an OECT as a resistor with the value depending on the voltage applied, assuming that the carrier mobility is constant. Despite the fact that this assumption simplifies the analysis of the circuit, it does not reflect the behaviour of conjugated polymers. A non-uniform model of carrier mobility has been developed providing a better fit with the output curves of OECTs[70]. In addition, the ionic circuit of the model needs to be examined more carefully. The use of a polarisable electrode and the nature of the OECT channel introduce a pair of capacitors: one between the gate and the electrode (double layer) and another one expressing the volumetric capacitance of the channel[4]. Previous studies conducted in OECTs employing different fabrication methods (photolithography and inkjet-printing) demonstrated that the material and the surface area of the gate electrode can directly influence the response of an OECT[71,72]. Transistors exploiting larger channel areas demonstrated higher sensitivity in sensor applications[71]. The materials of the gate electrode were Pt and PEDOT:PSS on PET (polyethyleneterephthalat), respectively. As the two capacitors formed in an OECT are in series and the value of the capacitance is proportional to the surface area, with the resistance being inverse proportional to the capacitance, we expect a voltage drop on the capacitor with the lowest value. As a result, Ag/AgCl non-polarisable electrodes that exhibit negligible voltage drop between the gate and the electrolyte have been introduced to achieve a more effective gating[73].

Finally, one of the major drawbacks of OECTs is the response time. The volumetric nature of OECTs endows them with high transconductance but also with slow ON/OFF operation ratio. It has been shown that the response time of an OECT scales with the area and the thickness of

the conducting polymer (volumetric dependency)[67]. This renders the use of OECTs in high frequencies unsuitable. Khodagholy et al. however, fabricated OECTs with response times in the range of hundreds of μs[74], making them an appealing option for electrophysiology signal recordings[6].

1.4.2 Semiconducting materials of OECTs

Since the fabrication of the first accumulation mode OECT using polypyrrole as a semiconducting film,[5] a variety of different materials have been explored. Despite being challenging to categorise all of the materials using well-established criteria, previous work has successfully benchmarked the majority of them by utilising their transconductance characteristics[66]. As mentioned above transconductance is given by:

$$g_m = \frac{W}{L} * d * \mu * C * (V_{TH} - V_G).$$

For similar device geometry and operating conditions, it is the product μ*C of carrier mobility and capacitance per unit of volume that can be used to identify the intrinsic characteristics of different polymers. Figure 1.13 summarises the results of this study. With the highest carrier mobility observed, μ*C product really close to the top performing material, easy processing methods and commercial availability, Poly(3,4-ethylenedioxythiophene):poly(styrene sulfonate) (PEDOT:PSS) stands out as one of the top semiconducting organic film candidates.

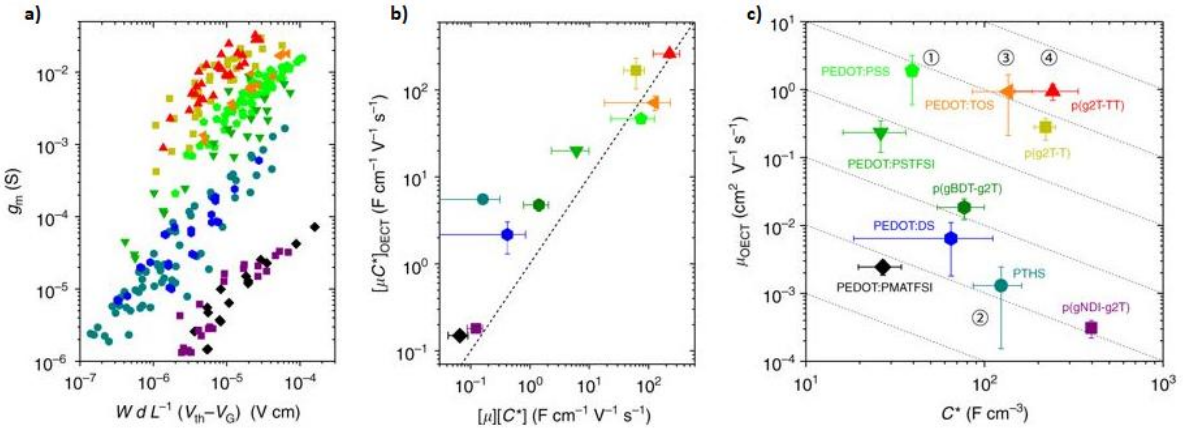

Figure 1.13 a) Dependence of transconductance on the geometry of the device and the applied voltage. The slope of this graph represents the product (μ*C). b) The product (μ*C) as a function of independent measurements of the carrier mobility (μ) and the capacitance per unit volume (C). The dashed line indicates a good fit for most of the polymers. c) Carrier mobility (μ) vs. volumetric capacitance (C) for all the examined materials. Image reproduced from [66].

1.4.3 PEDOT:PSS

PEDOT:PSS is a polymer formed by polymerising the monomer 3,4-ethylenedioxythiophene in the presence of a water soluble polyanion, poly(styrene sulfonate) (PSS)[75] (Figure 1.14). Although PEDOT is a conjugated polymer and is not soluble in water, the polymerisation with PSS creates an aqueous dispersion which can be exploited to spin-coat PEDOT:PSS on the surface of a substrate or use it as an ink to print multiple layers. In commercially available solutions, the negative charge of PSS chains is greater than the positive charge of PEDOT chains, categorising the material as a p-type semiconductor[75].

PEDOT:PSS has been extensively used to develop bioelectronics devices for electrophysiology, such as electrodes, OECTs and biosensors[38,76,77]. Its low toxicity level and biocompatibility have also been explored *in vitro* in different types of cells[78–80]. Enhancing the electrical conductivity, ensuring long term stability and uniformity of the semiconducting film is

of paramount importance for bioelectronic applications. Hence, different materials such as ethylene glycol[81], dimethyl sulfoxide[82], sorbitol[83], dodecyl benzene sulfonic acid (DBSA)[1] and (3-glycidoxypropyltrimethoxysilane) GOPS[77] have been employed to further improve the performance of PEDOT:PSS films. For all these reasons PEDOT:PSS has become one of the most commonly used organic polymers in the bioelectronics community[84]. It should be noted though that more research needs to be undertaken to ensure that the degradation of PSS chains does not lead to the release of deleterious compounds in long term applications[85].

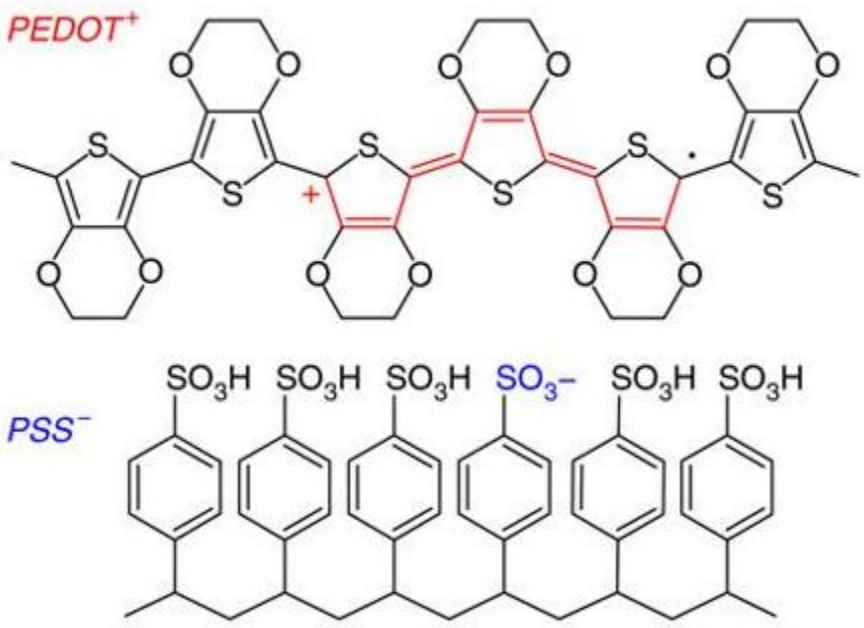

Figure 1.14 Chemical structure of PEDOT chain (top) and PSS chain (bottom). The excess of positive charges in PEDOT is compensated by the negative charges of PSS. Image adapted from [27].

1.4.4 Applications of OECTs

OECTs operate at low working voltages (less than 1V) and yet amplify the drain current by several orders of magnitude[86,87]. They can also be fabricated by low-cost materials and be implemented onto flexible substrates[31]. All of these properties combined with their ability to

translate ionic to electronic current made them a promising candidate for multiple biological applications. In this section, we will briefly highlight some representative applications of OECTs.

To begin with, Khodagholy et al. explored the ability of OECTs to amplify signals on the spot of the recording site and measured enhanced quality signals coming from brain activity of rats[6]. He showed that OECTs cannot only be fabricated onto flexible substrates, capable of being implanted into human brains, but can also provide higher SNR compared to electrodes (Figure 1.15 a,b,c,d). Following that, researchers illustrated that OECTs can be employed to stimulate neurons in a minimally invasive way in the hippocampus, paving the way for potential medical applications[7]. OECTs have also been used for fibre and cutaneous applications such as saline sensing on single cotton threads[88] (Figure 1.15 e), nylon fibre glucose sensors[89] and electrocardiograms on human skin[90]. Lin et al. illustrated the dependence of OECTs output current on the concentration of the electrolyte solution[91]. An increase in the concentration leads to a decrease of the drain current, which can be explained by the ionic behaviour of OECTs and can be utilised to implement ion sensors. Another study, focused on ion detection sensors, demonstrated how OECTs can be used to provide high sensitivity for low operating voltage, reporting a value of 1200 $mVV^{-1}dec^{-1}$ (normalised value for ion sensitivity over supply voltage), the highest ever observed in ion-sensitive transistors[92]. DNA sensors that detect complementary DNA targets using OECTs and microfluidic channels have also been developed[93]. Single strands were immobilised on the gate to assist with the sensing. Furthermore, Yao et al. used OECT arrays to record ion transport in epithelial cells, investigating potential applications of OECTs in drug delivery[94]. Finally, recent work demonstrated that OECTs can be used as transducers to characterise interactions between biological molecules and cell membranes[36]. It was demonstrated that the formation of a lipid membrane prohibits ion transportation, leading to a significantly reduced drain current in the saturation regime (Figure 1.15 f,g).

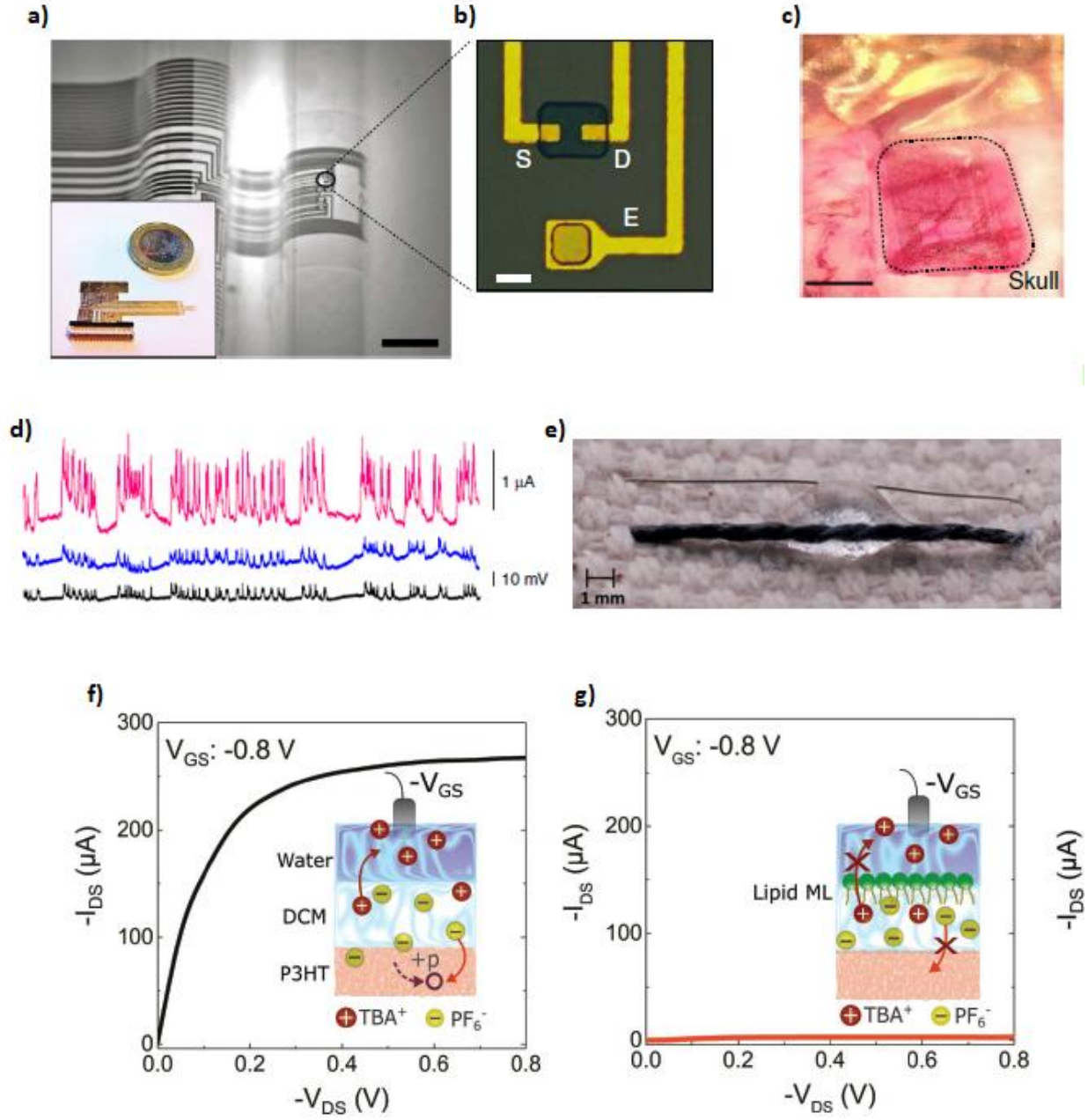

Figure 1.15 Summary of OECT applications. a) Image of a flexible probe, consisting of OECTs and microelectrode arrays. b) Optical microscopy image showing the structure of an OECT (drain and source contacts) and a surface electrode. c) Optical micrograph of an ECoG probe placed on the cortex. Dashed lines highlight the craniotomy area. d) Signals of brain activity recorded by an OECT (pink), a PEDOT:PSS surface electrode (blue) and an Ir-penetrating electrode (black). The quality of the signals collected by an

OECT surpasses the ones measured by surface electrodes, providing a much higher SNR. Images adapted from [6]. e) Single cotton thread OECT. The silver wire (top) corresponds to the gate of the OECT while the black PEDOT:PSS wire (bottom) implements the Source-Drain contacts. An electrolyte is placed between them to establish connection. Image adapted from [88]. f) Output curve of an OECT in the saturation regime before the formation of a lipid monolayer (gate voltage was kept constant at -0.8V). g) Output curve of the same OECT after the formation of a lipid monolayer. A significant reduction in the saturation drain current is observed. Images adapted from [36].

1.5 Noise in electronic devices

Noise can be defined as "any unwanted disturbance that obscures or interfaces with a desired signal"[95]. Noise in electronic devices behaves as a random signal, which suggests that its waveform cannot be predicted or be quantified in any instant of time. However, different approaches have been developed to tackle this problem, providing distributions which examine the probability of a signal to have a specific value at a designated point of time[95]. Analysing how different types of noise can affect the behaviour of an electronic device can provide us with crucial information about the intrinsic properties of the device itself, as well as pave the way to an enhanced, optimised performance. In this section, we will focus on two different types of noise, thermal and flicker, as they are the most commonly addressed in organic devices.

1.5.1 Thermal noise

Thermal noise was first investigated by Johnson and Nyquist in 1928. Their preliminary studies in a resistor showed that noise was generated by the thermal motion of charge carriers in a conductor, inducing random fluctuations in the current[96]. This phenomenon is independent

of the applied voltage and is treated as an intrinsic property of every material. The equation describing thermal noise is given below:

$$S_V = 4k_B TR\Delta f,$$

where S_V is the voltage power spectral density (PSD), k_B is Boltzmann's constant, T is the temperature in Kelvin, R is the resistance of the device and Δf is the frequency bandwidth. A simple conversion can be implemented to provide the current PSD ($S_I = 4k_B T/R$). Thermal noise exhibits a constant spectral density across the whole spectrum of frequency, behaving identically to white noise. Despite the fact that the nature of thermal noise itself makes it impossible to be alleviated or even minimised, it is of paramount importance to carefully examine its PSD, as a misinterpretation can lead to incorrect conclusions when studying the noise behaviour of a device[97].

1.5.2 Flicker noise

Flicker noise is a type of noise that appears in multiple electronic devices and has been shown to be inverse proportional to the frequency (also called 1/f noise). Its existence has been identified by studies performed in light emitting diodes[98], MOSFETs[99], TFTs[100], etc. However, the explicit source that originates flicker noise has not been specified yet. Different theories have been proposed in an attempt to explain the behaviour of different devices. McWhorter studied the effects of flicker noise in germanium and suggested that the origin of 1/f noise is the fluctuations between the semiconducting material and the oxide layer (insulator in semiconductor devices)[80]. This suggestion implies that the fluctuations are caused by the trapping-detrapping of charge carriers inside the oxide, affecting electrons tunnelling trough the semiconductor-oxide interface (carrier number fluctuations model)[97]. A few years later, Hooge, having experimented on resistors and semiconductors, proposed a model using an empirical relationship to correlate the PSD with the frequency and the voltage/current applied[102]. The equations describing this model are listed below:

$$\frac{S_I}{I^2} = \frac{S_V}{V^2} = \frac{a}{fN}$$, (eq. 1)

where α corresponds to the Hooge parameter, f is the frequency and N stands for the total amount of free charge carriers inside the material. Hooge's model suggests that fluctuations in the mobility of the carriers, induced by charge scattering cross section, are directly translated into fluctuations in the drain current (mobility fluctuation model)[103,104]. Despite the fact that most of the findings found in the literature are based on inorganic semiconductors, the mechanisms used in these devices can also be applied to analyse noise in organic electronics.

1.5.3 Noise analysis in organic transistors

Vandamme et al. was one of the first to describe the effects of noise in organic semiconductors. With his colleagues they analysed how 1/f noise affects the performance of pentacene and poly-thienylene vinylene (PTV) transistors. For PTV transistors, it was found that they exhibit a 1/f slope for frequencies higher than 3 Hz under different bias conditions, by varying V_{DS} while keeping V_{GS} constant (Figure 1.16). To ensure that PTV transistors comply with the mobility fluctuations model, different plots were acquired showing that the normalised current noise (S_I/I^2) is inversely proportional to the applied gate voltage V_{GS} and to the length of the channel L (Figure 1.17). This study provides a quick and effective guide to test if the empirical relationship, proposed by Hooge, is applicable in the devices under test. Both the applied voltage (V_{GS}) as well as the geometrical characteristics of the transistor (L) can provide us with an insight of the intrinsic noise properties of the devices. Another way to examine the applicability of Hooge's model is a direct comparison of the current PSD (S_I) with the square of the current. This type of measurement can assist in identifying the noise level of different device architectures, such as bottom contact vs. top contact TFTs[105]. However, a huge disadvantage of this approach is that it may lead to incorrect assumptions when comparing devices coming from different batches, where the fabrication conditions might not have been exactly similar.

Furthermore, using Hooge's model, Marinov et al. proposed a figure of merit in which a normalisation over the surface area of the channel (W*L) can be employed to categorise more accurately different semiconductor materials, based on the fact that N scales proportionally to the area of the channel[106]. His hypothesis was that the main parameter contributing to the mobility fluctuations was the hopping of carriers in the polymer film. The proposed figure of merit ($\frac{S_{ID}}{(V_{DS}*I_D)/(W*L)}$) quantifies how the bias voltage applied is converted into 1/f current noise per unit of surface area. Moreover, a more recent study revealed that noise in pentacene transistors shows an inverse proportionality to the applied gate voltage, in transistors with different channel thicknesses[107]. The results of that study illustrated that the noise spectral does not depend on the channel thickness, which can be probably explained by the fact that in TFTs the gate voltage is translated into a field effect doping of the semiconductor (a sheet of charged carriers is created but there is no ionic exchange as in OECTs).

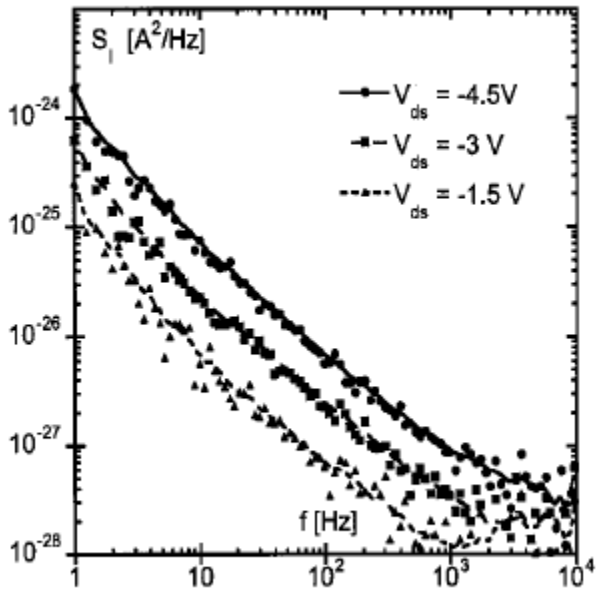

Figure 1.16 Power Spectral Density acquired by measuring the output current in a PTV sample (S_I) for different bias conditions (V_{DS} = -4.5, -3, -1.5 V). The plot indicates that the PSD is inverse proportional to the frequency (1/f slope). Increasing the applied V_{DS} leads to an increase in the current which in turn generates more noise in the device. Image reproduced from [108].

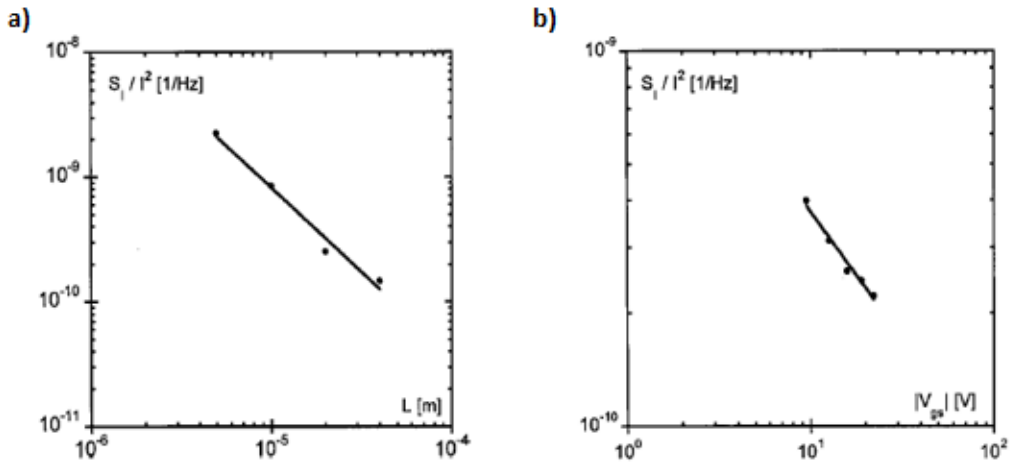

Figure 1.17 a) Normalised Power Spectral Density (S_I/I^2) showing the dependency of noise on length. An inverse proportional relationship is observed in agreement with Hooge's model as $N \propto L$ and $S_I/I^2 \propto 1/N$, which suggests that $S_I/I^2 \propto 1/L$ (taken at f = 1Hz, V_{DS} = -3 V, V_{GS} = -15.9 V and same width for all the examined devices). b) Normalised Power Spectral Density (S_I/I^2) showing the dependence of noise on the applied gate voltage (V_{GS}). Similarly an inverse proportional relationship is expected as $N \propto V_{GS}$. Image adapted from [108].

1.5.4 Noise in OECTs

As mentioned above, analysing the noise characteristics of OECTs in order to enhance their performance is one of the major goals of this study. Based on a recent study, OECTs exhibit 1/f noise in lower frequencies (Figure 1.18) and their behaviour can be described by a charge-noise model[109]. In all of the experiments performed V_D was kept constant at 100mV whereas the transistor was gated to different resistance values by changing the gate voltage. More focus was placed on the so called "channel regime" which corresponds to the subthreshold regime of a transistor (V_G > 0.35V, approximately).

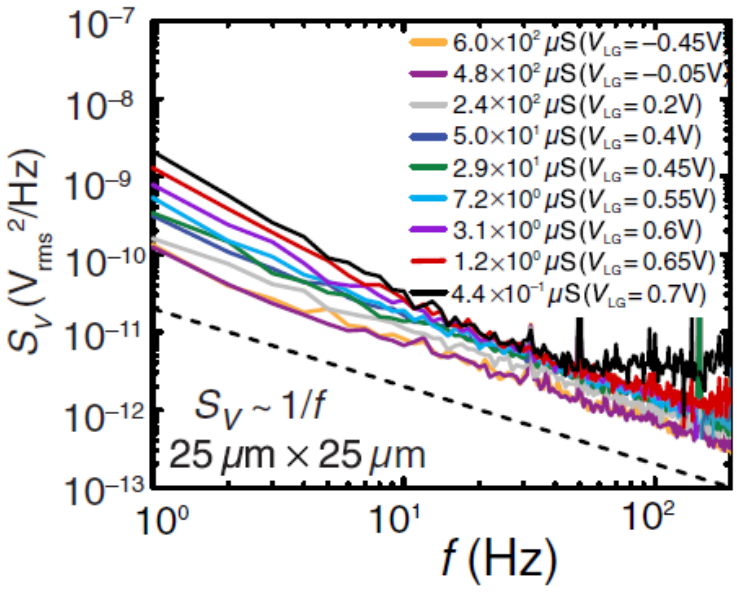

Figure 1.18 Power spectral density of the voltage fluctuations (S_V) for different frequencies, showing a 1/f dependence. Image adapted from [109].

Two different models were examined to identify which one fits better the behaviour of an OECT. The first one is called the a-noise model (which corresponds to Hooge's law) and can be expressed as:

$$\frac{S_I}{I^2} = \frac{a}{fN} = \frac{a}{fpwld} = \frac{ae\mu V_D}{fIl^2}, \text{ (eq. 2)}$$

where N=pwld (p represents the hole density and wld is the volume of the channel) and the final form of the equation can be obtained by applying Ohm's law and substituting the conductivity, σ=epμ. From eq. 2 we extract that normalised noise is inverse proportional to the output current, measured in the drain contact, for a standard device geometry and a constant bias voltage (V_D). Figure 1.19 illustrates the experimental data and the fit of the a-noise model (green line). As it can be seen the a-noise model cannot sufficiently describe the acquired data and thus, a different approach needed to be examined.

An alternative model that was applied and showed a better fit, at least in the channel regime, was the charge noise model which was previously used to describe the noise characteristics of graphene transistors[110]. This model was intially developed by Tersoff to describe the noise behaviour of electrolyte gated transistors[111]. The charge noise model assumes that fluctuations in the drain current are caused by a fluctuating liquid-gate voltage (number fluctuation model)[112]. The equation that quantifies this model is given below:

$$\frac{S_I}{I_D^2} = \frac{g_m^2 S_{Vg}}{I_D^2} = \frac{g_m^2 S_q}{I_D^2 C_{gate}^2}, \text{ (eq. 3)}$$

where g_m is the transconductance of the transistor, S_{VG} is the gate referred voltage noise and I_D is the drain-source current. This relationship between the PSD and the transconductance of an OECT can also be seen in Figure 1.19. The model starts to roll off as the transistor enters the contact regime, in which the contribution of the gold contacts is significantly higher[68]. From a critical point of view, despite the fact that this model seems to provide a better fit than the empirical relationship, it suffers from limitations such as the relatively small bandwidth of the examined regime (V_G > 0.35 V) and the significant deviations observed for higher drain currents (Figure 1.20).

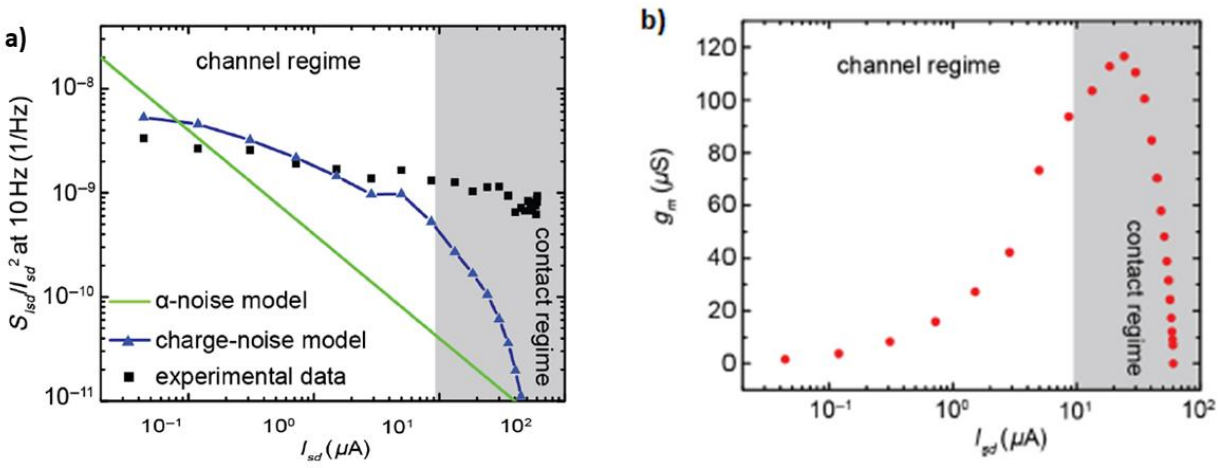

Figure 1.19 a) Normalised current noise (S_I/I^2) vs. drain current (I_{SD}) at 10 Hz. The green line corresponds to the a-noise model (following Hooge's law) whereas the blue triangle dots correspond to the charge noise

model. A better fit is observed in the channel regime by applying the charge noise model. b) Transconductance (g_m) vs. drain current (I_{SD}). Image adapted from [109].

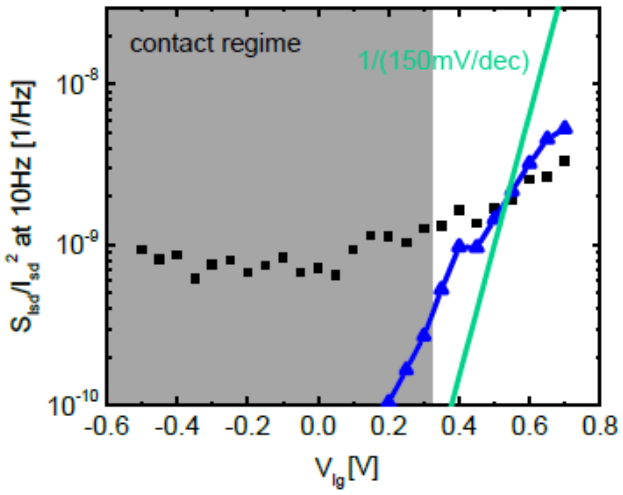

Figure 1.20 Normalised current noise (S_I/I^2) vs. gate voltage (V_{GS}). The green line shows the prediction of the a-noise model whereas the blue line corresponds to the charge-noise model. Image adapted from the supplementary information of [109].

Having proposed a model to explain the noise behaviour of OECTs, Stoop et al. and his colleagues studied how the device geometry can affect noise in OECTs. As shown in Figure 1.21 a) the PSD remains stable in the channel regime for varying resistance values. Similar conclusions were drawn for the dependency of the PSD on the channel thickness (Figure 1.21 b). It should be noted that although the ratio of the thickness between the two measured devices (thick channel/thin channel) was approximately 13, the transconductance ratio $g_{m,thick}/g_{m,thin}$ was found to be approximately 2.5.

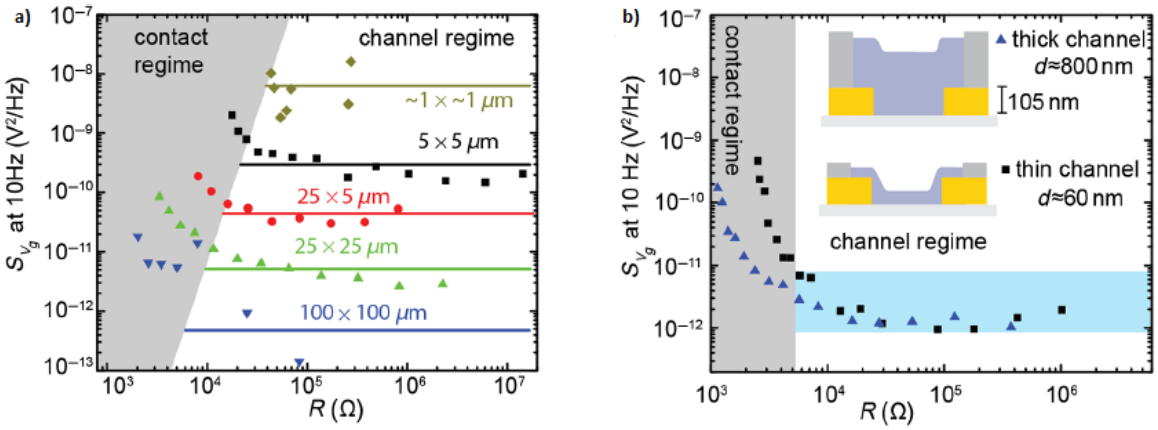

Figure 1.21 a) Gate referred voltage noise (S_{VG}) plotted vs. resistance at 10 Hz, for devices with different channel dimensions. The noise level scales inverse proportionally with the surface area of the channel (W*L) b) Gate referred voltage noise (S_{VG}) plotted vs. resistance at 10 Hz for 2 devices with different channel thickness. Image adapted from [109].

Chapter 2

Methods and materials

2.1 Fabrication

The fabrication of OECTs was based on previous publications[6,27,113] and included the deposition of gold, parylene C (PaC) and PEDOT:PSS in several subsequent steps. 26 x 76 mm^2 glass slides (Knittel Glass) were used as the substrate of the devices after they were thoroughly cleaned. The cleaning process involved an ultra-sonic bath in a Micro 90 (Cole Parmer) - deionised water (DI) low concentration solution (2%) for 20 minutes. Following that, the samples were rinsed with DI water, immersed into an acetone - isopropyl alcohol (IPA) solution (90%-10%) and were sonicated for another 20 minutes. To pattern the metal pads, a negative photoresist (AZ nLOF2035, Micro-Chemicals GmbH) was spun on the glass substrate at 4000 rpm for 30 seconds, baked at 110^oC for 1 minute and was exposed to UV light under constant power (80mJ/cm^2), using a mask aligner (Karl Suss MA/BA6). The exposed samples were post-baked at 110^oC for 1 minute and were developed using a MIF 726 developer. Having completed the development of the first layer, the samples were activated for 2 minutes using an O_2 plasma cleaner (Diener Electronic Femto), before being placed inside an e-beam evaporator (Kurt J Lesker PVD-75) to start the deposition of gold. A thin layer of Ti (5nm) was deposited on the glass substrate, followed by 100 nm of gold. The gold structures were fully formed after performing an overnight lift-off process, using a Technistrip® NI555 (Micro-Chemicals GmbH). Before proceeding with the deposition of the two layers of PaC, the samples were activated again for 2 minutes (O_2 plasma cleaner). An adhesion promoter, 3-(trimethoxysilyl)propyl methacrylate (Sigma Aldrich A-174), was used as to ensure that the first layer of PaC would not be removed during the peel-off process.

The samples were submerged in the solution for 30 secs and were hard baked for an hour in 70^{o}C, using a hot plate. Subsequently, they were placed in a parylene coater (SCS) to deposit the two layers of PaC. An anti-adhesive layer (2% v/v soap solution) consisted of Micro 90 and DI water was spun at 1000 rpm between the two layers of PaC. To pattern the PEDOT:PSS channels, a layer of photoresist (AZ9260, Micro-Chemicals GmbH) was spun on top of PaC at 4500 rpm for 30 seconds and was post baked at 110^{o}C for two minutes. The samples were exposed to UV light under constant power, using a mask aligner (MA/BA6), and were developed for 6 minutes, using a MIF 726 developer. The OECT channels were formed by reactive ion etching (Oxford 80 Plasmalab plus).

For the preparation of PEDOT:PSS, 19 ml of Clevios PH1000 (Heraeus), 1 ml of ethylene glycol, 50µl of dodecyl benzene sulphonic acid (DBSA, Sigma Aldrich) and 0,2 ml of (3-glycidyloxypropyl)trimethoxysilane (GOPS, Sigma Aldrich) were mixed and sonicated for 15 minutes. The PEDOT:PSS dispersion was spun at 3000 rpm for 30 seconds on the activated surface of OECTs and was annealed at 110^{o}C for 1 minute. To finalise the fabrication of OECTs a peel-off technique was used to remove the top sacrificial layer of PaC[114]. Finally, the samples were hard baked at 130^{o}C for an hour before being immersed into DI water to remove any excess compounds.

In order to fabricate flexible devices (Chapters 5 & 6), we followed the same process as described above for glass slides with the following changes. 1)The substrate that was employed for flexible devices was a 4 inch silicon wafer, 2) an extra layer of PaC was deposited on top of the silicon wafer (to allow the device to be lifted from the substrate), 3) an extra step of photolithography was used to define the outline of the OECTs. 4) An AZ 5214 E image reversal photoresist was employed to pattern gold. The photoresist was spun at 4000 rpm for 30 seconds, before proceeding with a soft bake at 100^{o}C for 1 minute. A subsequent image reversal bake at 110^{o}C for 2 minutes was performed after the exposure of the photoresist. To complete the pattern, the image was reversed by flood exposing the devices under the same mask aligner (<200 mJ>cm^{2}). The transistor contacts were formed by employing an AZ 351B MIF developer. 5) AZ 9260 was replaced by AZ 10 XT 520 cP positive photoresist, spun at 3000 rpm, followed by a

soft bake at 110°C for 2 minutes. Figure 2.1 shows the subsequent steps used to fabricate a flexible device (from left to right).

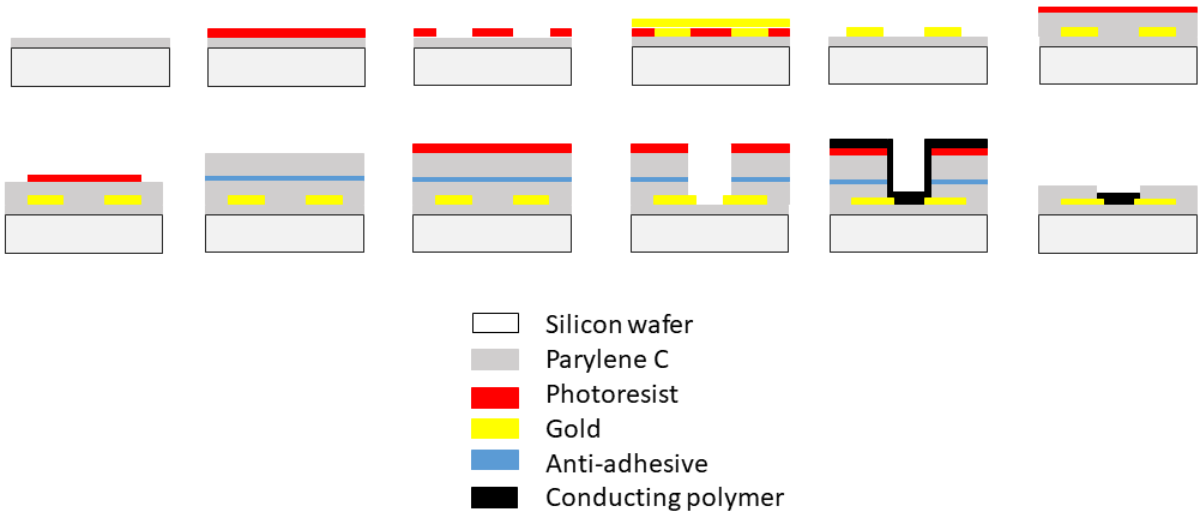

Figure 2.1 Illustration of the different steps of the fabrication process.

2.2 Characterisation

The PEDOT:PSS film area, including the total length of the stripe as well as the width and length of the actual channel, was measured using an optical microscope (Nikon Eclipse LV100ND). A DektakXT® stylus profilometer (Bruker) was used to measure the thickness of the PEDOT:PSS. Transistors were characterised using a 0.01 M Phosphate Buffered Saline (PBS) solution and a Ag/AgCl gate electrode (World Precision Instruments). A semiconductor device analyser (Keysight B1500A) was employed to bias and measure the gate and the drain current of OECTs. A delay of 100 ms was applied between measurements to ensure that the transistors had reached steady state. Customised software was designed in MATLAB to analyse and plot the exported data. In order to measure the frequency response of our devices, two NI-PXI-4071 digital multimeters and a customised LabVIEW program were used. All measurements were performed inside a Faraday cage to shield the transistors from any external sources of noise. Custom-built

electronics were used to control bias and convert the drain source current into voltage by utilising a transimpedance amplifier (10k gain), as shown in figure 2.2. The voltage signal was split into DC (frequency < 0.1 Hz) and AC (0.1 Hz < frequency < 5 kHz). The AC signal was amplified by an additional factor of 100 to assist with the noise evaluation. The voltage read out was done by a standard data acquisition system. All of the recordings were digitally filtered, using customised software in MATLAB, to remove 50 Hz noise and its harmonics as well as any external noise being added by the acquisition system. The data was also smoothed by using the smooth() function provided by MATLAB. Figures 2.3 a) and 2.3 b) illustrate the effects of filtering in the raw data. All calculations and graphs presented in this study were based on data that was treated in this manner, unless otherwise stated.

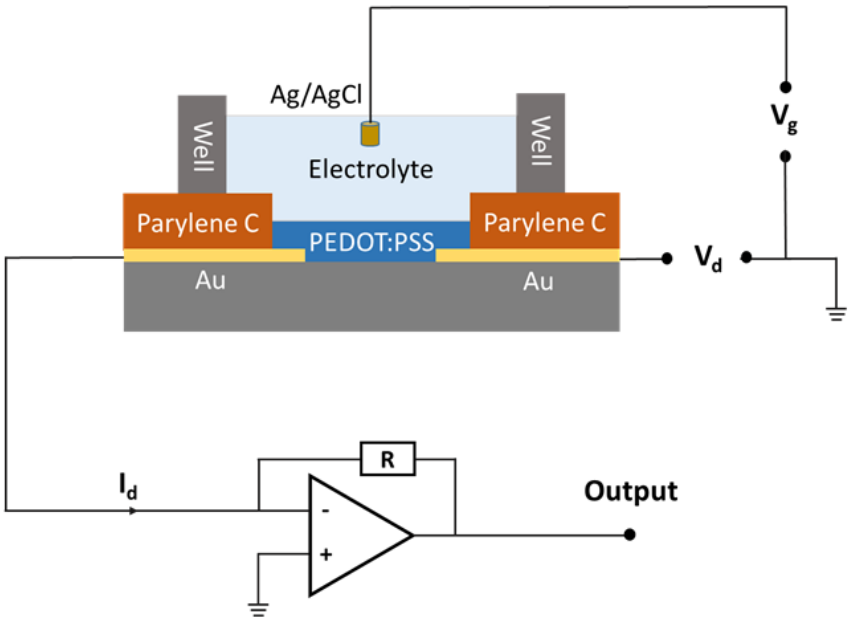

Figure 2.2 Schematic of an organic electrochemical transistor (OECT), highlighting the source and drain contacts as well as the gate electrode. A current to voltage amplifier was used to perform the noise measurements[115].

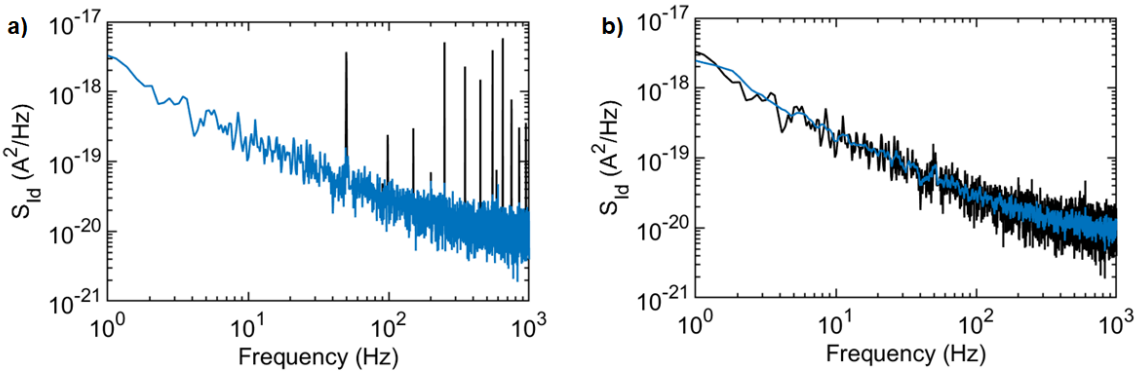

Figure 2.3 a) Removal of 50 Hz noise and its harmonics (indicated by the black lines) from the power spectral density (S_{Id}). b) Smoothing of S_{Id} vs. frequency.

2.3 Data treatment

All electrophysiology recordings were simultaneously acquired by a Keysight B2902A source measure unit, with a sampling frequency of 20 kHz. Both OECT and PEDOT:PSS electrode recordings were collected by the same equipment to minimise the effect of any noise added by the acquisition system and allow for fair comparisons between the two. Data were filtered digitally by employing a custom made MATLAB code. A Notch filter at 50 Hz was used to remove any noise added by power lines. We further filtered our data with a bandpass (1 – 300 Hz) filter to limit the frequency bandwidth of our experimental data, as we were mainly interested in recording LFPs. Time frequency analysis was performed in MATLAB in data that was filtered in both these manners.

2.4 *In vivo* protocol

All experimental procedures were performed in accordance with the UK Animals (Scientific Procedures) Act 1986. ~250 g Sprague Dawley rats (Charles River UK) were used for

this work. Animals anaesthetised using isoflurane (induction at 5% in O_2, maintenance at 2.5%). This was lowered to 1.25% isoflurane for electrophysiology recordings. Once anaesthetised animals were mounted on a stereotaxic frame, and their body temperature was monitored and maintained using a thermal blanket. Two stainless steel screws (M0.8 x 2mm, US Micro Screw) were inserted into the skull above the cerebellum to act as the grounded gate electrode for OECTs and the floating reference electrode for PEDOT:PSS electrodes.

A 6 mm by 4 mm square craniotomy was made (from approximately +2 mm anterio-posterior and +1 mm lateral, to -4 mm anterio-posterior and +5 mm lateral, relative to Bregma). The ECoG device was positioned over the limb somatosensory cortex (approximate Bregma coordinates -1 mm anterio-posterior and +3 mm lateral). All exposed tissue was kept moist by regular flushes using sterile saline. An ECoG device was then placed onto one of the two windows. The ECoG device was connected through its flexible flat cable to a custom made PCB board via a zero insertion force connector, and from there to one of the two channels of the Keysight B2902A source measure unit. After recording the device was moved to the other window, and recordings were repeated.

Chapter 3

Impact of contact overlap on transconductance and noise in organic electrochemical transistors[1]

3.1 Introduction

Since they were first developed by Wrighton in 1984[5], organic electrochemical transistors have attracted a great deal of attention and have found fertile ground in a variety of applications[4]. OECTs are organic transistors, consisting of two metal electrodes (source and drain), a semiconducting polymer film and a gate electrode submerged in an aqueous electrolyte. Different polymers have been employed to fabricate OECTs, with the most widely used being poly(3,4-ethylenedioxythiophene) polystyrene sulfonate (PEDOT:PSS), a p-type degenerately doped semiconductor. PEDOT:PSS has become popular within the bioelectronics community due to its stability, high conductivity and biocompatibility[85]. The unique architecture of OECTs allows them to convert ionic to electronic current by leveraging the mixed conductivity of their channel. This conversion is achieved by the injection of ions from the electrolyte and translates into a proportional modulation to the drain current[33]. This reversible exchange of ions between the electrolyte and the volume of the channel differentiates OECTs from field effect transistors (FETs) and makes them particularly suitable for biological sensing[28]. OECTs have been employed to

[1] This chapter is based closely on previously published work: **Anastasios G. Polyravas**, V. F. Curto, N. Schaefer, A. B. Calia, A. Guimera-Brunet, J. A. Garrido, and G. G. Malliaras, "Impact of contact overlap on transconductance and noise in organic electrochemical transistors". *Flex. Print. Electron. 4, 044003* (2019).

detect analytes[88], metabolites[89,116,117], ions[92], neurotransmitters[118] and DNA[93]; to interface with cells[36,119]; to measure neural activity[6,7]; and to replicate neuromorphic functions[120,121].

A figure of merit which is commonly used to characterise transistors is transconductance, defined as the first derivative of the drain current over the gate voltage, $g_m = \Delta I_d/\Delta V_g$. Transconductance quantifies the sensitivity of a transducer, as it directly relates a modulation in the gate voltage (input) to a modulation in the drain current (output). OECTs have been shown to exhibit the highest transconductance observed between electrolyte-gated transistors[27] given by the volumetric capacitance that describes conjugated polymers, such as PEDOT:PSS[122]. This leads to signal amplification and bestows OECTs with higher signal-to-noise ratio compared to surface electrodes[6] while providing them with a response time in the range of hundreds of μs[74]. A lot of recent work has focused on enhancing the performance of OECTs through the tuning of the device geometry[39,67] and the selection of the semiconducting material[66]. However, noise, which is a main limiting factor of the performance of OECTs has not been studied thoroughly.

Noise is described as a random disturbance in a signal and leads to a significant decrease in the quality of the information retrieved. The noise spectra can be divided into different types based on the source that generates it and the dependence on frequency, with the most important types of noise being thermal and flicker. Thermal noise originates from the thermal motion of charge carriers in a conductor and consists of a constant power spectral density that spreads across the whole frequency bandwidth. On the other hand, flicker noise exhibits a power spectrum that is inverse proportional to the frequency, rendering its contribution dominant in low frequencies and insignificant in high frequencies. A wide variety of reasons such as the bias voltage, the resistance and the structure of the organic device have been associated with the presence of flicker noise[97]. In contrast to thermal noise, flicker noise has been shown to significantly impact the performance of an electronic device and thus, it has been extensively studied in light emitting diodes[98], field effect transistors [99,112,123], thin film transistors[100] and graphene transistors[110]. While a lot of research has been performed on different types of transistors, there is only one study on OECTs[109].

In this work, we explore the noise characteristics of OECTs using PEDOT:PSS as the semiconducting material. We investigate how the bias conditions (drain and gate voltage) and the overlap between the gold contacts and the channel of the transistor affect the noise level of our devices. Our findings show how to tune the geometry and the bias conditions of OECTs to minimise noise and maximise signal-to-noise ratio.

3.2 Device performance

In this study, arrays consisting of 16 transistors with a channel length (L) of 50 μm and a width (W) of 50 μm were fabricated. The transistors were symmetrically grouped in 4 quadrants and exhibited different overlap between the source-drain contacts and the semiconducting channel area. A schematic of an OECT and the measuring system used is presented in Figure 3.1 a). Four different percentages of overlap were patterned (10%, 30%, 50% and 70%) corresponding to the length (L) of the PEDOT:PSS channel, leading to a total overlap of 5, 15, 25 and 35 μm on each side respectively. Figure 3.1 b) illustrates the resulting geometry, with the top image showing an OECT with 10% of overlap and the bottom image showing an OECT with 70% of overlap. The width and the length of the channel of every device was checked and was found to not deviate significantly (less than 2 μm) from the nominal values, with the overlap being in close proximity as well (within 1 μm). The total length (overlap between the PEDOT:PSS stripe and the source contact + overlap between the PEDOT:PSS stripe and the drain contact) in all OECTs was similar, allowing for comparisons between different devices.

Figure 3.1 c) shows the output characteristics of an OECT with W = 50 μm, L = 50 μm and d ~ 100 nm. The output characteristics were taken by applying a drain voltage (V_d) between 0 and - 0.6 V and a gate voltage (V_g) between 0 and 0.6 V, with a 50 mV step, and are typical for an electrolyte gated transistor operating in depletion mode[33]. The PEDOT:PSS film is fully doped in the absence of a gate voltage and hole current is flowing from source to drain. Upon the

application of a positive gate voltage cations from the electrolyte are injected into the channel, de-doping the film, leading to a significant reduction in the absolute value of the drain current (I_d). Figure 3.1 d) illustrates how the drain current and the transconductance vary as a function of the applied gate voltage for a constant V_d of - 0.6 V. From this transfer curve we obtain a maximum transconductance of about 1.7 mS at a V_g between - 0.1 to 0 V, in good agreement with transconductance values reported for OECTs with similar dimensions[27,39].

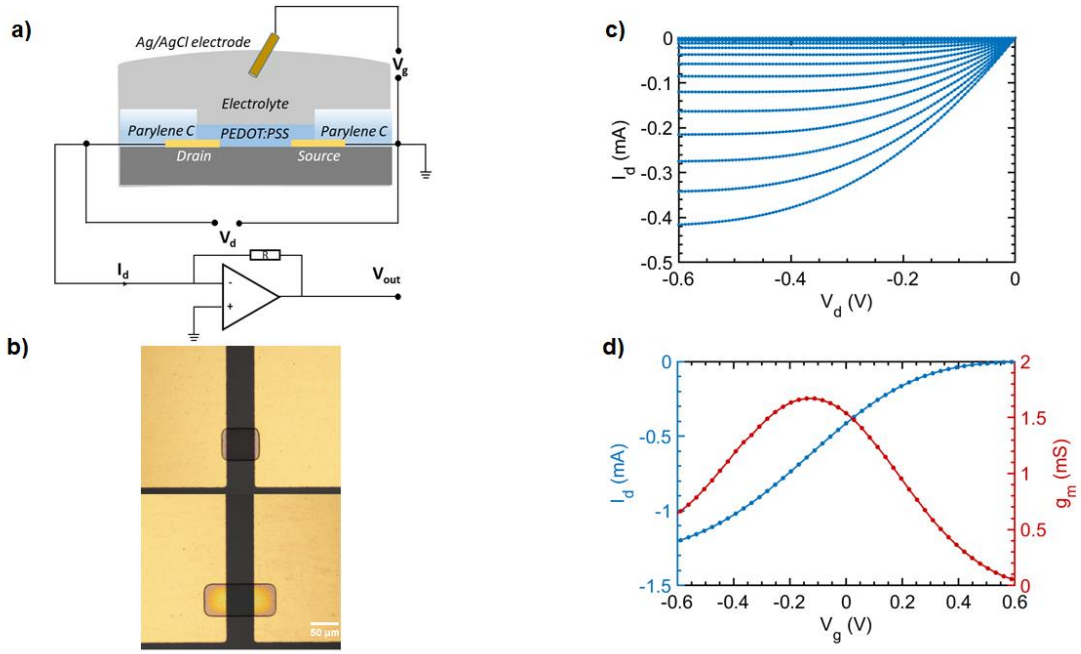

Figure 3.1 a) Schematic of an organic electrochemical transistor (OECT), highlighting the source and drain contacts as well as the gate electrode. A current to voltage amplifier was used to perform the noise measurements. b) Optical micrograph of an OECT with 10% (top) and 70% (bottom) overlap between the gold contacts and the PEDOT:PSS channel. c) Output curve of an OECT showing how the drain current (I_d) varies as a function of the drain voltage (V_d) for different gate voltage (V_g). Each curve is obtained by ranging V_g from 0 to 0.6 V with a 50 mV step (bottom to top). d) Transfer curve of an OECT biased at a constant V_d of - 0.6 V, indicating how the drain current and the transconductance (g_m) change as a function of the applied gate voltage.

3.3 Results and discussion

3.3.1 Noise behaviour

In order to understand the origin of noise in OECTs, we calculated the power spectral density of the drain current fluctuations (S_{Id}) for different gate and drain voltages while maintaining the same percentage of overlap. We found that S_{Id} depends on the bias conditions, as $S_{Id} \propto I_d^2$, whilst the spectra showed a 1/f characteristic in low frequencies. To minimise the effect of the current and be able to compare between different technologies, we normalised S_{Id} by dividing with I_d^2 and used this as a figure of merit. Interistingly enough, we observed that the normalised power spectral density, or relative noise, (S_{Id}/I_d^2) is independent of the applied V_d, for a fixed V_g (Figure 3.2). This suggests that drain voltage can be selected based on the needs of the application and the limitaions in power consumption, without affecting the noise level of an OECT.

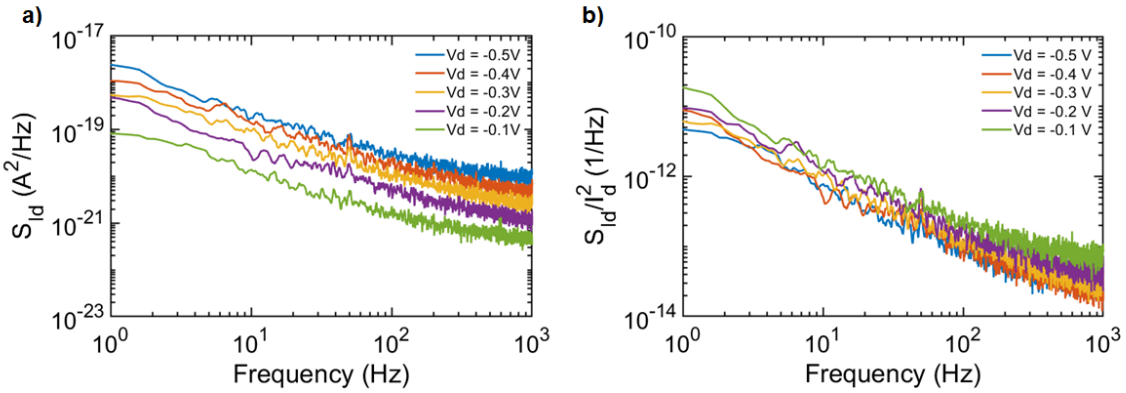

Figure 3.2 a) Power spectral density (S_{Id}) as a function of frequency for different bias voltages (V_d). Gate voltage was fixed at 0 V. b) Relative noise (S_{Id}/I_d^2) vs. frequency under the same bias conditions.

To further investigate the noise behaviour of our devices we plotted S_{Id}/I_d^2 as a function of frequency, shown in Figure 3.3 a). A constant V_d of - 0.5 V was applied to bias the device and the overlap was set to 30% (15 µm). The data shows that flicker (or 1/f) noise is the main contributor of noise in frequencies lower than 100 Hz with the spectra saturating above that; a regime where white noise becomes dominant. Figure 3.3 b) shows how relative noise varies as a function of the drain current with the blue line corresponding to the prediction of the α-noise model. In comparison, figure 3.3 c) demonstrates the dependence of relative noise on the ratio $(g_m/I_d)^2$, in agreement with the charge noise model. S_{Id} values were calculated at 10 Hz while I_d and g_m values were measured by changing the bias conditions. A better fit between our experimental data and the latter model was found. Our results agree with previous findings of Stoop et al., who verified this model for OECTs[109].

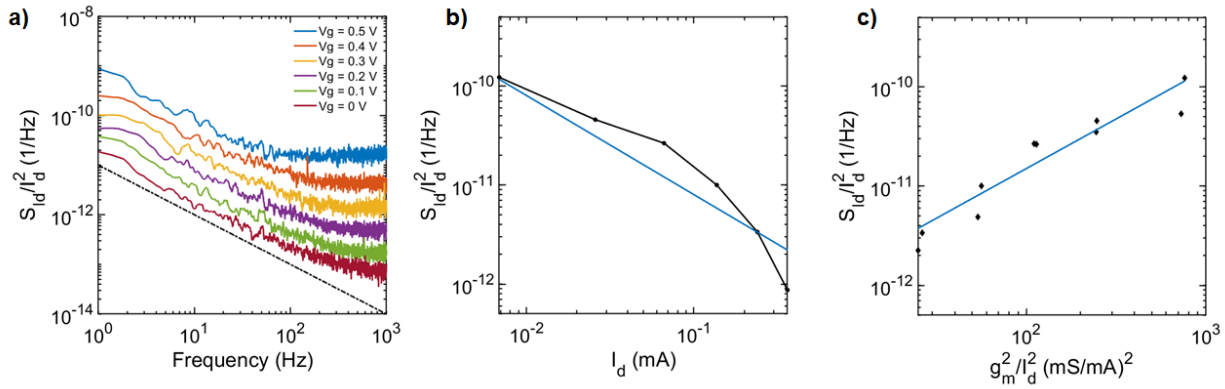

Figure 3.3 a) Relative noise (S_{Id}/I_d^2) vs. frequency. The black dashed line indicates a 1/f frequency dependence (flicker noise). b) Relative noise as a function of the drain current. The blue line corresponds to the prediction of Hooge's law. c) Relative noise vs. $(g_m/I_d)^2$. A better fit between our experimental data and the proposed charge noise model is observed.

3.3.2 Contact overlap

In order to investigate how geometry affects the performance of OECTs, we examined samples with 4 different percentages of overlap between the channel and the gold contacts. Transistors with different overlap had the same channel area (W, L) but a different percentage of surface area was covered by PEDOT:PSS and was exposed to the electrolyte solution (Figure 3. 1 b). We explored how g_m changes as a function of V_g for transistors with 10%, 30%, 50% and 70% of overlap. Figure 3.4 a) highlights our findings for four representative devices. All four OECTs were fabricated on the same glass slide and were equally spaced from the centre, to ensure that the thickness of PEDOT:PSS was similar for all of them. As can be seen from figure 3.4 a), g_m appears to not vary systematically as a function of the contact overlap. As expected an increase in the overlap area does not modify the active length of the channel and hence, the transconductance of OECTs. Our results demonstrate that a good ohmic contact is achieved at both source and drain contacts, independently of the overlap area.

To further explore the effect of overlap on the performance of OECTs we studied the frequency response of our devices. OECTs were biased with a constant V_d while a series of sine waves (amplitude of 50 mV, frequency range from 1 Hz to 20 kHz) was used at the gate electrode. Figure 3.4 b) shows how normalised transconductance ($g_m/g_{m,max}$) changes as a function of frequency for four devices with different percentage of overlap. We found that the cut-off frequency, which corresponds to $g_{m,fc} = \frac{1}{\sqrt{2}} * g_{m,max}$, increases as the overlap decreases. Our findings come in good agreement with previous work performed in thin film transistors[124]. To quantify this shift in f_c we considered that an OECT consists of two circuits, an electronic and an ionic one[33]. A recent study has shown that the cut-off frequency of PEDOT:PSS square surface electrodes is inverse proportional to $A^{\frac{1}{2}}$, where A stands for the total surface area of the electrodes[125]. Based on that study we employed a simple RC circuit to model OECTs[67] and substituted L with L' (given by adding the total length of the overlap into the active length (L) of the transistor channel) to describe the length of the PEDOT:PSS stripe. We derived that $f_c \sim \frac{1}{R_s C}$, where $R_s \sim \frac{1}{2(L'+W)}$ [126] and $C \sim (L'Wd)$ [67]. A more thorough analysis of the derived equations is

presented in the section below. A difference of ~300 Hz in the f_c was observed between OECTs with the 70% and 10% of overlap.

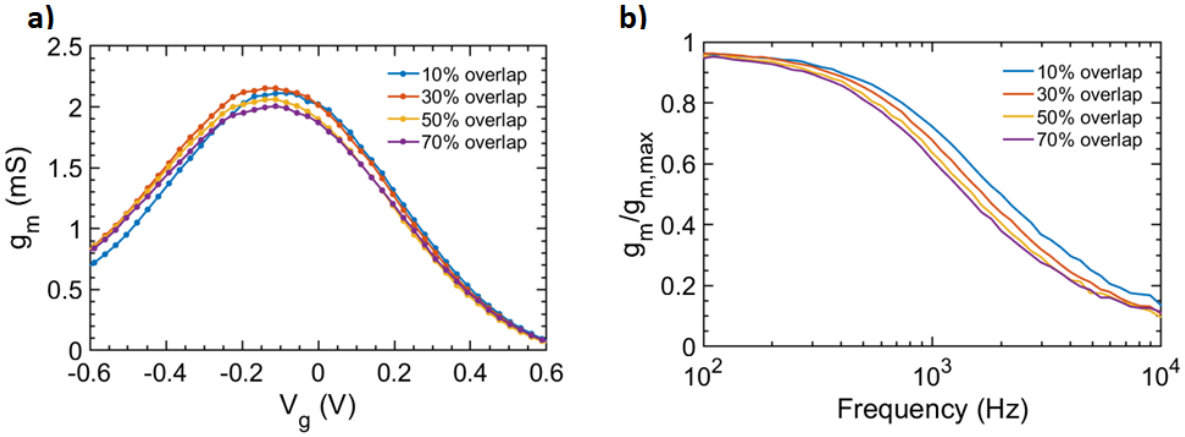

Figure 3.4 a) Variation of the transconductance as a function of the applied gate voltage for four transistors of different percentage of overlap. b) Normalised transconductance ($g_m/g_{m,max}$) vs. frequency. OECTs with a lower percentage of overlap show a higher cut-off frequency.

Finally, we examined how overlap correlates with noise in OECTs. Figure 3.5 shows how S_{Id}/I_d^2 varies as a function of V_g for four transistors of different overlap, at a fixed frequency of 10 Hz. The value of 10 Hz was selected as it corresponds to alpha waves in encephalography[127] and also allows comparisons between different technologies. As can be seen, relative noise increased under the application of a higher gate voltage for all the reported devices. To better understand this trend we calculated the ratio g_m/I_d for different V_g and found that the absolute value of g_m/I_d increased under the application of a higher V_g; in agreement with the prediction of the charge noise model. In contrast to f_c, no significant dependency between noise and overlap was observed. This is consistent with the fact that device performance, as seen by the steady state transconductance, does not vary with contact overlap. It demonstrates that noise is determined by the length of the transistor channel instead of the length of the PEDOT:PSS film.

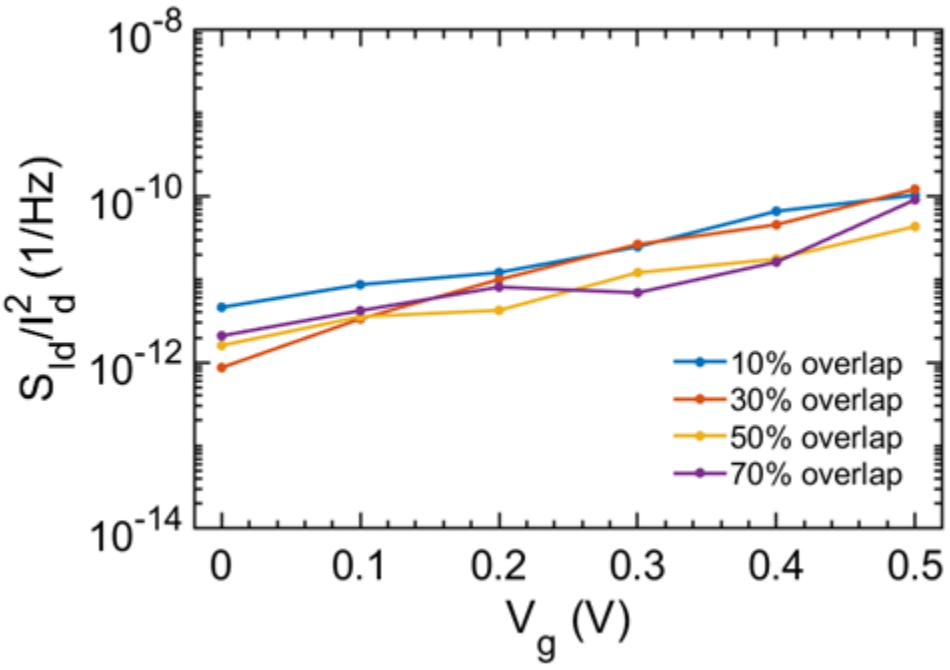

Figure 3.5 Relative noise vs. gate voltage illustrating that the noise level of an OECT is independent of the overlap.

3.3.3 Calculation of the cut-off frequency

The measured values of the cut-off frequency, where $\mathbf{g_{m,fc}} = \frac{\mathbf{1}}{\sqrt{\mathbf{2}}} * \mathbf{g_{m,max}}$, are shown in Table 2. The cut-off frequency is given by:

$$\mathbf{f_c} \sim \frac{\mathbf{1}}{\mathbf{RC}}, \qquad \text{(S1)}$$

where:

$$\mathbf{R} \sim \frac{\mathbf{1}}{\mathbf{2(L'+W)}}$$ [126] (S2)

and

$$\mathbf{C} \sim (\mathbf{L'Wd}),$$ [67] (S3)

where L' is the length of the PEDOT:PSS stripe[125].

The shift in f_c can be calculated by

$$\frac{\mathbf{f_{c,n+1}}}{\mathbf{f_{c,n}}} = \frac{(\mathbf{L'_{n+1}+W})}{(\mathbf{L'_n+W})} * \frac{\mathbf{L'_n}}{\mathbf{L'_{n+1}}}, \text{ (eq. 1)}$$

where $f_{c,n+1}$ is the estimated "shifted" cut-off frequency and $f_{c,n}$ is the known/starting cut-off frequency of the device under test. To check the validity of eq. 1, we measured the cut-off frequencies of our transistors by numerical interpolation and compared these values to the ones calculated by eq. 1. Eq. 1 seems to provide accurate estimations of f_c with slight deviations that can be justified by the rounding of the channel overlap edges, caused during the fabrication process. A difference of 287 Hz in the f_c was observed between OECTs with 70% and 10% of overlap (see Table 2). The values of the cut-off frequencies can alternatively be calculated by applying an exponential fit to the temporal response of the drain current to a positive gate voltage[74]. However, eq. 1 provides a quick and effective way to correlate the cut-off frequency of an OECT with the overlap between the channel and the gold contacts. Assuming agreement for 10% contact overlap, the calculated values for contact overlap are shown in Table 2. The "f_c Measured" column corresponds to the frequency values measured by numerical interpolation and the "f_c Calculated" column corresponds to the frequency values calculated by applying eq. 1.

% contact overlap	W (µm)	L' (µm)	f_c(Hz), Measured	$\frac{f_{c,n+1}}{f_{c,n}}$	f_c(Hz), Calculated
10%	50	60	1052	(-)	(1052)
30%	50	80	905	0.886	932
50%	50	100	811	0.923	835
70%	50	120	757	0.944	765

Table 2 Experimental and calculated values of the cut-off frequency for OECTs with different contact overlaps.

3.3.4 Discussion

The analysis of the noise characteristics of OECTs revealed that the power spectral density can be divided into two regimes. The first one consists of frequencies lower than 100 Hz and is dominated by flicker noise whereas the second one starts from frequencies higher than 100 Hz and exhibits a constant white noise spectra, typical of thermal noise. In this study, we emphasised on understanding the origin of flicker noise and provide ways of minimising the relative noise of OECTs. Minimising the noise level of an OECT can significantly enhance its performance and provide more detailed information when used as a recording device. This is particularly interesting when exploring electrophysiology signals such as alpha, delta, theta, beta and low gamma activity, which can be found in a frequency bandwidth ranging from 1 to 70 Hz.

In the analysis we performed, we investigated how the bias conditions (both gate and drain voltage) can affect the noise level of our OECTs. Our results show that the noise level increases with gate voltage. However, in contrast to S_{Id}, which was found to depend on the applied voltage V_d, relative noise appeared to be independent of V_d. Based on these findings, we suggest modifying the geometry of OECTs in order to exhibit maximum transconductance at zero

gate voltage while choosing a drain voltage that provides sufficient current and exhibits minimum power consumption, with regards to the respective application.

We also aimed to answer the question of whether the overlap between the channel and the metal electrodes can affect the performance of OECTs, with the greater aim of setting new design rules. Our findings show that overlap can be used as a factor to tune the frequency response of an OECT without significantly affecting the transconductance and the noise characteristics of the device. Understanding the behaviour of the frequency response of a transistor is of paramount importance as it sets a physical limitation in the bandwidth of the recorded signals. In order to efficiently record a signal of good quality, we need to ensure that the majority of the information is found in a range that does not exceed the cut-off frequency. Having mentioned this, we propose minimising the length of the organic semiconductor stripe to achieve a higher frequency bandwidth.

By fitting our data with the existing noise models, we found that a better fit was observed when applying the charge noise model, according to which the measured noise in the drain current originates from fluctuations in the hole density inside the channel. Noise can therefore be referred to voltage fluctuations at the gate according to $S_{Id} = S_{Vg} * g_m^2$, where S_{Vg} is the gate-referred noise[111,128]. Using this equation, we extracted an $S_{Vg} = 12.7 * 10^{-14}$ V^2Hz^{-1}. This value, compares favourably to previous measurements in PEDOT:PSS OECTs[109] and electrolyte-gated graphene transistors[110].

For sensor applications, $\sqrt{S_{Vg}}$ is an important figure of merit as it can used to evaluate the measuring capabilities of a device[128]. The signal-to-noise ratio (SNR) can be determined as the change in the potential of an ion sensitive membrane to the gate voltage noise ($SNR \propto \frac{1}{\sqrt{S_{Vg}}}$), where the smallest detectable voltage is given by $\Delta V = \sqrt{S_{Vg}}$ [109]. The extracted value for S_{Vg} translates into a $3.5669 * 10^{-7}$ ΔV. Comparing our devices with the ones previously reported[109], we found a 4.4 improvement in the SNR. Calculations in the S_{Vg} and SNR values were performed by rescaling the dimensions of the channel area in our devices, assuming that $S_{Vg} \propto \frac{1}{WL}$ [109].

Similarly to S_{Vg}, another figure of merit that is widely used to compare the recording capabilities of a device is V_{rms}. In contrast to S_{Vg}, which referes to a specific frequency (10 Hz in

our case), V_{rms} is calculated by applying a bandpass filter between a desired frequency bandwidth and thus, is calculated by:

$$V_{rms} = \sqrt{\frac{\int_{f1\ Hz}^{f2\ Hz} S_{I_d} \cdot df}{{g_m}^2}}$$

In a frequency range varying from 1 to 100 Hz, we calculated a $V_{rms} = 3.4$ μV. This value is more than adequate for enabling electrophysiology recordings[20].

3.4 Conclusion

In this work, we investigated how different parameters such as the contact overlap and the bias conditions can affect the noise characteristics of an OECT. We identified flicker noise as the main source of noise in low frequencies (<100 Hz) and consistent with the charge noise model. We found that relative noise is affected by the voltage applied in the gate electrode but is independent of the voltage applied between source and drain. By studying transistors with different overlap, we presented a way to change the frequency response of an OECT without changing the noise level and the transconductance. Our results shed light in some new design rules that can be utilised to tune the performance of OECTs and improve their recording capabilities.

Chapter 4

Effect of channel thickness on noise in organic electrochemical transistors[2]

4.1 Introduction

Organic electrochemical transistors have been attracting a great deal of attention due to advantages they bring, such as simple structure and high performance[4]. Their principle of operation involves changes in the conductivity of a semiconducting film induced by ions injected/extracted from an electrolyte[33]. This process is regulated by a gate electrode, which is immersed in the electrolyte and results to changes in the doping state of the semiconductor. These changes in the doping state of the polymer film are translated into different values of drain current. The latter is induced by a voltage applied between source and drain electrodes that make contact with the semiconducting film. The simple architecture of OECTs lends itself to fabrication by traditional photolithography[129] but also by low-cost printing techniques[130], onto a variety of

[2] This chapter is based closely on previously published work: **Anastasios G. Polyravas**, N. Schaefer, V. F. Curto, A. B. Calia, A. Guimera-Brunet, J. A. Garrido, and G. G. Malliaras, "Effect of channel thickness on noise in organic electrochemical transistors". Appl. Phys. Lett. 117, 073302 (2020).

substrates that include plastic[27], paper[131] and textile fibres[132]. OECTs have been used as transducers[133,134], in electrophysiology[6,7,90,135,136], biosensing[137–140] and *in vitro* systems[36,141].

In the majority of these applications, OECTs are used as transducers that regulate a voltage change at the gate ∂V_g to a current modulation in the drain ∂I_d [4]. This process is described by transconductance $g_m=\partial I_d/\partial V_g$ and is directly linked to the ability of OECTs to amplify recorded signals[39]. Consequently, a lot of emphasis has been placed on understanding how to improve transconductance by tuning device geometry[39,67], engineering the material design[142] and developing new device architectures[143]. OECTs using PEDOT:PSS, a commercially available *p*-type semiconducting material, show transconductance in the range of mS, outperforming transistors from both traditional and emerging semiconductors[27]. In contrast to field-effect transistors, where changes in conductivity happen in a thin channel formed close to the gate insulator, OECTs architecture allows the modulation of the entire volume of the semiconducting film. As a result, transconductance scales with channel thickness[67], making this an identifying characteristic of OECTs[66]. By utilising this volume dependence of transconductance, one can reach arbitrarily high values of g_m by simply increasing the channel thickness; OECTs with a transconductance of 1 S have been demonstrated[144].

Having highlighted the importance of channel thickness on signal amplification, a question that rises is how could this identifying parameter correlate with the noise being generated in the channel of an OECT. Stoop et al. and his colleagues were the first to investigate noise in OECTs[109]. Their study assisted in quantifying parameters that relate to signal-to-noise ratio (SNR) and limit of detection (LOD) while also showing that PEDOT:PSS OECTs exhibit a noise level that is comparable to graphene transistors, and only slightly higher than transistors based on carbon nanotubes and silicon nanowires. Moreover, their results suggested that large area channels maximise SNR. In the previous section, we investigated the impact of contact overlap and showed that it does not modify the noise characteristics of PEDOT:PSS OECTs[115]. Here, we explore the scaling of noise in OECTs as a function of the channel thickness. We demonstrate that metrics for SNR and LOD improve with channel thickness and address the origin of this behaviour. Our findings provide guidelines for optimising the performance of OECT-based transducers,

combining previous knowledge on the steady state behaviour of OECTs with the noise profiles arising from this work.

4.2 Results and discussion

4.2.1 Device architecture

OECTs developed for this study have the typical planar structure shown in Figure 3.1 a). Briefly, the gold contacts were photolithographically patterned onto a glass substrate, resulting in a 50 x 50 μm^2 channel. The semiconducting film was formed by spin coating a dispersion of PEDOT:PSS at multiple cycles to create channels with multiple layers of the polymer film. This resulted in OECTs with different thickness, i.e. 140 ± 14, 315 ± 74 and 1330 ± 75 nm (N = 6 devices per thickness); with the error bars corresponding to the standard deviation. To ensure good adhesion and uniformity, a soft pre-bake (one minute at 110^oC) was employed before the deposition of each subsequent layer of PEDOT:PSS. A 2 µm thick layer of parylene C (PaC) was used to insulate the gold contacts of each transistor, leaving only the channel area exposed to an aqueous electrolyte. The conductivity of the semiconducting film was regulated by a Ag/AgCl electrode, submerged into the electrolyte solution.

Before proceeding with the noise analysis, we examined the steady state characteristics of our devices. Figure 4.1 shows how I_d scales as a function of the applied gate voltage for a V_d varying from 0 to - 0.5 V. As can be seen, the saturation voltage as well as the amount of current that is induced between the drain and source contacts depends on the channel thickness. The transconductance of three representative devices is also presented in Figure 4.2. Transconductance was measured by grounding the source contact and applying a voltage of - 0.5 V at the drain, with V_g varying from - 0.6 to 0.6 V. Despite the increase observed in the maximum g_m value for OECTs with greater thickness, transconductance was not found to scale proportionally to the channel thickness, as expected from Bernards model[33]. Consistent with a

previous study[67], we found that the main reason for this deviation is the voltage drop caused by the resistance of the gold interconnects (described in the section below).

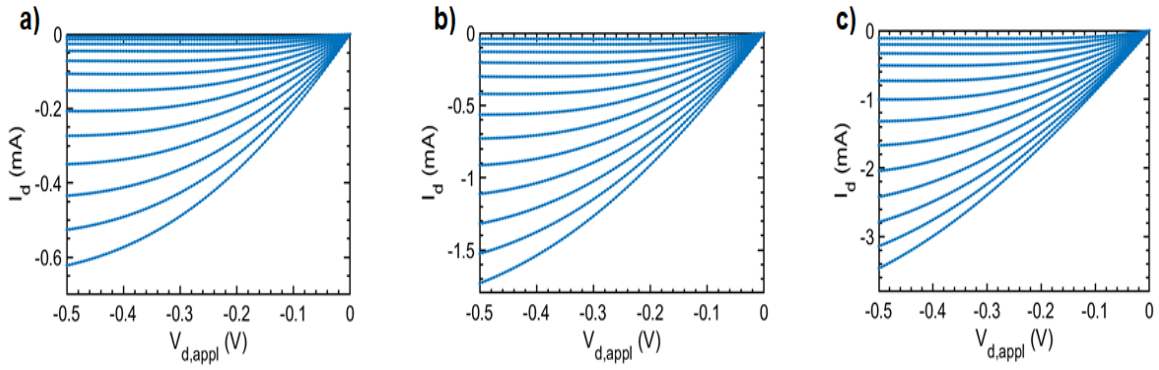

Figure 4.1 Output curves of three representative OECTs with a thickness of ~140 (a), 315 (b) and 1330 (c) nm. Each line corresponds to a different gate voltage ranging from 0 to 0.6 V with a 50 mV step.

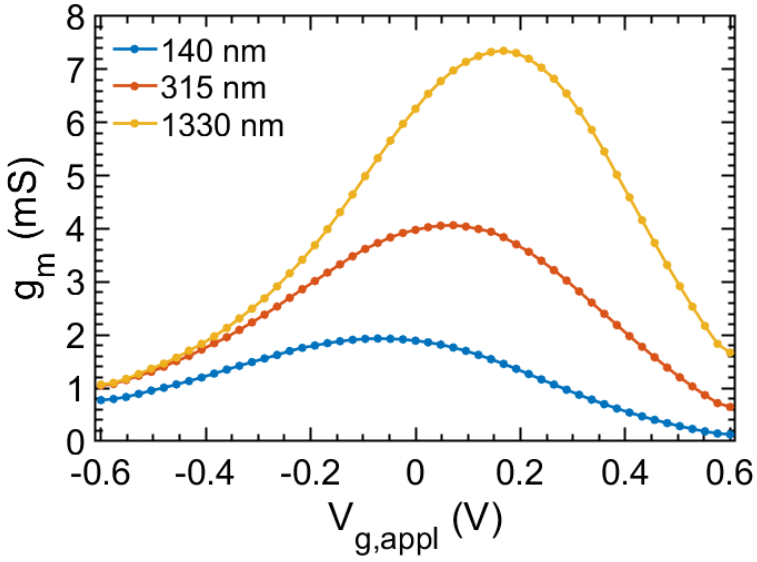

Figure 4.2 Transconductance vs. gate voltage for three OECTs with different thickness. The curves correspond to the measured values before applying any correction for resistive loss. V_d was fixed at – 0.5 V.

4.2.2 Correction for resistive loss

Despite knowing that resistive loss is present in every electronic system, we decided to apply a simple model to account for the voltage drop happening at the source and drain contacts. We used this model to correct for the effective voltage applied between the gate, source and drain terminals but most importantly to correct for the peak g_m, as this is an important figure of merit when examining OECTs with varying channel thickness.

If R is the total resistance of the interconnects, the circuit between the source and drain terminals can be modelled as three resistors in series: A resistor $\frac{1}{2}R$ representing the path from the source terminal to the source electrode, a resistor that corresponds to the channel R_{ch}, and a resistor $\frac{1}{2}R$ representing the path from the drain electrode to source. Placing the ground at the source terminal and applying $V_{g,appl}$ at the gate terminal and $V_{d,appl}$ at the drain terminal, the true values of V_g and V_d are:

$$V_g = V_{g,appl} - \frac{1}{2} I_d R$$

$$V_d = V_{d,appl} - I_d R$$

The interconnects had a length varying from 1.3 mm to 3 mm and a width that tapered from 300 µm down to 100 µm. The mean value of R was measured by short-circuiting the channels with a Au film and were calculated to be 92 ± 18 Ω (N = 12 devices). The values of the transconductance were also corrected for the true value of V_d based on:

$$g_m = \frac{W}{L} d\mu C^* V_d$$

The corrections are summarised in Table 3 below.

Channel thickness/correction	140 nm	315 nm	1330 nm
$\mathbf{V_g}$	+30 mV	+80 mV	+170 mV
$\mathbf{V_d}$	-440 mV	-340 mV	-160 mV
$\mathbf{g_m}$	×1.11	×1.46	×3.12

Table 3 Corrections applied to account for resistive loss at the Au interconnects.

Figure 4.3 shows the variation of transconductance as a function of the applied gate voltage for three OECTs, after performing the resistive loss correction. The maximum transconductance for the OECT with the thickest PEDOT:PSS channel was 22.8 mS, a value that is 10.5 and 3.8 times higher compared to the OECTs with a thickness of ~140 nm and ~315 nm, respectively. These results are in better agreement with Bernards model[33]. A shift in the gate voltage at which peak transconductance is reached was also observed, consistent with previous reports that studied the dependence of transconductance as a function of the channel geometry (width, length, thickness)[39].

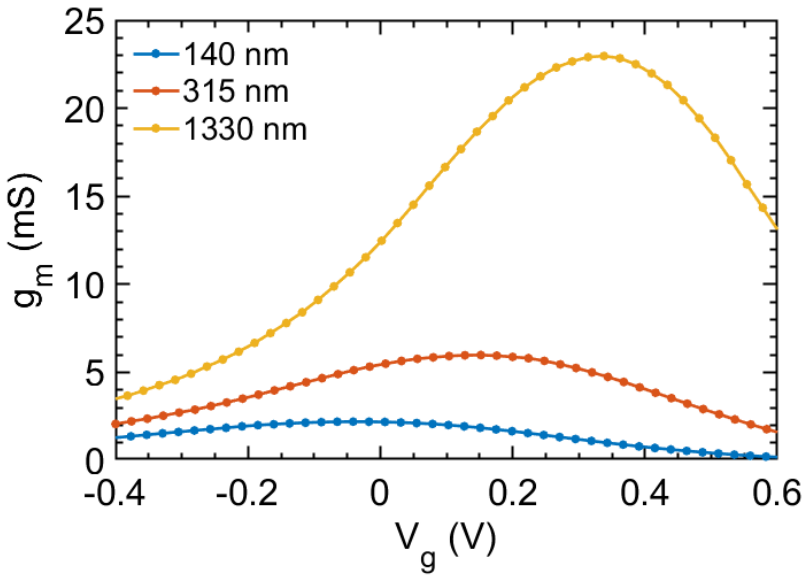

Figure 4.3 Transconductance vs. gate voltage for three OECTs with different thickness. Both g_m and V_g were corrected for resistive loss at the interconnects.

4.2.3 Frequency response

An increase in channel thickness is known to be accompanied by a decrease in the cut-off frequency[67], as the response time of OECTs increases drastically. This increase is directly linked to the volumetric behaviour of an OECT channel; thicker films exhibit a greater capacitance allowing the exchange of more ions within the organic polymer and thus slowing the operation of the device. This is shown in Figure 4.4, where the normalised transconductance $g_{m,norm}$ is plotted as a function of frequency f. OECTs were biased by applying - 0.5 V at the drain terminal with a series of sine waves with a frequency ranging from 1 Hz to 20 kHz and an amplitude of 50 mV being applied at the gate terminal. Transconductance was calculated by measuring the change ΔI_d in the drain current as a function of the applied sine wave in the gate terminal. Figure 4.4 is plotted by numerical interpolation of the acquired measured points. A 7.2 times decrease (998 Hz compared to 138 Hz) in the cut-off frequency was observed when the channel thickness was varied from ~140 nm to ~1330 nm.

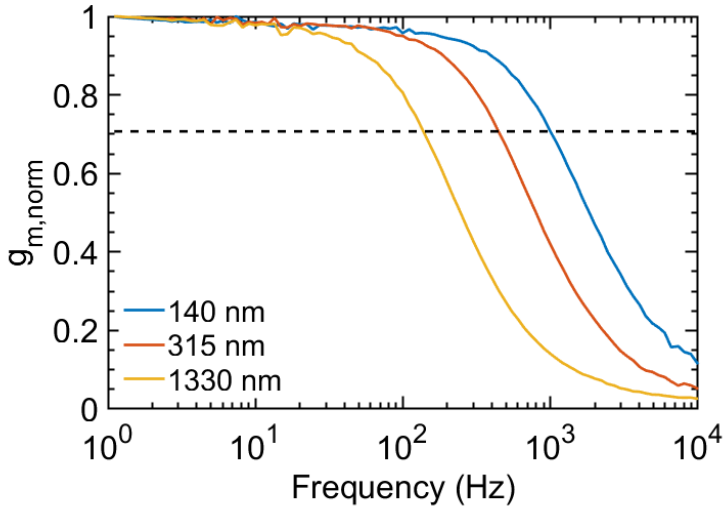

Figure 4.4 Normalised transconductance vs. frequency with the dashed line corresponding to the cut-off frequency (-3dB).

Two different models were examined to provide a prediction for the cut-off frequency. The first one is a simplified model that consists of a resistor R_s in series with a capacitor C (RC circuit) whereas the second one includes an extra resistor R_p in parallel with the capacitor C (RRC circuit). These models have been previously applied to describe electrode operation and have also found applicability in OECT operation[67]. Fit parameters and predictions of the two models are shown in Table 4. As expected, R_p decreases with channel thickness (due to an increase in the total volume of the polymer film), but remains three orders of magnitude higher than R_s, meaning that the RC circuit is accurate enough. The model does a reasonable job at predicting the cut-off frequency. Values in Table 4 were calculated based on a previous study[67].

Channel thickness	140 nm	315 nm	1330 nm
$\mathbf{R_s}$	10 kΩ	10 kΩ	10 kΩ
$\mathbf{R_p}$	20 MΩ	10 MΩ	6 MΩ
C	15 nF	30 nF	150 nF
$\mathbf{f_{c,RC}}$	1061 Hz	531 Hz	106 Hz
$\mathbf{f_{c,RRC}}$	1061 Hz	531 Hz	106 Hz
$\mathbf{f_{c,meas}}$	998 Hz	444 Hz	138 Hz

Table 4 Fit parameters and predictions for the two models frequency response models.

4.2.4 Noise analysis

Having explored the effect of different channel thickness on the device performance, we proceeded with the analysis of the noise characteristics of OECTs. Figure 4.5 a) shows how the power spectral density of the drain current S_{Id} of an OECT with ~140 nm channel thickness varies

as a function of frequency; the black dashed line is a guide for the eye, indicating a 1/f slope. As mentioned, this is a typical characteristic of flicker noise and was observed in frequencies lower than 100 Hz, in agreement with previous studies in thin film transistors[110,123], including OECTs[109,115]. To be consistent with our previous findings, we also investigated how relative noise S_{Id}/I_d^2 varies as a function of frequency and we observed a similar trend. Considering that relative noise can be used as a figure-of-merit to compare the noise level across different device architectures and bias conditions[145,146], we applied it as a normalisation to compare OECTs with different channel thickness. Figure 4.5 b) illustrates how relative noise scales with gate voltage for OECTs with three different thicknesses. Calculations were performed at 10 Hz. Each point in the graph represents the mean value measured from six OECTs with the same nominal channel thickness, with the error bars corresponding to the standard deviation. As seen from Figure 4.5 b), relative noise decreases non-linearly with channel thickness.

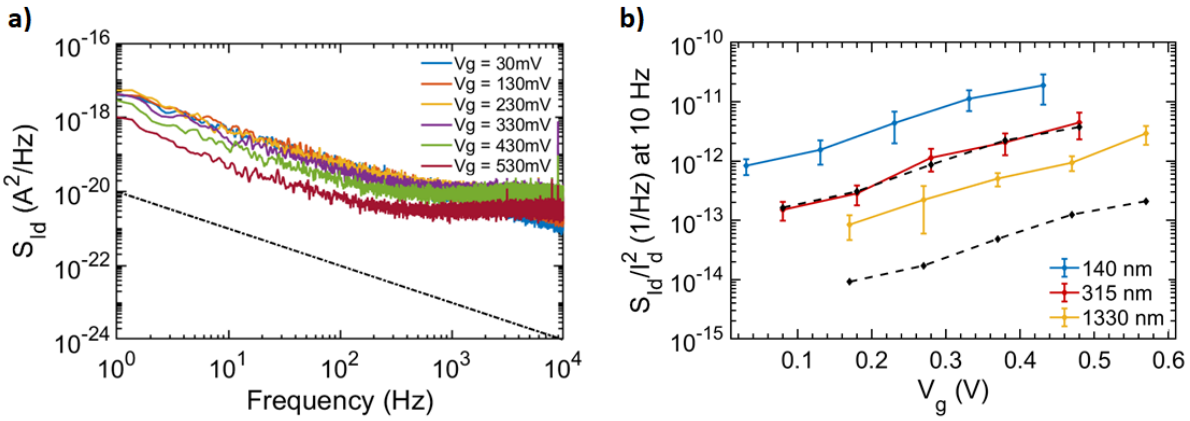

Figure 4.5 a) Power spectral density S_{Id} vs. frequency for an OECT with ~140 nm channel thickness. The dashed line has a slope of 1/f, indicating that flicker noise is the dominant contributor of noise at low frequencies. b) Normalised power spectral density S_{Id}/I_d^2 vs. gate voltage for OECTs with different thickness. Each point corresponds to the mean value (N = 6 transistors), with the error bars indicating the standard deviation. The solid lines are guides to the eye. V_g was corrected for resistive loss at interconnects. The dashed lines correspond to the scaling predicted by the charge noise model.

The noise behaviour of electrolyte-gated transistors[110,112,128], including OECTs[109], is usually described by the charge noise model. This model assumes that flicker noise originates from fluctuations in the number of charge carriers in the channel of the transistor[111]. Based on this assumption, the normalised power spectral density S_{Id}/I_d^2 is expected to be proportional to the ratio g_m^2/I_d^2, a trend that seems to hold in our devices (Figure 4.6). Moreover, in the charge noise model S_{Vg} is inversely proportional to the square of the gate capacitance[109,145]. By combining this with the capacitance dependence of OECTs with channel thickness, we extract that S_{Id}/I_d^2 is expected to scale proportionally to $1/d^2$. The dashed lines in Figure 4.5 b) reflect the theoretical scaling of relative noise for OECTs with a channel thickness of ~315 nm and ~1330 nm. The thickness of the thinnest OECT was used as a starting point to assist with these calculations. While a good agreement is observed for transistors with a ~315 nm thick channel, the relative noise predicted for transistors with a ~1330 nm thick channel is about 10 times lower compared to the measured values. This discrepancy is discussed more thoroughly in the Discussion section below.

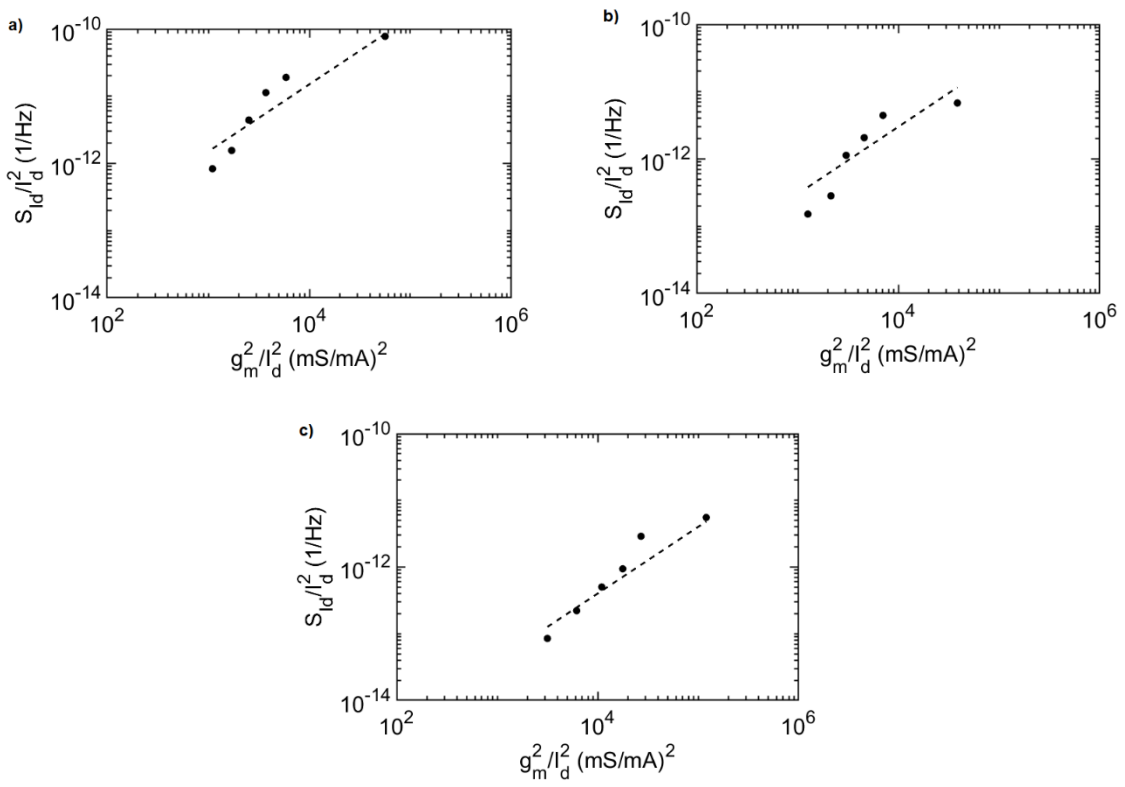

Figure 4.6 Normalised power spectral density of the drain current vs. $(g_m/I_d)^2$ for OECTs with a thickness of 140 nm (a), 315 nm (b) and 1330 nm (c), respectively. Each point corresponds to the mean value calculated from N = 6 transistors. The dashed line is a fit to the charge noise model. Transconductance values were corrected for resistive loss at the gold interconnects.

In addition to relative noise, parameters that relate to SNR and LOD are also used to characterise and compare transducer technologies. One of these parameters is the square root of the gate referred voltage noise $S_{Vg}^{1/2}$, obtained by dividing $S_{Id}^{1/2}$ by g_m. $S_{Vg}^{1/2}$ refers to a certain frequency (10 Hz in our case) and as such, it is used as a way to estimate SNR when the transistor is operating as a voltage sensor (the lower the $S_{Vg}^{1/2}$, the higher the SNR)[109,123]. Figure 4.7 a) shows how $S_{Vg}^{1/2}$ varies as a function of V_g, for OECTs with different channel thickness. The dashed lines reflect the theoretical values of $S_{Vg}^{1/2}$ for OECTs with a channel thickness of ~315 nm and ~1330 nm, respectively. Similarly to relative noise, a good agreement is observed for OECTs with a ~315 nm thick channel. However, a lower value is predicted for OECTs with a ~1330 nm thick channel.

It should be noted that despite the deviation from the theoretical values, the 50 nV/Hz$^{1/2}$ obtained from the OECT with ~1330 nm channel compares favourably to values reported in other thin film transistor technologies[110,128,147].

Another important metric for transistors is V_{rms}. V_{rms} is obtained by integrating S_{Id} over a frequency window of interest and extracting the square root of the integrated S_{Id} divided by transconductance[112,148]. As such, it quantifies the LOD, or the minimum voltage that can be detected by the transistor. In Figure 4.7 b) the V_{rms} values of eighteen OECTs with different thickness are plotted as a function of transconductance. Since relative noise flattens in frequencies higher than 100 Hz (Figure 4.5 a)), we chose the frequency window to correspond to 1 – 100 Hz and calculated V_{rms} with V_g = 0 V. For comparison reasons, we also calculated the V_{rms} values at a V_g corresponding to maximum transconductance (Figure 4.8). We found that V_{rms} decreases at higher transconductance (and hence channel thickness), realising its lowest value of approximately 0.4 μV for OECTs with the thickest channels. Table 5 shows the calculated V_{rms} values in different frequency bandwidths. Based on our results, OECTs compare favourably to reported values of transistors[148] and electrodes[149] from other materials. It should be noted that the thermal noise added by the Au interconnects was 12.28 nV in the 1-100 Hz range and hence, it was considered negligible.

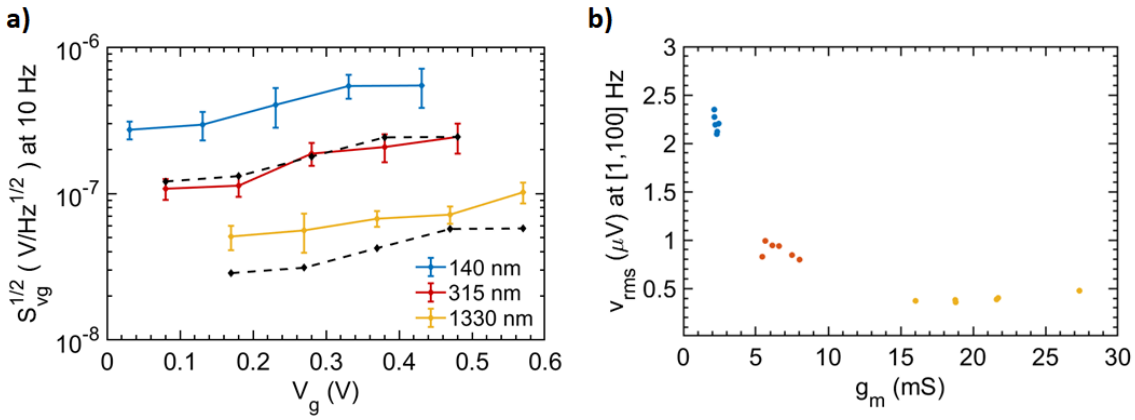

Figure 4.7 a) Root square gate voltage noise vs. V_g for OECTs with different thickness. Each point corresponds to the mean value obtained from N = 6 transistors, with the error bars indicating the standard

deviation. The solid lines are guides to the eye. V_g was corrected for resistive loss at interconnects. The dashed lines correspond to the scaling predicted by the charge noise model. b) Root mean square of the voltage fluctuations V_{rms} in the 1 Hz to 100 Hz bandwidth vs. transconductance. V_{rms} values were calculated for 0 V applied at the gate terminal.

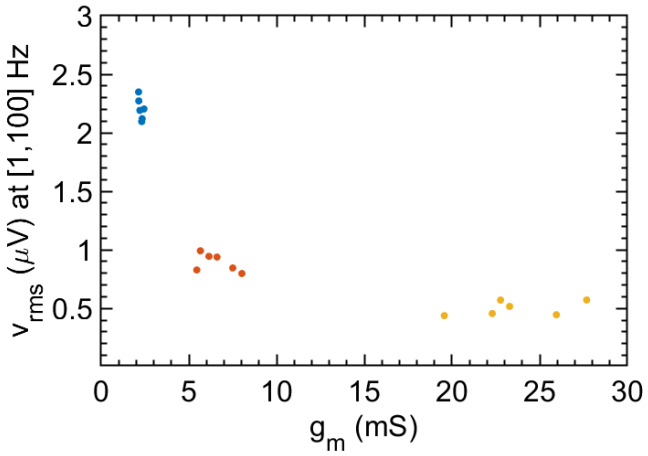

Figure 4.8 Root mean square of the voltage fluctuations in the 1 Hz to 100 Hz bandwidth vs. transconductance. V_{rms} values were calculated at the voltage at which the maximum transconductance was observed.

Channel thickness	V_{rms} at different frequency ranges			
	(1 - 30) Hz	(1 – 100) Hz	(1 – 1000) Hz	(1 – 5000) Hz
140 nm	1.88 µV	2.20 µV	2.83 µV	3.40 µV
315 nm	0.77 µV	0.89 µV	1.16 µV	1.39 µV
1330 nm	0.34 µV	0.40 µV	0.51 µV	0.60 µV

Table 5 V_{rms} of OECTs at varying frequency bandwidths.

4.3.1 Discussion

The volumetric capacitance that organic materials such as PEDOT:PSS show has been leveraged in several applications in bioelectronics[122]. This property bestows OECTs with high transconductance, which translates into high signal amplification[27]. It comes, however, at the expense of cut-off frequency. The volumetric doping/dedoping that occurs across the whole bulk of the organic film makes OECTs response time decrease as a function of channel thickness. Still, OECTs have been used in biosensing and electrophysiology, where signals range from quasi-DC up to several kHz[127]. A proper balance needs to be struck between the appropriate channel thickness that maximises transconductance while preserving a desired cut-off frequency, in order to optimise device performance[67]. Our findings for transconductance and cut-off frequency of OECTs with varying channels thickness validate this trade-off and are in quantitative agreement with the predictions of Bernards model. With respect to noise, we found that relative noise in OECTs decreases non linearly with the channel thickness. This suggests that a large channel thickness is not only desirable because it increases transconductance but also because it provides a higher SNR and a lower LOD, with the trade-off being cut-off frequency. This can be overcome though by using a different OECT architecture[136]. It should also be noted that V_{rms} tends to saturate for high polymer thickness, suggesting that no significant improvement in SNR is achieved for particularly thick OECT channels.

The analysis of our data showed that the decrease in noise was consistent with the prediction of the charge noise model for OECTs that exhibit a channel thickness within 300 nm. However, when we increased the channel thickness to values above 1 µm, the model underestimated the measured values of noise. We tried to interpret this deviation by applying a more sophisticated model that considers fluctuations in both carrier number and carrier mobility. This model, which was originally developed for field-effect transistors[145,150], introduces an additional factor in S_{Id}/I_d^2 that is proportional to the gate capacitance and hence, predicts a more moderate decrease of relative noise with channel thickness. Despite the fact that this additional

factor was not able to explain the observed deviation in OECTs with a thicker channel, a description of the augmented noise model is given in the section below.

4.3.2 Noise modelling

The charge noise model attributes noise to fluctuations in the number of charge carriers in the channel of the transistor. The normalised power spectral density of the drain current is linked to the power spectral density of the gate voltage as:

$$\frac{S_{I_d}}{I_d^2} = \frac{g_m^2}{I_d^2} * S_{V_g} \, , \tag{4}$$

with[109]:

$$S_{V_g} = \frac{S_q}{C^2} \tag{5}$$

where S_q is constant for a given frequency and channel dimensions and C is the gate capacitance. In OECTs, the capacitance is proportional to the thickness d of the channel, meaning that relative noise scales as $1/d^2$.

A more sophisticated model can be derived by assuming that noise arises from both fluctuations in carrier numbers in the channel and corresponding changes induced in the carrier mobility. We write[150]:

$$\Delta I_d = \frac{dId}{dVg} \Delta V_g + \frac{\partial Id}{\partial \mu} \Delta \mu \, . \tag{6}$$

Friedlein et al. showed that the carrier mobility in PEDOT:PSS OECTs can be described as[70]:

$$\mu = \mu_o \left(\frac{p}{p_o}\right)^{\beta}, \tag{7}$$

where p is the hole concentration, μ_o is a mobility pre-factor and p_o is the zero-field hole concentration, which is equal to the density of sulfonate groups SO_3^- compensating holes in the PEDOT:PSS film[67]. The exponent β is found to be ~1 for PEDOT:PSS OECTs[70].

Based on the Bernards model[33], the hole density in the channel is :

$$p = SO_3^- - \frac{C^*}{e} V_g \,, \tag{8}$$

with C^* is the volumetric capacitance and e the absolute value of the charge of an electron.

By combining Eqs. 7 and 8 we get:

$$d\mu = \mu_o \frac{-C^*}{eSO_3^-} \, dV_g \,, \tag{9}$$

where C^* is the capacitance of the film per volume area.

From the Bernards model we can get:

$$\frac{dI_d}{d\mu} = \frac{I_d}{\mu_o} \,, \tag{10}$$

Combining the above, Eq. 6 can be rewritten as:

$$dI_d = g_m * \mathrm{d}V_g - I_d * \frac{C^*}{eSO_3^-} \, dV_g \,, \tag{11}$$

By integrating we get the expression:

$$\frac{S_{I_d}}{I_d^2} = \left(1 - \frac{C^*}{eSO_3^-} * \frac{I_d}{g_m} \right)^2 \left(\frac{g_m}{I_d} \right)^2 S_{V_g} \,. \tag{12}$$

The extra term on the right-hand side of Eq. 12 (compared to Eq. 4) does not depend on channel thickness, hence the relative noise still scales as $1/d^2$, as determined by Eq. (5).

4.4 Conclusion

In this section, we investigated how channel thickness impacts the noise characteristics of PEDOT:PSS OECTs. We found that relative noise decreases with channel thickness. When the channel thickness increased from 140 nm to 315 nm, the decrease in noise was consistent with the prediction of the charge noise model. However, this model was not able to properly explain

our experimental data for OECTs with 1330nm channel thickness. Our results on metrics such as signal-to-noise ratio and limit of detection show that OECTs compare favourably to other transistor technologies, including graphene transistors and electrodes. This work demonstrates that OECT-based transducers should be designed for the maximum possible thickness, as determined by the cut-off frequency requirements of the application.

Chapter 5

Organic electrochemical transistors for wearable and sensing applications

5.1 Introduction

Wearable devices have seen an increase in their applicability due to the advantages they bring such as health monitoring, analyte detection and electrophysiology activity sensing. Recent reports from the World Health Organization have shown that cardiovascular diseases are the main cause of death worldwide, resulting in almost one third of global deaths[151]. A healthy lifestyle can reduce the rate at which such diseases appear, however, early detection is equally important. As a result, methods that allow the detection of early signs or provide a consistent way of health monitoring have attracted a great deal of attention. Currently existing devices in clinical applications include the use of Ag/AgCl electrodes to record electrophysiology signals from the human body. Ag/AgCl electrodes are disposable and provide a good quality signal. They do, however, suffer from connectivity issues, they are limited to short term measurements due to the gel they utilise to interface with the skin[152], and they can cause skin irritation or allergic reactions[153]. Electrodes coated with Poly(3,4-ethylenedioxythiophene):poly(styrene sulfonate), PEDOT:PSS, have been developed on different substrates, including paper[154], polyimide[155] and textiles[156] as an alternative to record electrocardiography and electromyography signals.

As the needs of the biomedical society keep on rising, more inexpensive, biocompatible, non-invasive technologies have been employed to assist with that cause. Organic electrochemical transistors (OECTs) offer the ability to amplify any electrophysiology signal collected from muscles, skin or brain. They can also be fabricated with PEDOT:PSS, a material which is used to enhance the properties of multiple electronic devices and can be sterilised, allowing for direct clinical translation[157]. OECTs architecture bestows them with a conductivity which corresponds to the doping state of the channel material. Any changes in the electrolyte in which they are submerged (i.e. voltage fluctuations, molecule motion) leads to the exchange of ions with PEDOT:PSS and thus, changes the output current. Such properties combined with their superior performance in electrophysiology recordings compared to electrodes[6], made OECTs a champion candidate for cutaneous and biosensing applications. OECTs have been applied to interface with the skin and record different types of signals, including ECG, EMG and EEG[90,135,158]. They have also found fertile ground in biosensing and health monitoring applications as they can operate as transducers, enabling the detection of analytes and metabolites. Similarly to recording an electrophysiology signal by detecting changes in the doping state of the channel film as a result of a voltage signal in the gate, OECTs can detect the interaction of a redox enzyme with a metabolite due to the transfer of an electron to the gate terminal[4]. OECTs have been used to detect a variety of analytes (glucose, lactate, cholesterol)[138], uric acid[159], alcohol[160] and ph changes[161].

In this study we apply the design rules that we established in Chapters 3 and 4[115,162] to fabricate a flexible, biocompatible device that can be used for cutaneous and biosensing purposes. We demonstrate that the noise level of our device, despite being higher compared to the OECT devices fabricated onto glass, is adequate for non-invasive electrophysiology. In addition, we show the ability of our transistors to record signals of varying amplitude and frequency in an artificial simulated electrode configuration.

5.2 Results and discussion

5.2.1 Characterisation of flexible devices

Flexible devices for this work were fabricated as described in Chapter 2. Figure 5.1 shows the output and transfer curves of a representative OECT from the flexible device. All devices were characterised in a phosphate-buffered saline (PBS) solution with the use of a Ag/AgCl electrode as the gate. Figure 5.1 a) shows how the drain current scales as a function of the bias voltage, V_d, under the application of different gate voltages (ranging from 0 to 0.6 V from bottom to top). Higher gate voltages signify the injection of a greater quantity of cations from the electrolyte, leading to a larger decrease in the conductivity of the PEDOT:PSS film and thus, to lower current values. The transfer characteristics of the same OECT are presented in Figure 5.1 b). A maximum transconductance of ~2.5 mS was achieved at a gate voltage of – 0.2 V; V_d was constant through the measurement and was set at – 0.6 V.

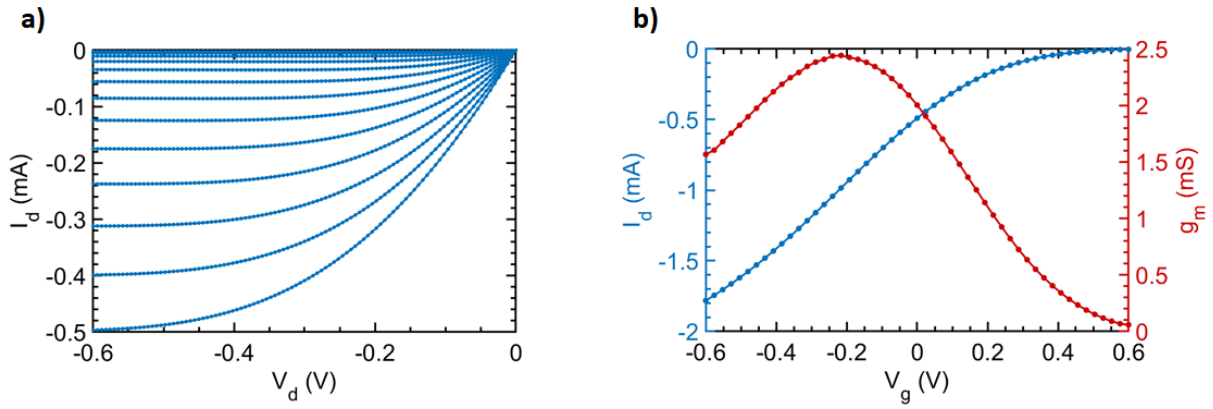

Figure 5.1 a) Output curve of a representative OECT on the flexible device, illustrating the variation of I_D as a function of V_d for different gate voltages. V_g was ranging from 0 to 0.6 V with a 50 mV step. b) Transfer curve of a representative OECT, showing the variation of transconductance as a function of V_g for a constant V_d of – 0.6 V.

5.2.2 Noise characteristics

To better understand the performance of our transistors, we proceeded with the noise analysis of the flexible devices. Figure 5.2 shows the noise behaviour of a representative device. The power spectral density of the current fluctuations as a function of frequency is highlighted in Figure 5.2 a). In these measurements V_{gs} was chosen to vary from 0 to 0. 5 V and V_d was set at – 0.2 V. The normalised expression of the PSD is presented in Figure 5.2 b), where a division with the square current was performed. In contrast to previous measurements in glass slide devices, we operated the devices with a lower V_d (- 0.2 V instead of - 0.5). This change was performed to account for the amplifier gain that was used to collect the current and reduce the power consumption of the device, as high power consumption can be a limiting factor in some electrophysiology applications. Our graphs show that both the PSD and the normalised PSD are decreasing as a function of frequency, a behaviour that is typical for flicker noise, however, the curves are reaching a plateau in a much lower frequency compared to previously reported studies[109,115,162]. We also plotted the variation of $S_{Vg}^{1/2}$ as a function of gate voltage (Figure 5.2 c) and find a good agreement in the reported values to the glass slide OECTs with the thinnest PEDOT:PSS channels[162]. An average value of 1.32 $\mu VHz^{-1/2}$ for $S_{Vg}^{1/2}$ and 17.6 μV for V_{rms} were calculated (N = 8 devices). Our results indicate that the noise level of the fabricated flexible devices is higher compared to previous OECTs, fabricated onto glass slides.

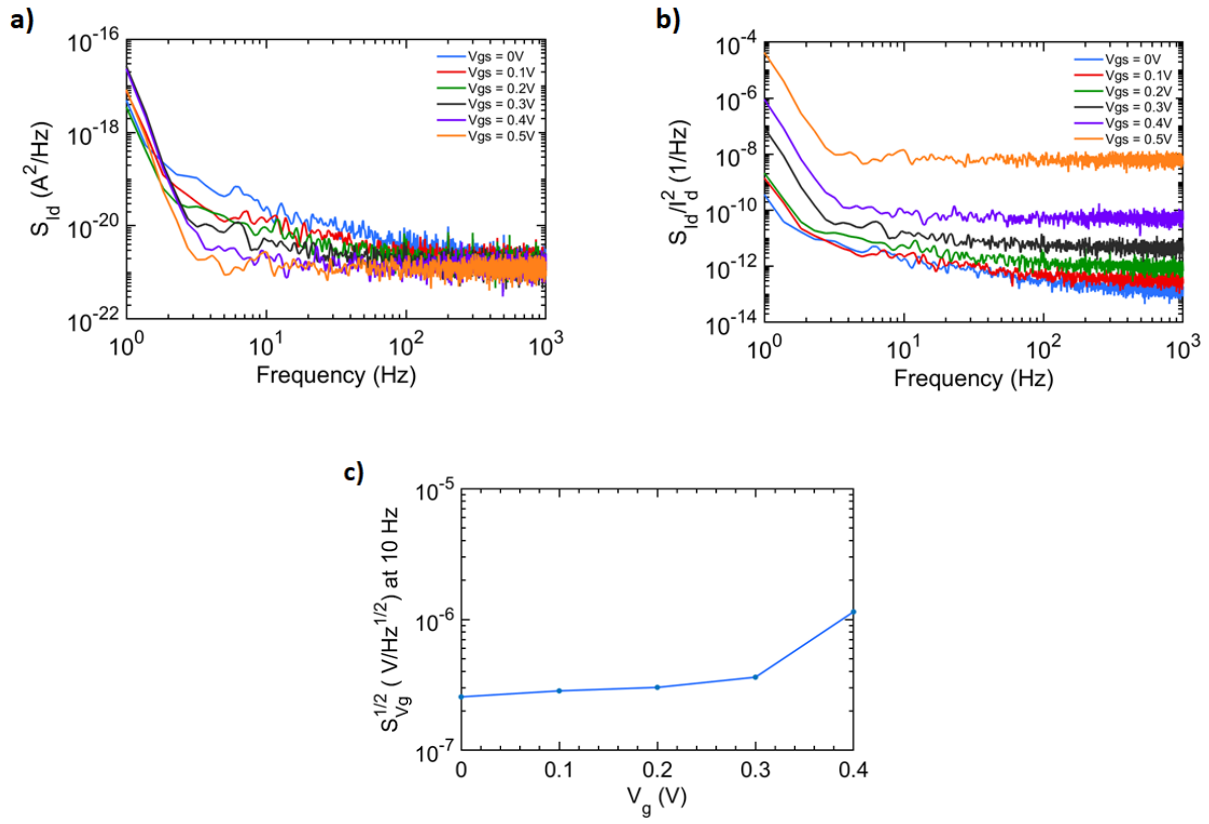

Figure 5.2 Noise characteristics of a representative OECT on a flexible device. Power spectral density S_{Id} (a) and normalised power spectral density S_{Id}/I_d^2 vs. frequency for different gate voltages; V_d was set at – 0.2 V. c) Root square gate voltage noise vs. V_g for the same device, showing the limit of detection of the transistor.

5.2.3 Simulated signal detection

To test the performance of our transistors we designed an artificially simulated environment that uses two gold electrodes, closely spaced to each other. The electrodes were insulated with PaC and only the tips were left exposed. They were submerged in a PBS solution and a waveform generator was used to create electric pulses (sine waves of varying amplitude and frequency) between the two. The flexible device was also submerged in the solution, with a Ag/AgCl electrode being used as a gate terminal to apply zero voltage. The approach in this

experimental *in vitro* set up was to test the ability of our devices to record signals coming from electrophysiology activity. A series of sine waves with different amplitudes and frequencies were applied from the waveform generator and the current changes were recorded. Figure 5.3 illustrates the configuration used for the *in vitro* measurements.

Figure 5.4 shows the fluctuations in the drain current after the application of a 100 mV pulse, with different graphs corresponding to different frequencies (varying from 1 Hz to 1kHz). OECTs were biased with a V_d of – 0.6 V while the gate was grounded. As seen from Figure 5.4, the amplitude of the signal is high enough to be easily recorded from the OECTs. In contrast, when we reduced the signal to 4 mV (which was the limit of the waveform generator) the OECT recordings were not accurate representations of the applied signal (Figure 5.5). We also observed that for low frequencies (Figure 5.5 a) some instabilities of the drain current were detected. In addition, despite not changing the bias conditions of our devices the steady state current was found to vary between measurements; we believe that such deviations might originate from connectivity issues with the flexible cable that was bonded on the device. Figure 5.6 highlights our previous observations by showing the relative modulation of the drain current as a function of the generated signal frequency. It should also be noted that for amplitudes between the ones described above, the transistors were performing similarly, i.e. the signal quality was high up to approximately 10 mV.

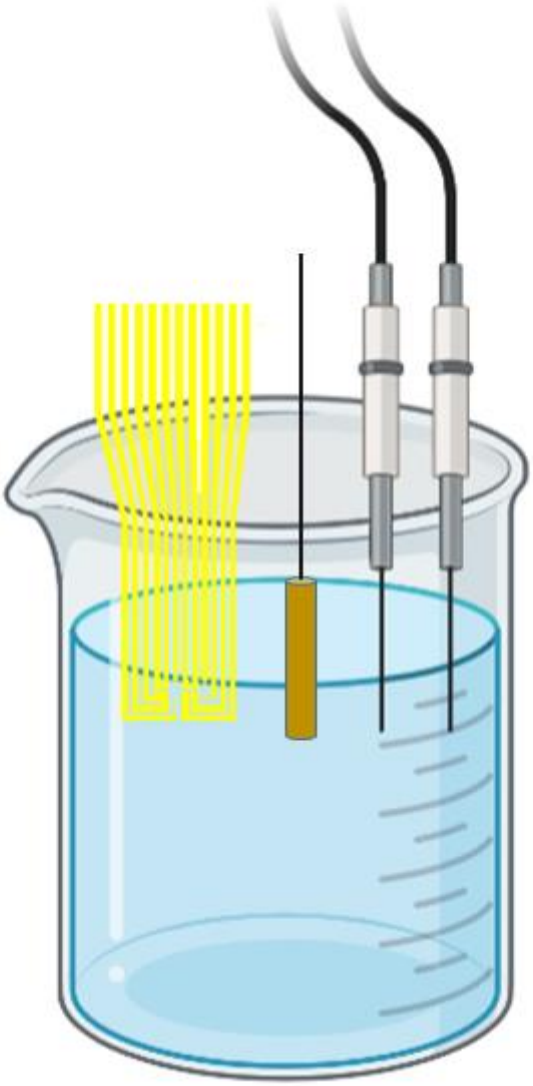

Figure 5.3 Schematic of the configuration used to record artificially generated signals. The flexible device was submerged into the electrolyte, which was PBS in this case, and it was recording the electric pulses being generated by the two gold electrodes. A Ag/AgCl electrode was also used to supply zero gate voltage and assist with the bias of the OECTs.

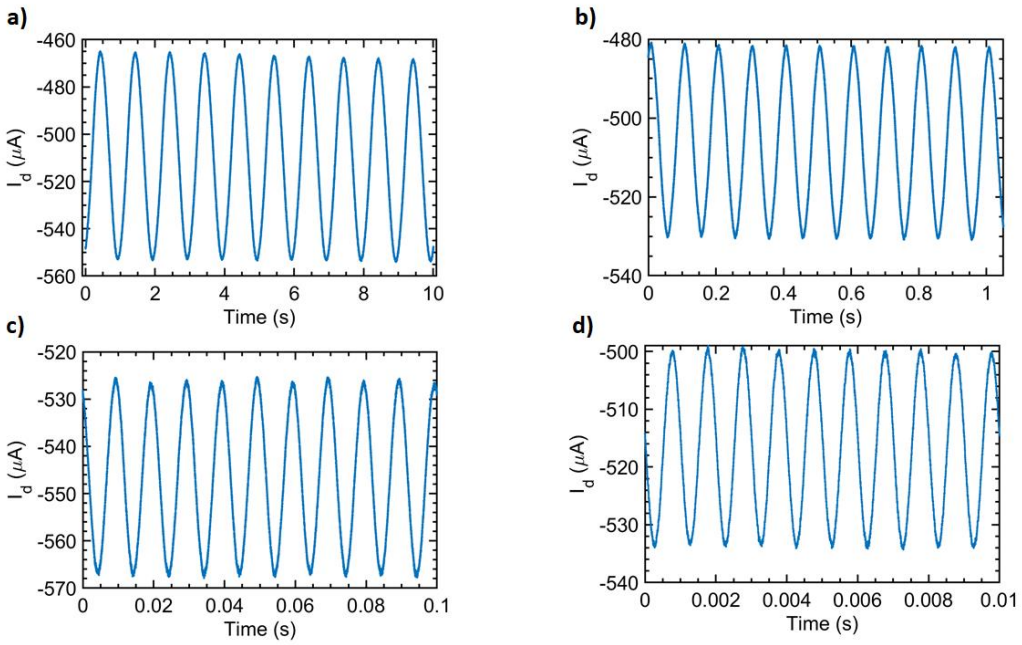

Figure 5.4 Changes in the drain current as a result of the application of different sine waves with an amplitude of 100 mV and a frequency of 1 Hz (a), 10 Hz (b), 100 Hz (c) and 1 kHz (d).

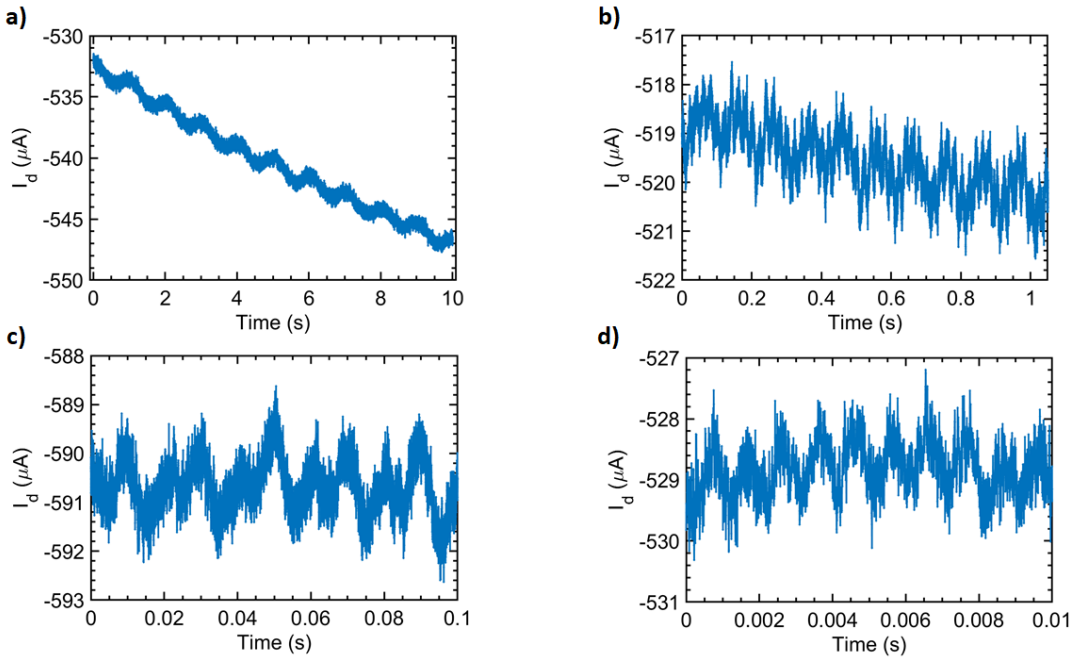

Figure 5.5 Changes in the drain current as a result of the application of different sine waves with an amplitude of 4 mV and a frequency of 1 Hz (a), 10 Hz (b), 100 Hz (c) and 1 kHz (d).

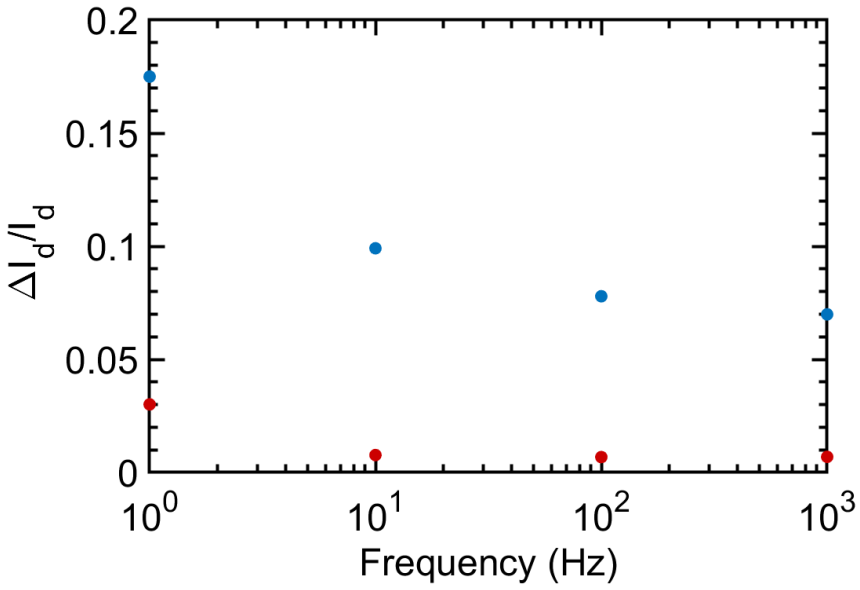

Figure 5.6 Relative modulation of the drain current as a function of the frequency of the generated pulse. Blue dots correspond to a signal of 100 mV amplitude, whereas red dots correspond to a signal of 4 mV.

5.2.4 Discussion

In this study we fabricated a flexible device with the greater aim of testing its applicability in electrophysiology. To optimise the performance of the device, we applied the design rules that we established in our previous work[115,162] in order to achieve maximum signal amplification and minimum noise. The characterisation of the device showed that peak transconductance was obtained for negative values of the applied gate voltage, however, the gain at zero V_g was sufficient enough to allow efficient operation. In future work, we propose tuning the architecture of the device, such as the channel dimensions, to shift maximum g_m at zero Volts[39]. The analysis of the noise characteristics of our transistors showed that the noise level of the flexible device is slightly higher compared to OECTs fabricated on glass[162]. In addition, the variation of the measured PSD as a function of frequency was found to deviate from previously reported flicker noise behaviour. This trend was observed for most of the studied devices, indicating that more analysis might be needed to ensure that such behaviour is attributed to the devices and not to

external factors. A potential issue that could arise in flexible devices is the interface of the measuring set up with the PaC substrate. In conformable substrates, a soft contact needs to be established to avoid damaging the gold pads, an issue that is not present when the device is fabricated onto rigid substrates (glass, silicon, etc.).

Finally, an artificially simulated electrode configuration was employed to test the performance of OECTs to record signals of different amplitude and frequency. Our devices showed good performance in a frequency bandwidth that varied from 1 Hz to 1 kHz, a range that is more than adequate for most electrophysiology signals[20]. A degradation in the signal quality was found as a function of the reduction in pulse amplitude. Such behaviour is expected and is linked to the recording limitations of OECTs as well as the nature of the experimental set up. In this configuration, we used insulated gold wires that were closely spaced as the signal source, and maintained a constant distance through the measurements. As a result, the picked up signal from the OECTs was much lower compared to a configuration where a Ag/AgCl is used as an active gate electrode. In summary, our flexible device showed good performance and has the potential to be applied in a variety of wearable and sensing applications, including invasive electrophysiology applications (described in chapter 5).

5.3 Conclusion

In this work we fabricated a flexible device using the design rules we established in previous chapters and tested its potential to be applied in electrophysiology applications. Characterisation of the device revealed that some tuning in the architecture might be needed to further optimise the operation point. Our noise analysis showed that the noise level of our flexible devices is higher to those previously reported, with a higher limit of detection and V_{rms} being observed. More research is required to examine the origins of such deviations. By utilising an artificial electrode configuration, we tested the recording capabilities of our devices and found

that our transistors are adequate for electrophysiology recordings. We believe that this technology has the potential to be used in a variety of electrophysiology applications.

Chapter 6

High quality epidural recordings using organic electrochemical transistors

6.1 Introduction

Understanding the mechanisms that the brain uses to communicate and process stimuli from the environment has been a topic that attracted a great deal of attention over the past few decades. To assist them with this task, scientists have employed microelectrode arrays using different technologies (Utah arrays, Michigan probes) to interface with the brain and record the electrochemical signals produced by the exchange of ions between the cell membranes of neurons (more information in Chapter 1)[25,26,127]. The information derived is used to analyse the behaviour of the brain and can be connected to specific motor or sensor activity. The latter has given birth to brain computer interfaces (BCIs), which are computer driven systems built to interact with the nervous system[20,163]. BCIs utilise signals collected from the brain to control external devices such as two dimensional cursors[164], prosthetic limbs[165,166] and wheelchairs[167]. Consequently, BCIs have been employed to assist with motor,[168] cognitive rehabilitation[169] and restore lost functionality in patients with paralysis[170] and paraplegia[171].

The invasiveness of the method used in a BCI is of paramount importance as it is directly linked to the amplitude and the frequency spectrum of the recorded signals. Typical oscillations corresponding to brain activity include delta (1-4 Hz), theta (4–8 Hz), alpha (7-14) beta (13-30 Hz) low and high gamma (30-150 Hz), as well as ripples (100-200 Hz)[127,172]. These oscillations of the neuronal circuitry are ultimately formed by single neuron activity (1-4 kHz). Non-invasive procedures involve the usage of electrode arrays placed on the scalp (electroencephalography (EEG)), less invasive methods employ arrays placed on the surface of the brain (electrocorticography (ECoG)), whereas more invasive methods utilise penetrating probes that pierce into the brain parenchyma[20]. Typically, more invasive methods allow recordings of higher frequency components from smaller volumes of tissue (e.g. individual neurons), increasing the spatio-temporal resolution of the received information. Although penetrating probes provide higher quality signals, their performance has been shown to significantly decline in long term recordings[2]. The main reason for this reduction lies within the response of the immune system of the human brain. The introduction of a foreign object triggers an inflammatory response, resulting in the encapsulation of the probe by an inactive layer of tissue. This process is known as “foreign body response” and has been linked to a variety of factors such as the insertion tissue damage[173,174], the blood brain barrier breach[175], the toxicity of the probe materials[176] and the mechanical mismatch between the implanted probe and the neural tissue[18,177].

It becomes apparent that a good balance between adequate signal quality and invasiveness needs to be struck to optimise the performance of a recording method. While EEG recordings are non-invasive and show good performance[164], their resolution is not sufficient for most BCI applications[178]. On the other hand, ECoG recordings typically consist of multiple grouped electrical potentials collected from the cortex of the brain (local field potentials (LFPs)). LFPs offer the advantage of providing higher temporal and spatial resolution compared to EEG signals. As an electrophysiology technique, ECoG does not necessitate penetration of the neuronal tissue, making it an excellent candidate for neuroscientists to study brain activity. ECoG microelectrode arrays have been used to assist with brain mapping[179] and localisation of epileptogenic zones[180]. Recording of ECoG signals can be performed above or below the dura,

leading to epidural or subdural activity respectively[6,181]. The presence of the dura can affect the quality of the recordings, with researchers demonstrating that small sized electrodes exhibited a higher signal quality when placed subdurally[182]. When used for chronical implantations though, epidural recordings have been shown to exhibit similar signal-to-noise ratio (SNR) to their subdural counterparts, a result that could be linked to the foreign body reaction triggered by the removal of the dura[183]. As a result, epidural recordings are preferred in a chronic implant environment due to the reduced risk they present for the patient. These findings pave the way for further reducing the invasiveness of the recording method whilst obtaining high SNR recordings.

An alternative method to record signals from brain activity is by using transistors instead of electrodes. A transistor is a three terminal device which can translate a voltage fluctuation on its input to a drain fluctuation on its output, expressed by transconductance. The main advantage that transistors bring compared to electrodes is the ability to amplify the recorded signal on the acquisition site, further improving the SNR. A promising architecture of organic transistors that offers high transconductance with biocompatibility is the organic electrochemical transistor (OECT). Poly(3,4-ethylenedioxythiophene) doped with polystyrene sulfonate (PEDOT:PSS) OECTs have been previously used for a variety of electrophysiology applications including myogram recordings in transgenic rats[184], ECG[90] and EEG signals in human volunteers[185], neuron stimulation[7] and subdural ECoG recordings in rats[6].

In this study, we explore the potential of OECT technology for minimally-invasive ECoG/BCI applications. We demonstrate the ability of OECTs to efficiently record signals from the cortex of an animal brain in a minimally invasive way, where the dura has not been removed. Simultaneous recordings of transistors and electrodes were collected in two different environments of ambiguous noise level. OECTs show a superior SNR compared to electrodes, particularly in the higher environmental noise environment.

6.2 Results and discussion

6.2.1 OECTs architecture

To collect electrophysiology signals from the cortex of the brain we fabricated our devices on a parylene C substrate with a thickness of approximately 2 µm. PaC has been widely used in biomedical applications due to the unique properties it provides in neural interfacing, such as biocompatibility and conformability[186–188]. Au was photolithographically patterned onto the PaC substrate leading to the formation of the transistor contacts, the electrodes and the interconnects. The dimensions of the Au interconnects were carefully chosen to minimise the voltage drop across the line, allowing for better performance and fair comparison between OECTs and electrodes. Another 2 µm layer of PaC was deposited on top to properly insulate each individual device. Reactive ion etching was performed to assist with the formation of the transistor channels and the electrode tips (more information provided in Chapter 2). Perforation holes were also patterned to ensure good conformation of the device on the cortical surface, as shown in Figure 6.1 a). Maintaining a constant flow of cerebrospinal fluid (CSF) in the cortex is important from both biological and recording perspective, as any alterations in the CSF fluid can compromise the stability of the recording. In addition, this design minimises any wrinkling and relative movement of the device to the recorded area of the cortex without compromising its mechanical stability[189]. The exposed parts were covered by a layer of PEDOT:PSS to establish connection between the source and drain contacts of the OECTs and reduce the impedance of surface electrodes. Each device consisted of 4 OECTs and 4 electrodes evenly distributed to allow simultaneous recordings of brain activity at comparable scale. The surface area of the transistor channels and the electrodes was designed to vary between 25 x 25 μm^2 to 100 x 100 μm^2 (Figure 6.1 b). Finally, anisotropic conductive film (ACF) bonding was used to establish connection between the pads of the recording devices and a flexible cable (Figure 6.1 c). The flexible cable was later connected into a zero insert force (ZIF, 14 pins, 0.5 mm spacing, ONECALL) connector to assist with the transmission of the recorded data via a custom made interface printed circuit board (PCB, 52.5 mm width, 40 mm height, 1.55 mm thickness, EuroCircuits).

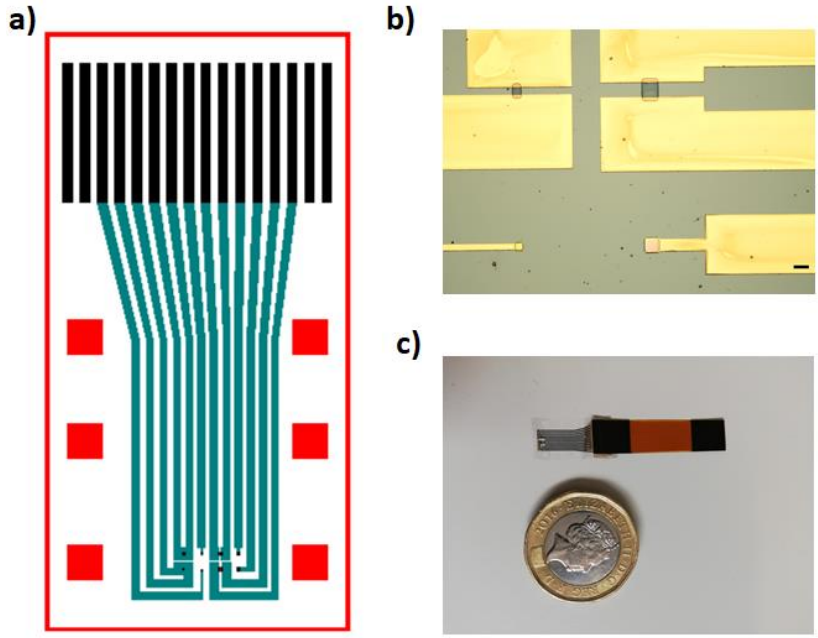

Figure 6.1 a) Schematic of an ECoG device. The Au interconnects are shown with green; black colour indicates the Au pads connected to the ZIF; red squares correspond to the perforation holes. b) Micrograph of an ECoG device. Scale bar is 50 µm. c) Image of an implantable ECoG device connected to a flexible cable.

6.2.2 OECTs *in vitro* characterisation

The fabricated OECTs were characterised in a phosphate-buffered saline (PBS) solution used as the electrolyte, with a stainless steel screw being submerged into the solution to act as a gate. Figures 6.2 (a,b) show the output and transfer characteristics of a representative OECT, biased with a constant drain voltage (V_d) of - 0.6 V. For the output curve the gate voltage (V_g) was chosen to vary between 0 to 0.6 V (Figure 6.2 a), whereas for the transfer curve V_g was ranging from - 0.6 to 0.6 V (Figure 6.2 b). A decrease in the drain current (I_d) is observed for higher gate voltages as a result of a reduction in the conductivity of the PEDOT:PSS film. This is caused by to the injection of cations from the electrolyte, leading to the dedoping of the polymer film. A maximum transconductance of ~ 2 mS was achieved at a V_g of - 0.2 V. Typically, characterisation of OECTs is performed with a non-polarisable Ag/AgCl electrode, however, this type of electrode

is toxic to the living tissue[190]. To accommodate comparisons between the two, we plotted the output and transfer characteristics of an OECT under the same conditions (both for V_d and V_g) with the use of a Ag/AgCl electrode, Figures 6.2 (c, d). Similar values for the drain current were observed, with transconductance exhibiting a slightly higher (~ 2.2 mS) peak value.

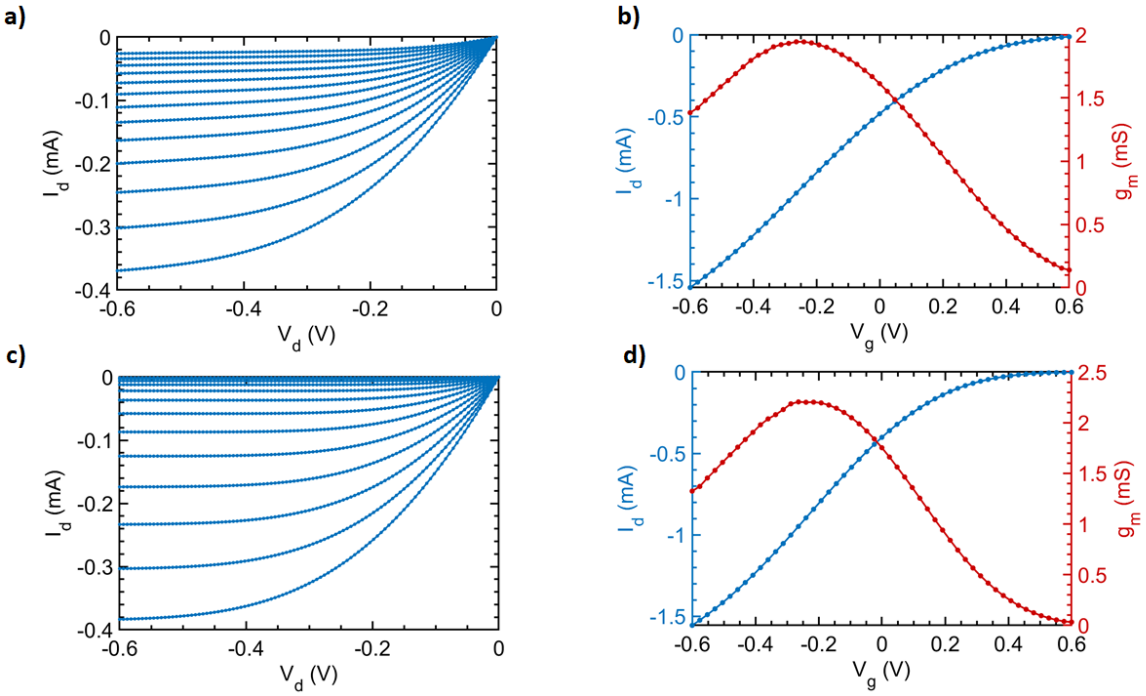

Figure 6.2 a) Output curve of an OECT, showing how I_D scales as a function of V_d for different gate voltages. V_g was ranging from 0 to 0.6 V with a 50 mV step. b) Transfer curve of an OECT, illustrating the variation of transconductance as a function of V_g for a constant V_d of – 0.6 V; a stainless steel screw was used as gate electrode. c) Output curve of an OECT. d) Transfer curve of an OECT; a Ag/AgCl electrode was used as gate. Similar bias conditions to graphs a) and b) were applied.

6.2.3 OECTs *in vivo* characterisation

After characterising the devices *in vitro*, we proceeded with the ECoG measurements in Sprague Dawley rats. The ECoG devices were peeled off from the silicon wafer and were placed on a glass substrate to assist with the alignment of an ACF bonding machine. A flexible cable was

attached to the pad area of the device to separate the implantable part from the non-implantable part, which was later connected to a ZIF connector. A custom made PCB was used as the interface board between the ECoG device and a precision source measure unit (SMU, Keysight B2902A). The PCB board consisted of a ZIF connector, allowing for the implantable probe to transmit the recorded data, and a double row pin header allowing the experimenter to choose between the electrode signals and the transistor signals. Oscillations in the somatosensory cortex were recorded as voltage fluctuations from the PEDOT:PSS electrodes and as drain current fluctuations from OECTs. Signals from both electrodes and transistors were acquired simultaneously and were directed to different individual channels on the same SMU. To avoid cross talk and minimise any interference from closely spaced devices, each measurement consisted of a single transistor and a single electrode. The measuring configuration was designed to provide identical recording conditions for both transistors and electrodes to allow for comparisons between them.

For the *in vivo* validation of the ECoG devices, we used Sprague Dawley rats that were under the effect of anaesthesia. After ensuring that the animals were properly anesthetised, a craniotomy was performed to reveal the cortex of the brain. Two stainless steel screws were implanted in the animal brain to assist with the ECoG recordings. For OECTs, the stainless steel screw was grounded and was used as the gate electrode of the transistor. For electrodes, the stainless steel screw was set to float and was used as the reference electrode of the configuration. After ensuring good connectivity with the PCB board, the ECoG devices were placed on the somatosensory cortex on top of the dura (Figure 6.3). A common source configuration was used for the OECT, similarly to previous work in subdural OECT recordings[6]. This enabled the transistors to work as transconductance amplifiers with a constant V_d of – 0.6 V. Figure 6.4 a) shows the recordings of low amplitude oscillations acquired by an OECT, with Figure 6.4 b) showing an equivalent recording from a surface electrode. Data in Figure 6.4 were filtered with a 50 Hz Notch filter to remove any noise added by main power lines. Despite being placed next to each other and thus, recording the same activity, the SNR of the signal recorded by OECTs was much higher compared to electrodes. To quantify SNR we used the mean value of the background signal in a period of low activity and subtracted it from the highest peak recorded in a period of

high activity, as well as the highest peak of biological noise recorded in a period of low biological activity. OECTs exhibited an SNR of 12.67 dB and PEDOT:PSS electrodes exhibited an SNR of 1.15 dB (averaged over five individual recordings).

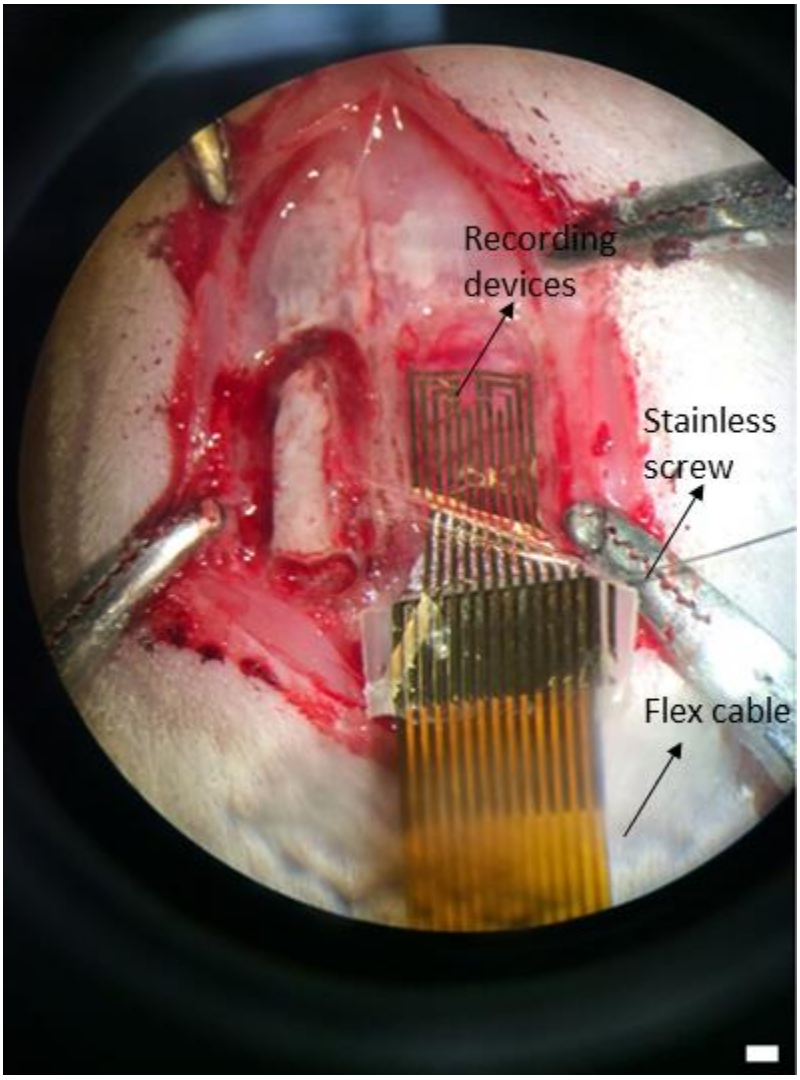

Figure 6.3 Intraoperative image illustrating an ECoG device, with the implantable part conforming on the surface of the animal cortex and the non-implantable part connected to a flexible cable. Scale bar 1 mm.

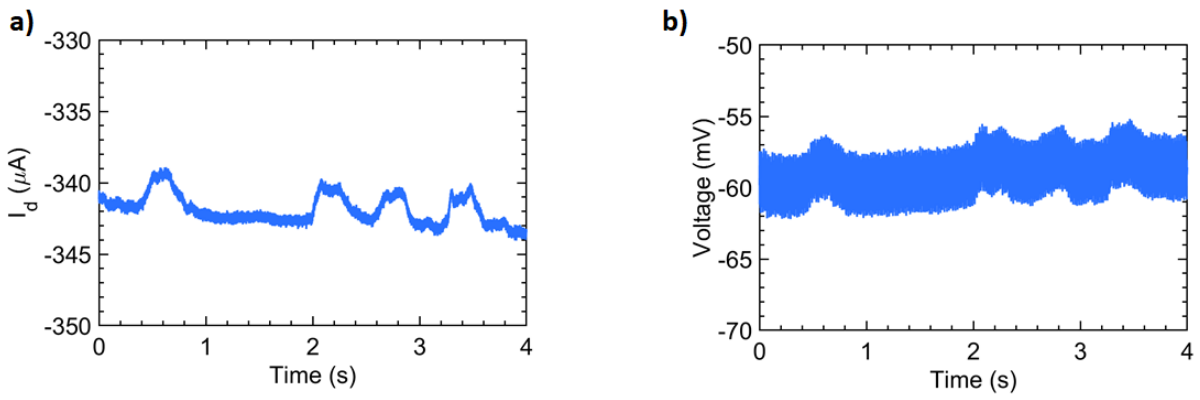

Figure 6.4 Recordings of ECoG signals above the dura of the somatosensory cortex using an OECT (a) and an electrode (b). The OECT was biased with a constant V_d of -0.6 V while the gate was grounded. 50 Hz noise was removed by applying a Notch filter to the acquired data. A much higher SNR is observed for OECTs compared to PEDOT:PSS electrodes.

As signals that correspond to LFPs show a frequency <200 Hz, we decided to further process the data by applying a bandpass filter (1 – 300 Hz). This provides a spatial-temporal resolution that is sufficient enough to drive a BCI whilst allowing to further reduce other sources of noise, both from non-neuronal physiological sources as well as from the acquisition system. Figure 6.5 shows how the recorded information appears after the application of the bandpass filter. OECTs continued to show higher SNR (20.13 dB) compared to their electrode counterparts (14.03 dB). By comparing the SNR of the two sets of data, we find that the signal quality recorded by the PEDOT:PSS electrodes was significantly improved. For OECTS, the addition of an extra filtering step contributed in better identifying the shape of the recorded LFPs, however, the main figures were clearly observed with minimal filtering. This can be attributed to the signal amplification of transistors happening on the spot of acquisition, in contrast to electrodes where the amplification occurs on a later stage by the measuring equipment.

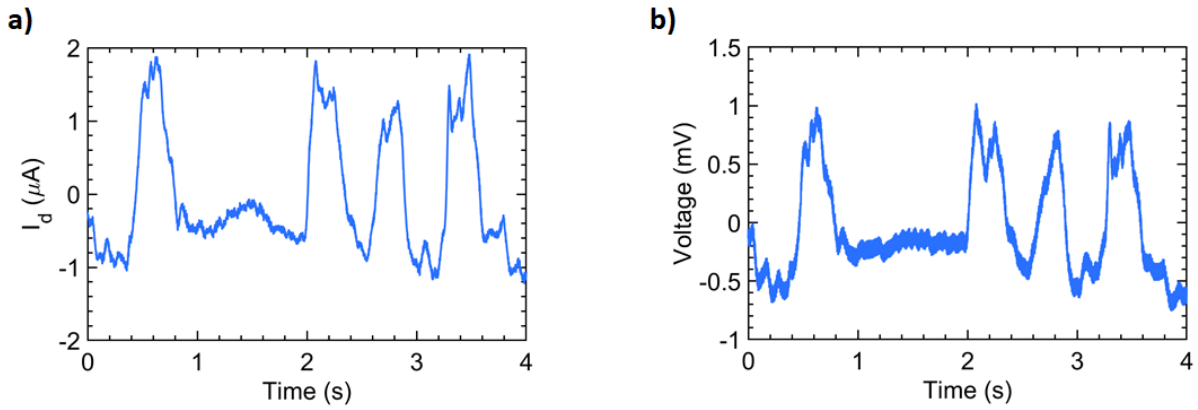

Figure 6.5 Recordings of ECoG signals above the dura of the somatosensory cortex using an OECT (a) and an electrode (b). The OECT was biased with a constant V_d of -0.6 V while the gate was grounded. Data was processed by applying a 50 Hz Notch filter and a bandpass filter (1 – 300 Hz). Despite showing improved quality compared to Figure 5.4, PEDOT:PSS electrodes still exhibited a lower SNR to OECTs.

To further investigate the limitations of our ECoG devices, we performed recordings in an environment with higher ambient noise. Figure 6.6 shows the recordings of epidural ECoG signals from a representative OECT (a) and a PEDOT:PSS electrode (b). Despite the higher ambient noise, the information derived from OECTs (Figure 6.6 a) clearly represents LFP activity. In the case of PEDOT:PSS electrodes, however, (Figure 6.6 b) the peaks of the recorded signal can barely be distinguished. The recording conditions were similar to the ones in the low noise environment, with data of Figure 6.6 being filtered with a 50 Hz Notch. In a second stage of processing, we applied a bandpass filter (1 - 300 Hz) to test the performance of both OECTs and electrodes; Figure 6.7 highlights our findings. As shown in Figure 6.7, the application of the bandpass filter significantly improved the quality of the signal. For OECTs, the recorded signal in Figure 6.7 a) resembles the one shown in Figure 6.6 a) with a much lower background noise. For the PEDOT:PSS electrode, the recorded signal in Figure 6.7 b) has similar peaks with the OECT, indicating that they recorded the same activity. Despite the improvement in the surface electrode recording, the background noise is quite high and affects the resolution of the derived information. These observations are also validated by the calculated SNR, which was found to be

19.06 dB for OECTs and 11.19 dB for the PEDOT:PSS electrode (averaged over five individual recordings). It should be noted that the SNR values reported for OECTs in the high ambient noise environment are approximately 1 dB lower than the ones calculated in low ambient noise, with electrodes showing a difference of approximately 3 dB.

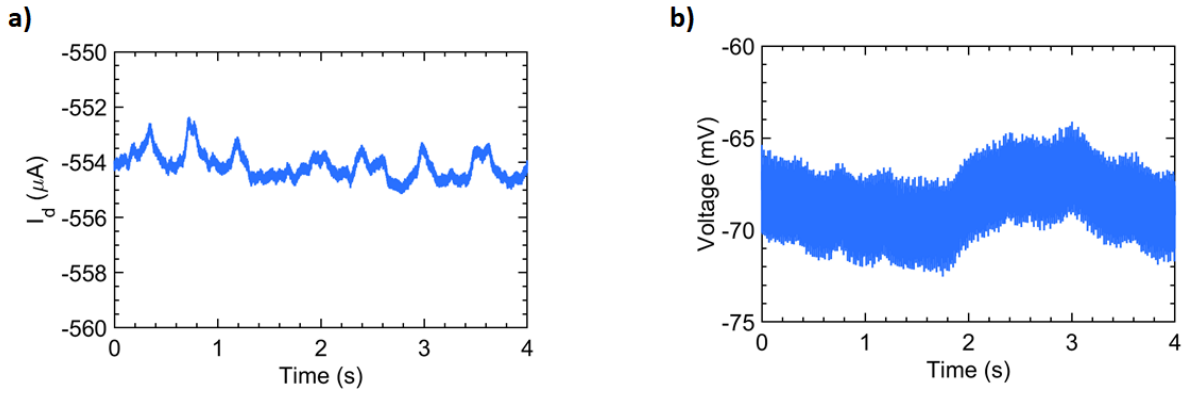

Figure 6.6 Recordings of ECoG signals above the dura of the somatosensory cortex using an OECT (a) and an electrode (b). The OECT was biased with a constant V_d of - 0.6 V while the gate was grounded. 50 Hz noise was removed by applying a Notch filter to the acquired data. It should be noted that despite the higher ambient noise, brain activity is clearly recorded by OECTs.

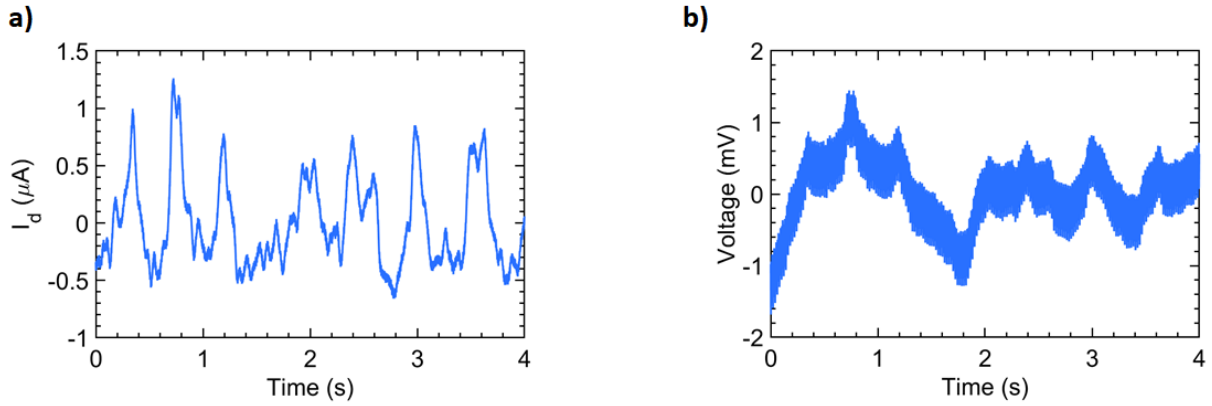

Figure 6.7 Recordings of ECoG signals above the dura of the somatosensory cortex using an OECT (a) and an electrode (b). The OECT was biased with a constant V_d of - 0.6 V while the gate was grounded. Data was processed by applying a 50 Hz Notch filter and a bandpass filter (1 – 300 Hz). Note that the superior SNR of OECTs compared to PEDOT:PSS electrodes.

In order to better investigate the spectrum of the recorded ECoG signals, we performed a time frequency analysis on our data. The power spectrum of an OECT and a PEDOT:PSS electrode as a function of time and frequency is shown in Figures 6.8 a), b) respectively. The experimental data was collected in a low noise environment and were filtered with a 50 Hz Notch and a bandpass (1 – 300 Hz) filter. Our results show that the resolution provided by OECTs is better compared to PEDOT:PSS electrodes. Despite having a higher signal power, the PEDOT:PSS electrode cannot resolve the recorded activity as accurately as an OECT, in agreement with the quality of the ECoG recordings above. A similar trend was observed in a higher ambient noise environment, shown in Figure 6.9.

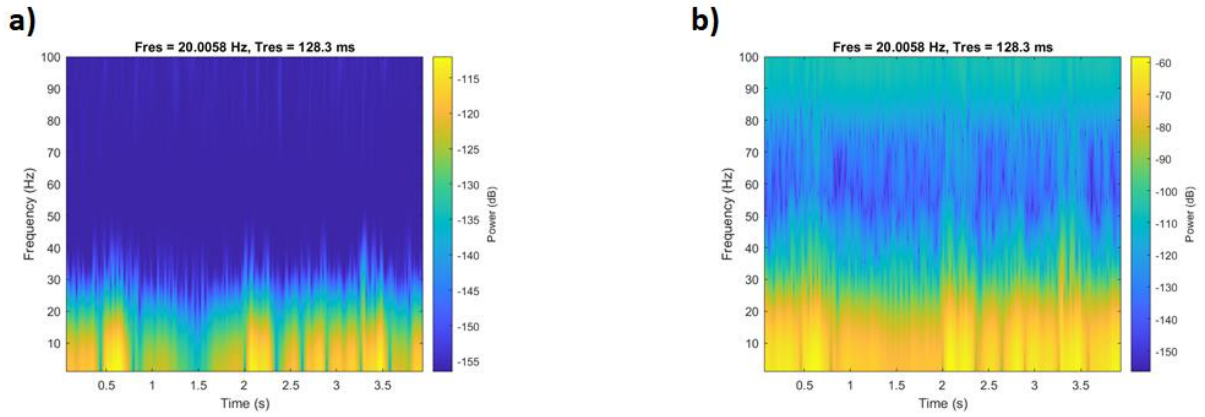

Figure 6.8 Time frequency analysis of a representative OECT (a) and a PEDOT:PSS electrode (b) placed epidurally to record ECoG signals, in a low ambient noise environment. The OECT was biased with a constant V_d of - 0.6 V while the gate was grounded. Data was processed by applying a 50 Hz Notch filter and a bandpass filter (1 – 300 Hz). Note that the OECT shows maximum signal power in a frequency range of 1 – 20 Hz, whereas the PEDOT:PSS electrode has a wider energy distribution.

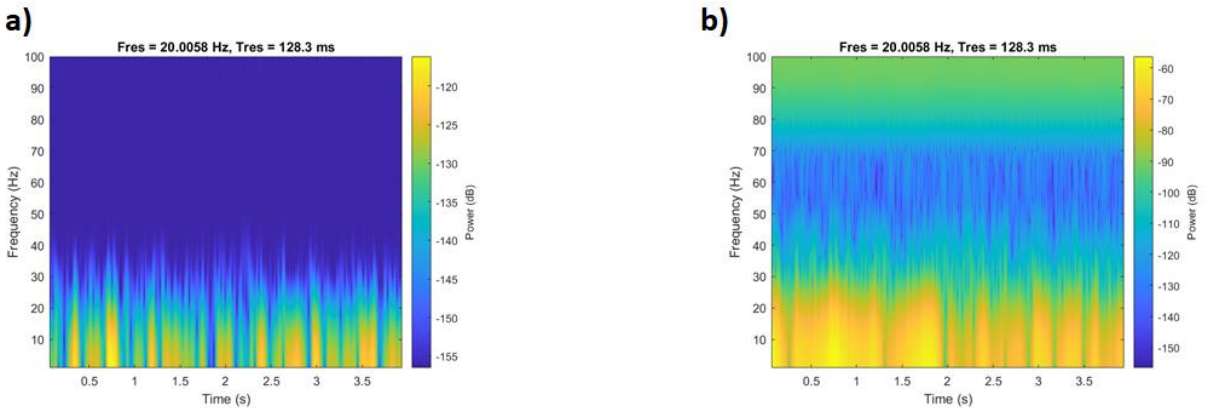

Figure 6.9 Time frequency analysis of a representative OECT (a) and a PEDOT:PSS electrode (b) placed epidurally to record ECoG signals, in a higher ambient noise environment. The OECT was biased with a constant V_d of - 0.6 V while the gate was grounded. Data was processed by applying a 50 Hz Notch filter and a bandpass filter (1 – 300 Hz). A wider frequency bandwidth in which the majority of the signal power is distributed is observed in OECTs.

6.2.4 Discussion

In this work we demonstrated the ability of OECTs to record LFPs from the somatosensory cortex of an animal brain without removing the dura layer. To obtain a better understanding of OECT advantages and limitations, we developed an ECoG device that consisted on both OECTs and PEDOT:PSS electrodes, closely spaced to record similar brain activity. Having a transistor architecture, OECTs have the drawback of needing a constant power supply to provide them with a bias voltage (V_d and potentially V_g, depending on the configuration) due to their operation as an active device, in comparison to passive electrodes. This can be a major limiting factor when it comes to chronic clinical implantations. However, if properly tuned, this property can be proven to be significantly beneficial as it allows to locally amplify the recorded signal and improve the SNR of the derived information. In previous work we showed that for a thickness of around 300 nm and at zero gate voltage, OECTS can be employed as biological transducers that exhibit both

maximum signal amplification and minimum noise level[115,162]. Here, we used a V_d of – 0.6 V to ensure saturation and grounded the gate to achieve a minimal noise level. Our work is inspired by previous research that showed the ability of PEDOT:PSS electrodes and OECTs to record both epidural[181] and subdural[6] ECoG signals in an acute recording configuration, and is aiming on providing a fertile ground for the application of OECTs in BCIs.

To achieve this we analysed the behaviour of OECTs and PEDOT:PSS electrodes in a simple configuration that included a commercially available source measure unit, a PCB interface board and a flexible ECoG device. Despite not including any evoked potentials, our set up allowed us to collect recordings of brain activity from anaesthetised animals. Our results show that the quality of the recorded information and the SNR of OECTs is much higher compared to surface electrodes. OECTs therefore allow the recording of brain activity with higher resolution due to the lower background noise level. This can be utilised to observe smaller features that cannot be resolved from electrodes whilst reducing the amount of time required to record the same information of brain activity with surface electrodes[6]. A key advantage of epidural recordings is the reduced invasiveness of the recording method, which translates into a reduced foreign body response and inflammation as well as lower associated risks (i.e. post-surgical compilations, infections, hematoma) making translation to the clinic easier. Our findings show that the LFPs recorded above the dura corresponded to typical brain activity under anaesthesia, paving the way for chronic applications. In addition, OECT recordings showed a high SNR even with a minimal filtering, as the main features of the ECoG signals could be observed with the application of a single 50 Hz Notch filter. By utilising this, more complex integrated circuits that involve OECTs and a simple stage of analogue filters could be implemented to assist with chronic BCIs.

6.3 Conclusion

In this study, we focused on exploring the ability of OECTs to record ECoG signals in a minimally invasive way. We designed an ECoG device that included both OECTs and PEDOT:PSS

electrodes and implanted our device on the brain somatosensory cortex of a rat model. Our results showed that our transistors were able to collect LFPs above the dura with high SNR and better resolution, compared to PEDOT:PSS electrodes. By avoiding the removal of the dura, we show that our technology is mature enough to provide sufficient information of brain activity to drive clinical/sensory/BCI applications with minimal invasiveness, ensuring a lower surgical risk and minimising the foreign body response. We envision that our findings will pave the way in implementing integrated circuits of OECTs for further use in chronical BCI applications.

Chapter 7

Conclusions and future work

7.1 Key findings

In this work, a study of the noise characteristics of OECTS is presented with more emphasis being placed on enhancing their performance for electrophysiology applications. To achieve that we analysed how some geometry parameters affect the steady state behaviour of OECTs and more importantly their noise profile. Our results allowed us to form new design rules for OECTs, that we used to engineer flexible devices for sensing and recording applications. A more thorough description, split in the chapters of this thesis, is given below.

In Chapter 3 we focused on the effect of geometry and bias conditions on the performance of OECTs. Transistor arrays were fabricated onto glass substrates with different contact overlaps; we defined contact overlap as the total length of the PEDOT:PSS stripe, including the channel of the transistor itself. Our findings show that a change in the percentage of contact overlap does not significantly alter the steady state transconductance and the output characteristics of OECTs. It does, however, reduce the cut-off frequency of the device, limiting the frequency bandwidth of OECTs. To test the behaviour of our devices further, we explored how noise scales as a function of the contact overlap and the applied bias. Our results demonstrate that the noise level of OECTs is independent of the contact overlap, highlighting that a good Ohmic contact is established. Relative noise was found to increase as function of the applied gate voltage but remains constant for different drain-source voltage. By combining our findings, a set of new design rules has been developed for OECTs with minimum noise. Our study suggests that OECTs should be designed with the minimum contact overlap defined by the

microfabrication technique used, to ensure the highest frequency bandwidth for the specified architecture. A greater aim of achieving maximum transconductance at zero gate voltage should also be considered, as it allows for maximum amplification whilst maintaining a minimum noise level.

In Chapter 4 we investigated how the thickness of the polymer film impacts noise in OECTs. OECTs similar to Chapter 3 were fabricated with multiple layers of PEDOT:PSS spun to form devices with three different channel thickness. In this work, we employed two different models to describe the behaviour of OECTs. Our results showed that a good fit with the charge noise model was observed, with significant deviations for high PEDOT:PSS thickness. The analysis performed on our devices revealed that relative noise decreases in a non-linear trend as a function of channel thickness. This can be combined with the increased signal amplification observed in OECTs with thicker channels to provide us with devices that exhibit both maximum signal amplification and minimum noise and thus, higher SNR. It should be noted however, that the increase observed in relative noise seemed to saturate after a particular polymer thickness. Higher PEDOT:PSS thickness also comes with the drawback of a decrease in the cut-off frequency. Our findings suggest that a good balance between signal amplification, noise and frequency bandwidth can be stricken for OECTs that exhibit a thickness of approximately 300 nm. Depending on the needs of the application, adjustments to this rule can be applied, for example, a greater thickness can be employed to further improve SNR when recording signals/events that spread across a narrower frequency window.

Having identified some new design rules that allow to engineer low noise OECTs, we proceeded with applying them on a flexible device in Chapter 5. The main goal of this study was to test the behaviour of OECTs fabricated onto a flexible substrate with the further aim of using them in electrophysiology applications. The dimensions of the gold interconnects were designed to match a commercially available ZIF connector while adjustments were made to ensure the voltage drop was minimal. By using an *in vitro* configuration we demonstrate that OECTs are adequate of recording low amplitude signals in agreement with our theoretical studies, making them an excellent candidate for wearable applications.

In Chapter 6 we used the same flexible device, reported in Chapter 5, to record electrophysiology signals from the somatosensory cortex of an animal brain. A key figure of this experimental set up was the invasiveness of the recording method. Our devices were placed on top of the dura to reduce the inflammatory response and collect ECoG signals. We compared our technology with PEDOT:PSS electrodes to highlight the advantages and limitations of our ECoG device. Our results demonstrate that OECTs recorded LFP signals with greater resolution than PEDOT:PSS electrodes and higher SNR. The quality of the signal was high enough to allow minimal filtering, when recorded by OECTs, and the derived information was sufficient to be used in BCI applications. We envision that this study will pave the way for high quality, less invasive applications of OECTs in different electrophysiology environments.

7.2 Future work

In this thesis multiple directions of further understanding the mechanisms of operation of OECTs were pursed with more focus on their applicability in electrophysiology. There are still, however, multiple avenues for future research. A topic that can lead to better understanding of the noise characteristics of OECTs is the applicability of the charge noise model as the thickness of the polymer film increases. As we showed in Chapter 4, both the charge noise model and the augmented model that we developed failed to interpret the behaviour of really thick OECTs. Despite identifying a good trade-off between noise, signal amplification and frequency response, we believe that research in this topic can shed more light and allow for further optimisation in the operation of OECTs. Another field that remains to be explored is the applicability of our flexible devices in a wearable application set up. In this work we showed that we can fabricate low noise OECTs on a flexible substrate and successfully applied that in an epidural recording set up, acquiring information of high resolution and SNR. We believe that the same architecture can be used in a cutaneous environment and allow the recording of electrophysiology signals such as EEG, ECG and EMG. Finally, it would be interesting to record ECoG signals both subdurally and epidurally and compare the derived information. Combined together, the results of previous

studies[6,181,183] and this work can potentially lay the foundations for enhanced recordings in BCI applications in a minimally invasive way.

References

1. Zhang, S., Kumar, P., Nouas, A. S., Fontaine, L., Tang, H. & Cicoira, F. Solvent-induced changes in PEDOT:PSS films for organic electrochemical transistors. *APL Mater.* **3**, 014911 (2014).

2. Chen, R., Canales, A. & Anikeeva, P. Neural recording and modulation technologies. *Nat. Rev. Mater.* **2**, 16093 (2017).

3. Berggren, M. & Richter-Dahlfors, A. Organic Bioelectronics. *Adv. Mater.* **19**, 3201–3213 (2007).

4. Rivnay, J., Inal, S., Salleo, A., Owens, R. M., Berggren, M. & Malliaras, G. G. Organic electrochemical transistors. *Nat. Rev. Mater.* **3**, 17086 (2018).

5. White, H. S., Kittlesen, G. P. & Wrighton, M. S. Chemical derivatization of an array of three gold microelectrodes with polypyrrole: fabrication of a molecule-based transistor. *J. Am. Chem. Soc.* **106**, 5375–5377 (1984).

6. Khodagholy, D., Doublet, T., Quilichini, P., Gurfinkel, M., Leleux, P., Ghestem, A., Ismailova, E., Hervé, T., Sanaur, S., Bernard, C. & Malliaras, G. G. *In vivo* recordings of brain activity using organic transistors. *Nat. Commun.* **4**, 1575 (2013).

7. Williamson, A., Ferro, M., Leleux, P., Ismailova, E., Kaszas, A., Doublet, T., Quilichini, P., Rivnay, J., Rózsa, B., Katona, G., Bernard, C. & Malliaras, G. G. Localized Neuron Stimulation with Organic Electrochemical Transistors on Delaminating Depth Probes. *Adv. Mater.* **27**, 4405–4410 (2015).

8. Verkhratsky, A., Krishtal, O. A. & Petersen, O. H. From Galvani to patch clamp: the development of electrophysiology. *Pflüg. Arch.* **453**, 233–247 (2006).

9. Hatsopoulos, N. G. & Donoghue, J. P. The Science of Neural Interface Systems. *Annu. Rev. Neurosci.* **32**, 249–266 (2009).

10. Neuron Communication | Biology for Majors II. https://courses.lumenlearning.com/suny-wmopen-biology2/chapter/neuron-communication/. Accessed 30/6/2021.

11. Nerve action potential andpropagation. in *Basic Physiology for Anaesthetists* (eds. Huang, C., Chambers, D. & Matthews, G.) 221–227 (Cambridge University Press, 2015). doi:10.1017/CBO9781139226394.051.

12. Pas, J. Flexible neural probes with a fast bioresorbable shuttle: From in vitro to in vivo electrophysiological recordings. 116.

13. *Brain-Computer Interfaces: Principles and Practice*. (Oxford University Press, 2012).

14. Molleman, A. *Patch Clamping: An Introductory Guide to Patch Clamp Electrophysiology*. (John Wiley & Sons, 2003).

15. Qing, Q., Jiang, Z., Xu, L., Gao, R., Mai, L. & Lieber, C. M. Free-standing kinked nanowire transistor probes for targeted intracellular recording in three dimensions. *Nat. Nanotechnol.* **9**, 142–147 (2014).

16. Xu, A. M., Aalipour, A., Leal-Ortiz, S., Mekhdjian, A. H., Xie, X., Dunn, A. R., Garner, C. C. & Melosh, N. A. Quantification of nanowire penetration into living cells. *Nat. Commun.* **5**, 3613 (2014).

17. Fendyur, A., Mazurski, N., Shappir, J. & Spira, M. E. Formation of Essential Ultrastructural Interface between Cultured Hippocampal Cells and Gold Mushroom-Shaped MEA- Toward "IN-CELL" Recordings from Vertebrate Neurons. *Front. Neuroengineering* **4**, (2011).

18. Rivnay, J., Wang, H., Fenno, L., Deisseroth, K. & Malliaras, G. G. Next-generation probes, particles, and proteins for neural interfacing. *Sci. Adv.* **3**, e1601649 (2017).

19. Buzsáki, G., Anastassiou, C. A. & Koch, C. The origin of extracellular fields and currents — EEG, ECoG, LFP and spikes. *Nat. Rev. Neurosci.* **13**, 407–420 (2012).

20. Thakor, N. V. Translating the Brain-Machine Interface. *Sci. Transl. Med.* **5**, 210ps17-210ps17 (2013).

21. Hill, N. J., Gupta, D., Brunner, P., Gunduz, A., Adamo, M. A., Ritaccio, A. & Schalk, G. Recording Human Electrocorticographic (ECoG) Signals for Neuroscientific Research and Real-time Functional Cortical Mapping. *J. Vis. Exp. JoVE* (2012) doi:10.3791/3993.

22. Jorfi, M., Skousen, J. L., Weder, C. & Capadona, J. R. Progress towards biocompatible intracortical microelectrodes for neural interfacing applications. *J. Neural Eng.* **12**, 011001 (2015).

23. Ludwig, K. A., Uram, J. D., Yang, J., Martin, D. C. & Kipke, D. R. Chronic neural recordings using silicon microelectrode arrays electrochemically deposited with a poly(3,4-ethylenedioxythiophene) (PEDOT) film. *J. Neural Eng.* **3**, 59 (2006).

24. Ludwig, K. A., Langhals, N. B., Joseph, M. D., Richardson-Burns, S. M., Hendricks, J. L. & Kipke, D. R. Poly(3,4-ethylenedioxythiophene) (PEDOT) polymer coatings facilitate smaller neural recording electrodes. *J. Neural Eng.* **8**, 014001 (2011).

25. Drake, K. L., Wise, K. D., Farraye, J., Anderson, D. J. & BeMent, S. L. Performance of planar multisite microprobes in recording extracellular single-unit intracortical activity. *IEEE Trans. Biomed. Eng.* **35**, 719–732 (1988).

26. Campbell, P. K., Jones, K. E., Huber, R. J., Horch, K. W. & Normann, R. A. A silicon-based, three-dimensional neural interface: manufacturing processes for an intracortical electrode array. *IEEE Trans. Biomed. Eng.* **38**, 758–768 (1991).

27. Khodagholy, D., Rivnay, J., Sessolo, M., Gurfinkel, M., Leleux, P., Jimison, L. H., Stavrinidou, E., Herve, T., Sanaur, S., Owens, R. M. & Malliaras, G. G. High transconductance organic electrochemical transistors. *Nat. Commun.* **4**, 2133 (2013).

28. Lin, P. & Yan, F. Organic Thin-Film Transistors for Chemical and Biological Sensing. *Adv. Mater.* **24**, 34–51 (2012).

29. Malliaras, G. G. Organic bioelectronics: A new era for organic electronics. *Biochim. Biophys. Acta BBA - Gen. Subj.* **1830**, 4286–4287 (2013).

30. Owens, R. M. & Malliaras, G. G. Organic Electronics at the Interface with Biology. *MRS Bull.* **35**, 449–456 (2010).

31. Yao, C. Organic electrochemical transistor based biomedical devices for electrophysiological recordings. (2015).

32. Liao, C., Zhang, M., Yao, M. Y., Hua, T., Li, L. & Yan, F. Flexible Organic Electronics in Biology: Materials and Devices. *Adv. Mater.* **27**, 7493–7527 (2015).

33. Bernards, D. A. & Malliaras, G. G. Steady-State and Transient Behavior of Organic Electrochemical Transistors. *Adv. Funct. Mater.* **17**, 3538–3544 (2007).

34. Inal, S., Rivnay, J., Leleux, P., Ferro, M., Ramuz, M., Brendel, J. C., Schmidt, M. M., Thelakkat, M. & Malliaras, G. G. A high transconductance accumulation mode electrochemical transistor. *Adv. Mater. Deerfield Beach Fla* **26**, 7450–7455 (2014).

35. Giovannitti, A., Nielsen, C. B., Sbircea, D.-T., Inal, S., Donahue, M., Niazi, M. R., Hanifi, D. A., Amassian, A., Malliaras, G. G., Rivnay, J. & McCulloch, I. N-type organic electrochemical transistors with stability in water. *Nat. Commun.* **7**, 13066 (2016).

36. Pitsalidis, C., Pappa, A.-M., Porel, M., Artim, C. M., Faria, G. C., Duong, D. D., Alabi, C. A., Daniel, S., Salleo, A. & Owens, R. M. Biomimetic Electronic Devices for Measuring Bacterial Membrane Disruption. *Adv. Mater.* **30**, 1803130 (2018).

37. Nilsson, D., Chen, M., Kugler, T., Remonen, T., Armgarth, M. & Berggren, M. Bi-stable and dynamic current modulation in electrochemical organic transistors. *Adv. Mater.* **14**, 51–54 (2002).

38. Rivnay, J., Owens, R. M. & Malliaras, G. G. The Rise of Organic Bioelectronics. *Chem. Mater.* **26**, 679–685 (2014).

39. Rivnay, J., Leleux, P., Sessolo, M., Khodagholy, D., Hervé, T., Fiocchi, M. & Malliaras, G. G. Organic electrochemical transistors with maximum transconductance at zero gate bias. *Adv. Mater. Deerfield Beach Fla* **25**, 7010–7014 (2013).

40. Donahue, M. J., Williamson, A., Strakosas, X., Friedlein, J. T., McLeod, R. R., Gleskova, H. & Malliaras, G. G. High-Performance Vertical Organic Electrochemical Transistors. *Adv. Mater.* **30**, n/a-n/a (2018).

41. Hess, L. H., Hauf, M. V., Seifert, M., Speck, F., Seyller, T., Stutzmann, M., Sharp, I. D. & Garrido, J. A. High-Transconductance Graphene Solution-Gated Field Effect Transistors. *Appl. Phys. Lett.* **99**, 033503 (2011).

42. Ohno, Y., Maehashi, K., Yamashiro, Y. & Matsumoto, K. Electrolyte-gated graphene field-effect transistors for detecting pH and protein adsorption. *Nano Lett.* **9**, 3318–3322 (2009).

43. Dankerl, M., Eick, S., Hofmann, B., Hauf, M., Ingebrandt, S., Offenhäusser, A., Stutzmann, M. & Garrido, J. A. Diamond Transistor Array for Extracellular Recording From Electrogenic Cells. *Adv. Funct. Mater.* **19**, 2915–2923 (2009).

44. Felderer, F. & Fromherz, P. Transistor needle chip for recording in brain tissue. *Appl. Phys. A* **104**, 1 (2011).

45. Li, B.-R., Chen, C.-W., Yang, W.-L., Lin, T.-Y., Pan, C.-Y. & Chen, Y.-T. Biomolecular recognition with a sensitivity-enhanced nanowire transistor biosensor. *Biosens. Bioelectron.* **45**, 252–259 (2013).

46. Yuan, H., Shimotani, H., Tsukazaki, A., Ohtomo, A., Kawasaki, M. & Iwasa, Y. High-Density Carrier Accumulation in ZnO Field-Effect Transistors Gated by Electric Double Layers of Ionic Liquids. *Adv. Funct. Mater.* **19**, 1046–1053 (2009).

47. Nasr, B., Wang, D., Kruk, R., Rösner, H., Hahn, H. & Dasgupta, S. High-Speed, Low-Voltage, and Environmentally Stable Operation of Electrochemically Gated Zinc Oxide Nanowire Field-Effect Transistors. *Adv. Funct. Mater.* **23**, 1750–1758 (2013).

48. Braga, D., Erickson, N. C., Renn, M. J., Holmes, R. J. & Frisbie, C. D. High-transconductance organic thin-film electrochemical transistors for driving low-voltage red-green-blue active matrix organic light-emitting devices. *Adv. Funct. Mater.* **22**, 1623–1631 (2012).

49. Cho, J. H., Lee, J., Xia, Y., Kim, B., He, Y., Renn, M. J., Lodge, T. P. & Frisbie, C. D. Printable ion-gel gate dielectrics for low-voltage polymer thin-film transistors on plastic. *Nat. Mater.* **7**, 900–906 (2008).

50. Sasa, S., Ozaki, M., Koike, K., Yano, M. & Inoue, M. High-performance ZnO/ZnMgO field-effect transistors using a hetero-metal-insulator-semiconductor structure. *Appl. Phys. Lett.* **89**, 053502 (2006).

51. Siddiqui, J., Cagin, E., Chen, D. & Phillips, J. D. ZnO thin-film transistors with polycrystalline (Ba,Sr)TiO3 gate insulators. *Appl. Phys. Lett.* **88**, 212903 (2006).

52. Xu, H., Zhang, Z., Xu, H., Wang, Z., Wang, S. & Peng, L.-M. Top-gated graphene field-effect transistors with high normalized transconductance and designable dirac point voltage. *ACS Nano* **5**, 5031–5037 (2011).

53. Moon, J. S., Curtis, D., Bui, S., Hu, M., Gaskill, D. K., Tedesco, J. L., Asbeck, P., Jernigan, G. G., VanMil, B. L., Myers-Ward, R. L., Eddy, C. R., Campbell, P. M. & Weng, X. Top-Gated Epitaxial Graphene FETs on Si-Face SiC Wafers With a Peak Transconductance of 600 mS/mm. *IEEE Electron Device Lett.* **31**, 260–262 (2010).

54. Meric, I., Han, M. Y., Young, A. F., Ozyilmaz, B., Kim, P. & Shepard, K. L. Current saturation in zero-bandgap, top-gated graphene field-effect transistors. *Nat. Nanotechnol.* **3**, 654–659 (2008).

55. Do, Q.-, Blekker, K., Regolin, I., Prost, W. & Tegude, F. J. High Transconductance MISFET With a Single lt;emphasis emphasistype="roman" gt;InAs lt;/emphasis gt; Nanowire Channel. *IEEE Electron Device Lett.* **28**, 682–684 (2007).

56. Tomioka, K., Yoshimura, M. & Fukui, T. A III-V nanowire channel on silicon for high-performance vertical transistors. *Nature* **488**, 189–192 (2012).

57. Nidhi, Dasgupta, S., Lu, J., Speck, J. S. & Mishra, U. K. Self-Aligned N-Polar GaN/InAlN MIS-HEMTs With Record Extrinsic Transconductance of 1105 mS/mm. *IEEE Electron Device Lett.* **33**, 794–796 (2012).

58. Bouzid-Driad, S., Maher, H., Defrance, N., Hoel, V., Jaeger, J.-D., Renvoise, M. & Frijlink, P. AlGaN/GaN HEMTs on Silicon Substrate With 206-GHz \rm MAX. *IEEE Electron Device Lett.* **34**, 36–38 (2013).

59. Hill, R. J. W., Moran, D. A. J., Li, X., Zhou, H., Macintyre, D., Thoms, S., Asenov, A., Zurcher, P., Rajagopalan, K., Abrokwah, J., Droopad, R., Passlack, M. & Thayne, I. G. Enhancement-mode GaAs MOSFETs with an In0.3 Ga0.7As channel, a mobility of over 5000 cm2/V ·s, and transconductance of over 475 µS/µm. *IEEE Electron Device Lett.* **28**, 1080–1082 (2007).

60. Cao, Q., Han, S., Tulevski, G. S., Zhu, Y., Lu, D. D. & Haensch, W. Arrays of single-walled carbon nanotubes with full surface coverage for high-performance electronics. *Nat. Nanotechnol.* **8**, 180–186 (2013).

61. Cao, Q., Kim, H., Pimparkar, N., Kulkarni, J. P., Wang, C., Shim, M., Roy, K., Alam, M. A. & Rogers, J. A. Medium-scale carbon nanotube thin-film integrated circuits on flexible plastic substrates. *Nature* **454**, 495–500 (2008).

62. Zschieschang, U., Hofmockel, R., Rödel, R., Kraft, U., Kang, M. J., Takimiya, K., Zaki, T., Letzkus, F., Butschke, J., Richter, H., Burghartz, J. N. & Klauk, H. Megahertz operation of flexible low-voltage organic thin-film transistors. *Org. Electron.* **14**, 1516–1520 (2013).

63. Klauk, H., Zschieschang, U. & Halik, M. Low-voltage organic thin-film transistors with large transconductance. *J. Appl. Phys.* **102**, 074514 (2007).

64. Yokota, T., Sekitani, T., Kato, Y., Kuribara, K., Zschieschang, U., Klauk, H., Yamamoto, T., Takimiya, K., Kuwabara, H., Ikeda, M. & Someya, T. Low-voltage organic transistor with subfemtoliter inkjet source–drain contacts. *MRS Commun.* **1**, 3–6 (2011).

65. Cui, Y., Zhong, Z., Wang, D., Wang, W. U. & Lieber, C. M. High Performance Silicon Nanowire Field Effect Transistors. *Nano Lett.* **3**, 149–152 (2003).

66. Inal, S., Malliaras, G. G. & Rivnay, J. Benchmarking organic mixed conductors for transistors. *Nat. Commun.* **8**, 1767 (2017).

67. Rivnay, J., Leleux, P., Ferro, M., Sessolo, M., Williamson, A., Koutsouras, D. A., Khodagholy, D., Ramuz, M., Strakosas, X., Owens, R. M., Benar, C., Badier, J.-M., Bernard, C. & Malliaras, G. G. High-performance transistors for bioelectronics through tuning of channel thickness. *Sci. Adv.* **1**, e1400251 (2015).

68. Kaphle, V., Liu, S., Al-Shadeedi, A., Keum, C.-M. & Lüssem, B. Contact Resistance Effects in Highly Doped Organic Electrochemical Transistors. *Adv. Mater. Deerfield Beach Fla* **28**, 8766–8770 (2016).

69. Friedlein, J. T., Rivnay, J., Dunlap, D. H., McCulloch, I., Shaheen, S. E., McLeod, R. R. & Malliaras, G. G. Influence of disorder on transfer characteristics of organic electrochemical transistors. *Appl. Phys. Lett.* **111**, 023301 (2017).

70. Friedlein, J. T., Shaheen, S. E., Malliaras, G. G. & McLeod, R. R. Optical Measurements Revealing Nonuniform Hole Mobility in Organic Electrochemical Transistors. *Adv. Electron. Mater.* **1**, n/a-n/a (2015).

71. Cicoira, F., Sessolo, M., Yaghmazadeh, O., DeFranco, J. A., Yang, S. Y. & Malliaras, G. G. Influence of device geometry on sensor characteristics of planar organic electrochemical transistors. *Adv. Mater. Deerfield Beach Fla* **22**, 1012–1016 (2010).

72. Hütter, P. C., Rothländer, T., Haase, A., Trimmel, G. & Stadlober, B. Influence of geometry variations on the response of organic electrochemical transistors. *Appl. Phys. Lett.* **103**, 043308 (2013).

73. Bard, A. J. & Faulkner, L. R. *Electrochemical methods: fundamentals and applications*. (Wiley, 2001).

74. Khodagholy, D., Gurfinkel, M., Stavrinidou, E., Leleux, P., Herve, T., Sanaur, S. & Malliaras, G. G. High speed and high density organic electrochemical transistor arrays. *Appl. Phys. Lett.* **99**, 163304 (2011).

75. Jonsson, A. Organic electronics for precise delivery of neurotransmitters. 109.

76. Simon, D. T., Gabrielsson, E. O., Tybrandt, K. & Berggren, M. Organic Bioelectronics: Bridging the Signaling Gap between Biology and Technology. *Chem. Rev.* **116**, 13009–13041 (2016).

77. Strakosas, X., Wei, B., C. Martin, D. & M. Owens, R. Biofunctionalization of polydioxythiophene derivatives for biomedical applications. *J. Mater. Chem. B* **4**, 4952–4968 (2016).

78. Amorini, F., Zironi, I., Marzocchi, M., Gualandi, I., Calienni, M., Cramer, T., Fraboni, B. & Castellani, G. Electrically Controlled 'Sponge Effect' of PEDOT:PSS Governs Membrane Potential and Cellular Growth. *ACS Appl. Mater. Interfaces* **9**, 6679–6689 (2017).

79. Ramuz, M., Hama, A., Huerta, M., Rivnay, J., Leleux, P. & Owens, R. M. Combined Optical and Electronic Sensing of Epithelial Cells Using Planar Organic Transistors. *Adv. Mater.* **26**, 7083–7090 (2014).

80. Inal, S., Hama, A., Ferro, M., Pitsalidis, C., Oziat, J., Iandolo, D., Pappa, A.-M., Hadida, M., Huerta, M., Marchat, D., Mailley, P. & Owens, R. M. Conducting Polymer Scaffolds for Hosting and Monitoring 3D Cell Culture. *Adv. Biosyst.* **1**, 1700052 (2017).

81. Crispin, X., Jakobsson, F. L. E., Crispin, A., Grim, P. C. M., Andersson, P., Volodin, A., van Haesendonck, C., Van der Auweraer, M., Salaneck, W. R. & Berggren, M. The Origin of the High Conductivity of Poly(3,4-ethylenedioxythiophene)−Poly(styrenesulfonate) (PEDOT−PSS) Plastic Electrodes. *Chem. Mater.* **18**, 4354–4360 (2006).

82. Yan, F., Parrott, E. P. J., Ung, B. S.-Y. & Pickwell-MacPherson, E. Solvent Doping of PEDOT/PSS: Effect on Terahertz Optoelectronic Properties and Utilization in Terahertz Devices. *J. Phys. Chem. C* **119**, 6813–6818 (2015).

83. Nardes, A. M., Kemerink, M., de Kok, M. M., Vinken, E., Maturova, K. & Janssen, R. A. J. Conductivity, work function, and environmental stability of PEDOT:PSS thin films treated with sorbitol. *Org. Electron.* **9**, 727–734 (2008).

84. Wen, Y. & Xu, J. Scientific Importance of Water-Processable PEDOT–PSS and Preparation, Challenge and New Application in Sensors of Its Film Electrode: A Review. *J. Polym. Sci. Part Polym. Chem.* **55**, 1121–1150 (2017).

85. Mantione, D., del Agua, I., Sanchez-Sanchez, A., Mecerreyes, D., Mantione, D., del Agua, I., Sanchez-Sanchez, A. & Mecerreyes, D. Poly(3,4-ethylenedioxythiophene) (PEDOT) Derivatives: Innovative Conductive Polymers for Bioelectronics. *Polymers* **9**, 354 (2017).

86. Liao, C., Zhang, M., Niu, L., Zheng, Z. & Yan, F. Organic electrochemical transistors with graphene-modified gate electrodes for highly sensitive and selective dopamine sensors. *J. Mater. Chem. B* **2**, 191–200 (2013).

87. Liao, C., Zhang, M., Niu, L., Zheng, Z. & Yan, F. Highly selective and sensitive glucose sensors based on organic electrochemical transistors with graphene-modified gate electrodes. *J. Mater. Chem. B* **1**, 3820–3829 (2013).

88. Tarabella, G., Villani, M., Calestani, D., Mosca, R., Iannotta, S., Zappettini, A. & Coppedè, N. A single cotton fiber organic electrochemical transistor for liquid electrolyte saline sensing. *J. Mater. Chem.* **22**, 23830 (2012).

89. Yang, A., Li, Y., Yang, C., Fu, Y., Wang, N., Li, L. & Yan, F. Fabric Organic Electrochemical Transistors for Biosensors. *Adv. Mater.* **30**, 1800051 (2018).

90. Campana, A., Cramer, T., Simon, D. T., Berggren, M. & Biscarini, F. Electrocardiographic Recording with Conformable Organic Electrochemical Transistor Fabricated on Resorbable Bioscaffold. *Adv. Mater.* **26**, 3874–3878 (2014).

91. Lin, P., Yan, F. & Chan, H. L. W. Ion-Sensitive Properties of Organic Electrochemical Transistors. *ACS Appl. Mater. Interfaces* **2**, 1637–1641 (2010).

92. Ghittorelli, M., Lingstedt, L., Romele, P., Crăciun, N. I., Kovács-Vajna, Z. M., Blom, P. W. M. & Torricelli, F. High-sensitivity ion detection at low voltages with current-driven organic electrochemical transistors. *Nat. Commun.* **9**, (2018).

93. Lin, P., Luo, X., Hsing, I.-M. & Yan, F. Organic Electrochemical Transistors Integrated in Flexible Microfluidic Systems and Used for Label-Free DNA Sensing. *Adv. Mater.* **23**, 4035–4040 (2011).

94. Yao, C., Xie, C., Lin, P., Yan, F., Huang, P. & Hsing, I.-M. Organic Electrochemical Transistor Array for Recording Transepithelial Ion Transport of Human Airway Epithelial Cells. *Adv. Mater.* **25**, 6575–6580 (2013).

95. Low-Noise Electronic System Design. *Wiley.com* https://www.wiley.com/en-us/Low+Noise+Electronic+System+Design-p-9780471577423.

96. Kogan, Sh. *Electronic Noise and Fluctuations in Solids*. (Cambridge University Press, 2008).

97. Song, Y. & Lee, T. Electronic noise analyses on organic electronic devices. *J. Mater. Chem. C* **5**, 7123–7141 (2017).

98. Ke, L., Zhao, X. Y., Kumar, R. S. & Chua, S. J. Low-frequency noise measurement and analysis in organic light-emitting diodes. *IEEE Electron Device Lett.* **27**, 555–557 (2006).

99. Klaassen, F. M. Characterization of low 1/f noise in MOS transistors. *IEEE Trans. Electron Devices* **18**, 887–891 (1971).

100. Rhayem, J., Rigaud, D., Valenza, M., Szydlo, N. & Lebrun, H. 1/f Noise in amorphous silicon thin film transistors: effect of scaling down. *Solid-State Electron.* **43**, 713–721 (1999).

101. McWhorter, A. L. (Alan L. 1/f noise and related surface effects in germanium. (Massachusetts Institute of Technology, 1955).

102. Hooge, F. N., Kleinpenning, T. G. M. & Vandamme, L. K. J. Experimental studies on 1/f noise. *Rep. Prog. Phys.* **44**, 479 (1981).

103. Corradetti, A., Leoni, R., Carluccio, R., Fortunato, G., Reita, C., Plais, F. & Pribat, D. Evidence of carrier number fluctuation as origin of 1/ *f* noise in polycrystalline silicon thin film transistors. *Appl. Phys. Lett.* **67**, 1730–1732 (1995).

104. Hooge, F. N. 1/f noise. *Phys. BC* **83**, 14–23 (1976).

105. Necliudov, P. V., Rumyantsev, S. L., Shur, M. S., Gundlach, D. J. & Jackson, T. N. 1/f noise in pentacene organic thin film transistors. *J. Appl. Phys.* **88**, 5395–5399 (2000).

106. Marinov, O., Deen, M. J., Yu, J., Vamvounis, G., Holdcroft, S. & Woods, W. Low-frequency noise in polymer thin-film transistors. *IEE Proc. - Circuits Devices Syst.* **151**, 466–472 (2004).

107. Conrad, B. R., Cullen, W. G., Yan, W. & Williams, E. D. Percolative effects on noise in pentacene transistors. *Appl. Phys. Lett.* **91**, 242110 (2007).

108. Vandamme, L. K. J., Feyaerts, R., Trefán, Gy. & Detcheverry, C. 1/f noise in pentacene and poly-thienylene vinylene thin film transistors. *J. Appl. Phys.* **91**, 719–723 (2001).

109. Stoop, R. L., Thodkar, K., Sessolo, M., Bolink, H. J., Schönenberger, C. & Calame, M. Charge Noise in Organic Electrochemical Transistors. *Phys. Rev. Appl.* **7**, 014009 (2017).

110. Heller, I., Chatoor, S., Männik, J., Zevenbergen, M. A. G., Oostinga, J. B., Morpurgo, A. F., Dekker, C. & Lemay, S. G. Charge Noise in Graphene Transistors. *Nano Lett.* **10**, 1563–1567 (2010).

111. Tersoff, J. Low-Frequency Noise in Nanoscale Ballistic Transistors. *Nano Lett.* **7**, 194–198 (2007).

112. Sharf, T., Kevek, J. W., DeBorde, T., Wardini, J. L. & Minot, E. D. Origins of Charge Noise in Carbon Nanotube Field-Effect Transistor Biosensors. *Nano Lett.* **12**, 6380–6384 (2012).

113. Sessolo Michele, Khodagholy Dion, Rivnay Jonathan, Maddalena Fabien, Gleyzes Melanie, Steidl Esther, Buisson Bruno, & Malliaras George G. Easy-to-Fabricate Conducting Polymer Microelectrode Arrays. *Adv. Mater.* **25**, 2135–2139 (2013).

114. DeFranco, J. A., Schmidt, B. S., Lipson, M. & Malliaras, G. G. Photolithographic patterning of organic electronic materials. *Org. Electron.* **7**, 22–28 (2006).

115. Polyravas, A. G., Curto, V. F., Schaefer, N., Calia, A. B., Guimera-Brunet, A., Garrido, J. A. & Malliaras, G. G. Impact of contact overlap on transconductance and noise in organic electrochemical transistors. *Flex. Print. Electron.* **4**, 044003 (2019).

116. Bernards, D. A., Macaya, D. J., Nikolou, M., DeFranco, J. A., Takamatsu, S. & Malliaras, G. G. Enzymatic sensing with organic electrochemical transistors. *J. Mater. Chem.* **18**, 116–120 (2007).

117. Pappa, A. M., Ohayon, D., Giovannitti, A., Maria, I. P., Savva, A., Uguz, I., Rivnay, J., McCulloch, I., Owens, R. M. & Inal, S. Direct metabolite detection with an n-type accumulation mode organic electrochemical transistor. *Sci. Adv.* **4**, eaat0911 (2018).

118. Tang, H., Lin, P., Chan, H. L. W. & Yan, F. Highly sensitive dopamine biosensors based on organic electrochemical transistors. *Biosens. Bioelectron.* **26**, 4559–4563 (2011).

119. Lin, P., Yan, F., Yu, J., Chan, H. L. W. & Yang, M. The Application of Organic Electrochemical Transistors in Cell-Based Biosensors. *Adv. Mater.* **22**, 3655–3660 (2010).

120. Gkoupidenis, P., Schaefer, N., Garlan, B. & Malliaras, G. G. Neuromorphic Functions in PEDOT:PSS Organic Electrochemical Transistors. *Adv. Mater.* **27**, 7176–7180 (2015).

121. Yamamoto, S. & Malliaras, G. G. Controlling the Neuromorphic Behavior of Organic Electrochemical Transistors by Blending Mixed and Ion Conductors. *ACS Appl. Electron. Mater.* **2**, 2224–2228 (2020).

122. Proctor, C. M., Rivnay, J. & Malliaras, G. G. Understanding volumetric capacitance in conducting polymers. *J. Polym. Sci. Part B Polym. Phys.* **54**, 1433–1436 (2016).

123. Clément, N., Nishiguchi, K., Dufreche, J. F., Guerin, D., Fujiwara, A. & Vuillaume, D. A silicon nanowire ion-sensitive field-effect transistor with elementary charge sensitivity. *Appl. Phys. Lett.* **98**, 014104 (2011).

124. Münzenrieder, N., Salvatore, G. A., Petti, L., Zysset, C., Büthe, L., Vogt, C., Cantarella, G. & Tröster, G. Contact resistance and overlapping capacitance in flexible sub-micron long oxide thin-film transistors for above 100 MHz operation. *Appl. Phys. Lett.* **105**, 263504 (2014).

125. Koutsouras, D. A., Gkoupidenis, P., Stolz, C., Subramanian, V., Malliaras, G. G. & Martin, D. C. Impedance Spectroscopy of Spin-Cast and Electrochemically Deposited PEDOT:PSS Films on Microfabricated Electrodes with Various Areas. *ChemElectroChem* **4**, 2321–2327 (2017).

126. Newman, J. Resistance for Flow of Current to a Disk. *J. Electrochem. Soc.* **113**, 501–502 (1966).

127. Buzsáki, G. *Rhythms of the Brain*. (Oxford University Press, 2006). doi:10.1093/acprof:oso/9780195301069.001.0001.

128. Bedner, K., Guzenko, V. A., Tarasov, A., Wipf, M., Stoop, R. L., Rigante, S., Brunner, J., Fu, W., David, C., Calame, M., Gobrecht, J. & Schönenberger, C. Investigation of the dominant 1/f noise source in silicon nanowire sensors. *Sens. Actuators B Chem.* **191**, 270–275 (2014).

129. Sessolo, M., Khodagholy, D., Rivnay, J., Maddalena, F., Gleyzes, M., Steidl, E., Buisson, B. & Malliaras, G. G. Easy-to-Fabricate Conducting Polymer Microelectrode Arrays. *Adv. Mater.* **25**, 2135–2139 (2013).

130. Andersson Ersman, P., Lassnig, R., Strandberg, J., Tu, D., Keshmiri, V., Forchheimer, R., Fabiano, S., Gustafsson, G. & Berggren, M. All-printed large-scale integrated circuits based on organic electrochemical transistors. *Nat. Commun.* **10**, 1–9 (2019).

131. Nilsson, D., Kugler, T., Svensson, P.-O. & Berggren, M. An all-organic sensor–transistor based on a novel electrochemical transducer concept printed electrochemical sensors on paper. *Sens. Actuators B Chem.* **86**, 193–197 (2002).

132. Hamedi, M., Herlogsson, L., Crispin, X., Marcilla, R., Berggren, M. & Inganäs, O. Fiber-Embedded Electrolyte-Gated Field-Effect Transistors for e-Textiles. *Adv. Mater.* **21**, 573–577 (2009).

133. Strakosas, X., Bongo, M. & Owens, R. M. The organic electrochemical transistor for biological applications. *J. Appl. Polym. Sci.* **132**, (2015).

134. Bai, L., Elósegui, C. G., Li, W., Yu, P., Fei, J. & Mao, L. Biological Applications of Organic Electrochemical Transistors: Electrochemical Biosensors and Electrophysiology Recording. *Front. Chem.* **7**, (2019).

135. Leleux, P., Rivnay, J., Lonjaret, T., Badier, J.-M., Bénar, C., Hervé, T., Chauvel, P. & Malliaras, G. G. Organic Electrochemical Transistors for Clinical Applications. *Adv. Healthc. Mater.* **4**, 142–147 (2015).

136. Cea, C., Spyropoulos, G. D., Jastrzebska-Perfect, P., Ferrero, J. J., Gelinas, J. N. & Khodagholy, D. Enhancement-mode ion-based transistor as a comprehensive interface and real-time processing unit for in vivo electrophysiology. *Nat. Mater.* 1–8 (2020) doi:10.1038/s41563-020-0638-3.

137. Zhang, M., Liao, C., Mak, C. H., You, P., Mak, C. L. & Yan, F. Highly sensitive glucose sensors based on enzyme-modified whole-graphene solution-gated transistors. *Sci. Rep.* **5**, (2015).

138. Pappa, A.-M., Curto, V. F., Braendlein, M., Strakosas, X., Donahue, M. J., Fiocchi, M., Malliaras, G. G. & Owens, R. M. Organic Transistor Arrays Integrated with Finger-Powered Microfluidics for Multianalyte Saliva Testing. *Adv. Healthc. Mater.* **5**, 2295–2302 (2016).

139. Braendlein, M., Pappa, A.-M., Ferro, M., Lopresti, A., Acquaviva, C., Mamessier, E., Malliaras, G. G. & Owens, R. M. Lactate Detection in Tumor Cell Cultures Using Organic Transistor Circuits. *Adv. Mater.* **29**, 1605744 (2017).

140. Curto, V. F., Marchiori, B., Hama, A., Pappa, A.-M., Ferro, M. P., Braendlein, M., Rivnay, J., Fiocchi, M., Malliaras, G. G., Ramuz, M. & Owens, R. M. Organic transistor platform with integrated microfluidics for in-line multi-parametric *in vitro* cell monitoring. *Microsyst. Nanoeng.* **3**, 17028 (2017).

141. Pitsalidis, C., Ferro, M. P., Iandolo, D., Tzounis, L., Inal, S. & Owens, R. M. Transistor in a tube: A route to three-dimensional bioelectronics. *Sci. Adv.* **4**, eaat4253 (2018).

142. Giovannitti, A., Sbircea, D.-T., Inal, S., Nielsen, C. B., Bandiello, E., Hanifi, D. A., Sessolo, M., Malliaras, G. G., McCulloch, I. & Rivnay, J. Controlling the mode of operation of organic transistors through side-chain engineering. *Proc. Natl. Acad. Sci.* **113**, 12017–12022 (2016).

143. Spyropoulos, G. D., Gelinas, J. N. & Khodagholy, D. Internal ion-gated organic electrochemical transistor: A building block for integrated bioelectronics. *Sci. Adv.* **5**, eaau7378 (2019).

144. Malti, A., Edberg, J., Granberg, H., Khan, Z. U., Andreasen, J. W., Liu, X., Zhao, D., Zhang, H., Yao, Y., Brill, J. W., Engquist, I., Fahlman, M., Wågberg, L., Crispin, X. & Berggren, M. An Organic Mixed Ion-Electron Conductor for Power Electronics. *Adv. Sci. Weinh. Baden-Wurtt. Ger.* **3**, 1500305 (2016).

145. Liu, Y., He, H., Chen, R., En, Y.-F., Li, B. & Chen, Y.-Q. Analysis and Simulation of Low-Frequency Noise in Indium-Zinc-Oxide Thin-Film Transistors. *IEEE J. Electron Devices Soc.* **6**, 271–279 (2018).

146. Choi, H.-S., Jeon, S., Kim, H., Shin, J., Kim, C. & Chung, U.-I. The impact of active layer thickness on low-frequency noise characteristics in InZnO thin-film transistors with high mobility. *Appl. Phys. Lett.* **100**, 173501 (2012).

147. Männik, J., Heller, I., Janssens, A. M., Lemay, S. G. & Dekker, C. Charge Noise in Liquid-Gated Single-Wall Carbon Nanotube Transistors. *Nano Lett.* **8**, 685–688 (2008).

148. Hébert, C., Masvidal-Codina, E., Suarez-Perez, A., Calia, A. B., Piret, G., Garcia-Cortadella, R., Illa, X., Garcia, E. D. C., Sanchez, J. M. D. la C., Casals, D. V., Prats-Alfonso, E., Bousquet, J., Godignon, P., Yvert, B., Villa, R., Sanchez-Vives, M. V., Guimerà-Brunet, A. & Garrido, J. A. Flexible Graphene Solution-Gated Field-Effect Transistors: Efficient Transducers for Micro-Electrocorticography. *Adv. Funct. Mater.* **28**, 1703976 (2018).

149. Kuzum, D., Takano, H., Shim, E., Reed, J. C., Juul, H., Richardson, A. G., de Vries, J., Bink, H., Dichter, M. A., Lucas, T. H., Coulter, D. A., Cubukcu, E. & Litt, B. Transparent and flexible low

noise graphene electrodes for simultaneous electrophysiology and neuroimaging. *Nat. Commun.* **5**, 1–10 (2014).

150. Ghibaudo, G., Roux, O., Nguyen-Duc, C., Balestra, F. & Brini, J. Improved Analysis of Low Frequency Noise in Field-Effect MOS Transistors. *Phys. Status Solidi A* **124**, 571–581 (1991).

151. Cardiovascular diseases (CVDs). https://www.who.int/news-room/fact-sheets/detail/cardiovascular-diseases-(cvds). Accessed 30/6/2021.

152. Gruetzmann, A., Hansen, S. & Müller, J. Novel dry electrodes for ECG monitoring. *Physiol. Meas.* **28**, 1375–1390 (2007).

153. Wu, H., Yang, G., Zhu, K., Liu, S., Guo, W., Jiang, Z. & Li, Z. Materials, Devices, and Systems of On-Skin Electrodes for Electrophysiological Monitoring and Human–Machine Interfaces. *Adv. Sci.* **8**, 2001938 (2021).

154. Bihar, E., Roberts, T., Saadaoui, M., Hervé, T., Graaf, J. B. D. & Malliaras, G. G. Inkjet-Printed PEDOT:PSS Electrodes on Paper for Electrocardiography. *Adv. Healthc. Mater.* **6**, 1601167 (2017).

155. Velasco-Bosom, S., Karam, N., Carnicer-Lombarte, A., Gurke, J., Casado, N., Tomé, L. C., Mecerreyes, D. & Malliaras, G. G. Conducting Polymer-Ionic Liquid Electrode Arrays for High-Density Surface Electromyography. *Adv. Healthc. Mater.* **n/a**, 2100374.

156. Bihar, E., Roberts, T., Ismailova, E., Saadaoui, M., Isik, M., Sanchez-Sanchez, A., Mecerreyes, D., Hervé, T., Graaf, J. B. D. & Malliaras, G. G. Fully Printed Electrodes on Stretchable Textiles for Long-Term Electrophysiology. *Adv. Mater. Technol.* **2**, 1600251 (2017).

157. Uguz, I., Ganji, M., Hama, A., Tanaka, A., Inal, S., Youssef, A., Owens, R. M., Quilichini, P. P., Ghestem, A., Bernard, C., Dayeh, S. A. & Malliaras, G. G. Autoclave Sterilization of PEDOT:PSS Electrophysiology Devices. *Adv. Healthc. Mater.* **5**, 3094–3098 (2016).

158. Braendlein, M., Lonjaret, T., Leleux, P., Badier, J. & Malliaras, G. G. Voltage Amplifier Based on Organic Electrochemical Transistor. *Adv. Sci.* **4**, (2016).

159. Liao, C., Mak, C., Zhang, M., Chan, H. L. W. & Yan, F. Flexible Organic Electrochemical Transistors for Highly Selective Enzyme Biosensors and Used for Saliva Testing. *Adv. Mater.* **27**, 676–681 (2015).

160. Bihar, E., Deng, Y., Miyake, T., Saadaoui, M., Malliaras, G. G. & Rolandi, M. A Disposable paper breathalyzer with an alcohol sensing organic electrochemical transistor. *Sci. Rep.* **6**, 27582 (2016).

161. Scheiblin, G., Coppard, R., Owens, R. M., Mailley, P. & Malliaras, G. G. Referenceless pH Sensor using Organic Electrochemical Transistors. *Adv. Mater. Technol.* **2**, 1600141 (2017).

162. Polyravas, A. G., Schaefer, N., Curto, V. F., Calia, A. B., Guimera-Brunet, A., Garrido, J. A. & Malliaras, G. G. Effect of channel thickness on noise in organic electrochemical transistors. *Appl. Phys. Lett.* **117**, 073302 (2020).

163. Klein, E. Chapter 24 - Ethics and the emergence of brain-computer interface medicine. in *Handbook of Clinical Neurology* (eds. Ramsey, N. F. & Millán, J. del R.) vol. 168 329–339 (Elsevier, 2020).

164. Wolpaw, J. R. & McFarland, D. J. Control of a two-dimensional movement signal by a noninvasive brain-computer interface in humans. *Proc. Natl. Acad. Sci. U. S. A.* **101**, 17849–17854 (2004).

165. Schwartz, A. B. Cortical neural prosthetics. *Annu. Rev. Neurosci.* **27**, 487–507 (2004).

166. Lebedev, M. A. & Nicolelis, M. A. L. Brain-machine interfaces: past, present and future. *Trends Neurosci.* **29**, 536–546 (2006).

167. Millán, J. del R., Rupp, R., Mueller-Putz, G., Murray-Smith, R., Giugliemma, C., Tangermann, M., Vidaurre, C., Cincotti, F., Kubler, A., Leeb, R., Neuper, C., Mueller, K. R. & Mattia, D. Combining Brain–Computer Interfaces and Assistive Technologies: State-of-the-Art and Challenges. *Front. Neurosci.* **4**, (2010).

168. Introduction to Neural Engineering for Motor Rehabilitation | Wiley. *Wiley.com* https://www.wiley.com/en-us/Introduction+to+Neural+Engineering+for+Motor+Rehabilitation-p-9781118628638.

169. Dobkin, B. H. Brain–computer interface technology as a tool to augment plasticity and outcomes for neurological rehabilitation. *J. Physiol.* **579**, 637–642 (2007).

170. Birbaumer, N., Murguialday, A. R. & Cohen, L. Brain-computer interface in paralysis. *Curr. Opin. Neurol.* **21**, 634–638 (2008).

171. King, C. E., Wang, P. T., McCrimmon, C. M., Chou, C. C., Do, A. H. & Nenadic, Z. The feasibility of a brain-computer interface functional electrical stimulation system for the restoration of overground walking after paraplegia. *J. NeuroEngineering Rehabil.* **12**, 80 (2015).

172. Herrmann, C. S., Fründ, I. & Lenz, D. Human gamma-band activity: a review on cognitive and behavioral correlates and network models. *Neurosci. Biobehav. Rev.* **34**, 981–992 (2010).

173. Polikov, V. S., Tresco, P. A. & Reichert, W. M. Response of brain tissue to chronically implanted neural electrodes. *J. Neurosci. Methods* **148**, 1–18 (2005).

174. Pas, J., Rutz, A. L., Quilichini, P. P., Slézia, A., Ghestem, A., Kaszas, A., Donahue, M. J., Curto, V. F., O'Connor, R. P., Bernard, C., Williamson, A. & Malliaras, G. G. A bilayered PVA/PLGA-bioresorbable shuttle to improve the implantation of flexible neural probes. *J. Neural Eng.* **15**, 065001 (2018).

175. Saxena, T., Karumbaiah, L., Gaupp, E. A., Patkar, R., Patil, K., Betancur, M., Stanley, G. B. & Bellamkonda, R. V. The impact of chronic blood-brain barrier breach on intracortical electrode function. *Biomaterials* **34**, 4703–4713 (2013).

176. Kotzar, G., Freas, M., Abel, P., Fleischman, A., Roy, S., Zorman, C., Moran, J. M. & Melzak, J. Evaluation of MEMS materials of construction for implantable medical devices. *Biomaterials* **23**, 2737–2750 (2002).

177. Lind, G., Linsmeier, C. E. & Schouenborg, J. The density difference between tissue and neural probes is a key factor for glial scarring. *Sci. Rep.* **3**, 2942 (2013).

178. Muller, R., Le, H.-P., Li, W., Ledochowitsch, P., Gambini, S., Bjorninen, T., Koralek, A., Carmena, J. M., Maharbiz, M. M., Alon, E. & Rabaey, J. M. A Minimally Invasive 64-Channel Wireless µECoG Implant. *IEEE J. Solid-State Circuits* **50**, 344–359 (2015).

179. Crone, N. E. Functional mapping with ECoG spectral analysis. *Adv. Neurol.* **84**, 343–351 (2000).

180. Jasper, H. H., Arfel-Capdeville, G. & Rasmussen, T. Evaluation of EEG and cortical electrographic studies for prognosis of seizures following surgical excision of epileptogenic lesions. *Epilepsia* **2**, 130–137 (1961).

181. Organic Implantable Probes for in vivo Recordings of Electrophysciological Activity and Drug Delivery | Semantic Scholar.

182. Bundy, D. T., Zellmer, E., Gaona, C. M., Sharma, M., Szrama, N., Hacker, C., Freudenburg, Z. V., Daitch, A., Moran, D. W. & Leuthardt, E. C. Characterization of the effects of the human dura on macro- and micro-electrocorticographic recordings. *J. Neural Eng.* **11**, 016006 (2014).

183. John, S. E., Opie, N. L., Wong, Y. T., Rind, G. S., Ronayne, S. M., Gerboni, G., Bauquier, S. H., O'Brien, T. J., May, C. N., Grayden, D. B. & Oxley, T. J. Signal quality of simultaneously recorded endovascular, subdural and epidural signals are comparable. *Sci. Rep.* **8**, 8427 (2018).

184. Lee, W., Kim, D., Rivnay, J., Matsuhisa, N., Lonjaret, T., Yokota, T., Yawo, H., Sekino, M., Malliaras, G. G. & Someya, T. Integration of Organic Electrochemical and Field-Effect Transistors for Ultraflexible, High Temporal Resolution Electrophysiology Arrays. *Adv. Mater.* **28**, 9722–9728 (2016).

185. Pierre, L., Jonathan, R., Thomas, L., Jean-Michel, B., Christian, B., Thierry, H., Patrick, C. & G, M. G. Organic Electrochemical Transistors for Clinical Applications. *Adv. Healthc. Mater.* **4**, 142–147 (2015).

186. Lecomte, A., Degache, A., Descamps, E., Dahan, L. & Bergaud, C. In vitro and in vivo biostability assessment of chronically-implanted Parylene C neural sensors. *Sens. Actuators B Chem.* **251**, 1001–1008 (2017).

187. Chang, T. Y., Yadav, V. G., De Leo, S., Mohedas, A., Rajalingam, B., Chen, C.-L., Selvarasah, S., Dokmeci, M. R. & Khademhosseini, A. Cell and Protein Compatibility of Parylene-C Surfaces. *Langmuir* **23**, 11718–11725 (2007).

188. de la Oliva, N., Mueller, M., Stieglitz, T., Navarro, X. & del Valle, J. On the use of Parylene C polymer as substrate for peripheral nerve electrodes. *Sci. Rep.* **8**, 5965 (2018).

189. Khodagholy, D., Gelinas, J. N., Thesen, T., Doyle, W., Devinsky, O., Malliaras, G. G. & Buzsáki, G. NeuroGrid: recording action potentials from the surface of the brain. *Nat. Neurosci.* **18**, 310–315 (2015).

190. Grimnes, S. & Martinsen, Ø. G. Chapter 7 - Electrodes. in *Bioimpedance and Bioelectricity Basics (Third Edition)* (eds. Grimnes, S. & Martinsen, Ø. G.) 179–254 (Academic Press, 2015). doi:10.1016/B978-0-12-411470-8.00007-6.